Organic Opto-Electronic Devices for Data Storage and Solid-State Lighting

Item type	text; Electronic Dissertation
Authors	Lauters, Michael E
Publisher	The University of Arizona.
Rights	Copyright © is held by the author. Digital access to this material is made possible by the University Libraries, University of Arizona. Further transmission, reproduction or presentation (such as public display or performance) of protected items is prohibited except with permission of the author.
Downloaded	17-Sep-2016 23:54:15
Link to item	http://hdl.handle.net/10150/193770

ORGANIC OPTO-ELECTRONIC DEVICES FOR DATA STORAGE AND SOLID-STATE LIGHTING

by

Michael E. Lauters

A Dissertation Submitted to the Faculty of the

COMMITTEE ON OPTICAL SCIENCES (GRADUATE)

In Partial Fulfillment of the Requirements
For the Degree of

DOCTOR OF PHILOSOPHY

In the Graduate College

THE UNIVERSITY OF ARIZONA

2006

THE UNIVERSITY OF ARIZONA
GRADUATE COLLEGE

As members of the Dissertation Committee, we certify that we have read the dissertation

prepared by **Michael E. Lauters**

entitled **Organic Opto-Electronic Devices for Data Storage and Solid-State Lighting**

and recommend that it be accepted as fulfilling the dissertation requirement for the

Degree of **Doctor of Philosophy**

____ Date: **9/29/2006**
Dror Sarid, Faculty Advisor

____ Date: **9/29/2006**
Ghassan Jabbour, Member

____ Date: **9/29/2006**
Thomas Milster, Member

Final approval and acceptance of this dissertation is contingent upon the candidate's submission of the final copies of the dissertation to the Graduate College.

I hereby certify that I have read this dissertation prepared under my direction and recommend that it be accepted as fulfilling the dissertation requirement.

____ Date: **9/29/2006**
Dissertation Director: **Dror Sarid**

STATEMENT BY AUTHOR

This dissertation has been submitted in partial fulfillment of requirements for an advanced degree at The University of Arizona and is deposited in the University Library to be made available to borrowers under rules of the Library.

Brief quotations from this dissertation are allowable without special permission, provided that accurate acknowledgment of source is made. Requests for permission for extended quotation from or reproduction of this manuscript in whole or in part may be granted by the head of the major department or the Dean of the Graduate College when in his or her judgment the proposed use of the material is in the interests of scholarship. In all other instances, however, permission must be obtained from the author.

SIGNED: Michael E. Lauters

ACKNOWLEDGEMENTS

I would like to express my tremendous gratitude to my academic advisor, Professor Ghassan Jabbour, for providing me with a great opportunity to conduct my research on this dissertation. The balance that he has provided me, between the freedom to choose experiments of interest and the structured guidance of my work, has been ideal. His outstanding knowledge of the entire field of organic opto-electronics and endless curiosity in all the sciences has inspired me throughout my graduate career. I would like to thank Professor Dror Sarid my dissertation director and acting faculty advisor. I am extremely grateful for his guidance and support throughout my time at the Optical Sciences Center. I would also like to thank Professor Tom Milster for serving on my committee and providing me with helpful advice and interesting questions.

I need to give a special thanks to Dr. Brendan McCarthy for the many discussions and experiments that we have shared on the topic of organic memory. Also, a "thank you" to Leonid Boguslavksy and Dr. Robert Norwood for their insight and help with the Optical Bio-Chemical Sensor project. I would like to thank Sheng Li, Jesse Froehlich, Stephan Hyunsik, Dr. Mochosuki San, and the rest of the Nitto Denko Corporation for their collaboration, materials, and funding. I would also like to thank the Department of Energy (DE-FG-03-02ER46013) for funding.

I would like to mention that without my parents Donna and Mike, I would have never been possible. They have given me the work ethic, morals, and values that have helped me become the person I am today. My parents and brothers, Jason and Mitch, have inspired me throughout my life and have given me a foundation to always rely on.

Last but not least, I want to thank my friends/colleagues; Dr. Jian Li, Evan Williams, Mike Morrell, Ranjan Grover, Dr. Yuka Yoshioka, Anna Flesher, Dennis Douglas, Hanna Heikkinen, Dr. Brigitte, Wex, Parul Dhagat, Konstantine Yamnitskiy, Steve Stromski, Jeremy Rogers, Nathan Leisso, Chris Derose, Eric Goodwin, Jason Auxier, Jacob Hesterman, Kevin Schultz, John Sullivan, Dr. Brian Kinder, Quinn Sanford, Professor Nasser Peyghambarian, and the staff of the College of Optical Sciences for their unique support and memories during my graduate career.

DEDICATION

This dissertation is dedicated to my wife Leah and our new family.

TABLE OF CONTENTS

PART I Nonvolatile multilevel conductance switching and memory effects in organic thin-film structures

TABLE OF CONTENTS - *Continued*

TABLE OF CONTENTS - *Continued*

PART II White organic light-emitting devices (WOLEDs) incorporating lumophore-functionalized macromolecules

LIST OF FIGURES

LIST OF FIGURES – *Continued*

LIST OF FIGURES - *Continued*

LIST OF FIGURES – *Continued*

LIST OF FIGURES – *Continued*

LIST OF FIGURES – *Continued*

LIST OF TABLES

ABSTRACT

In the first part of this dissertation, metal/organic/indium tin oxide (ITO) structures, including OLEDs, are demonstrated to contain multiple nonvolatile conductance states that can be programmed by the application of an external bias above a certain threshold voltage (V_{th}). These conductance states are stable and in turn can be probed by the use of a bias lower in value than V_{th}. The unbiased retention time of states is greater than several weeks, and more than 48,000 write-read-rewrite-read cycles have been performed with minimal degradation. It is found that the programming of a continuum of conductance states is possible, and techniques to do so are outlined. The electrical conductivity of the highest and lowest states can differ by six orders of magnitude. Switching speeds below 50 ns are shown, resulting in an energy requirement of about 100 pJ to switch from one conductance state to another. The memory phenomenon is shown to be influenced by the active layer thickness and anode/surface roughness while temperature dependence is limited. The electrical characteristics of these devices are consistent with metal diffusion or filament phenomena found in metal-insulator-metal structures, suggesting a possible mechanism by which the states are stored.

In the second part of this dissertation, electroluminescent devices employing several new organic-inorganic lumophore-functionalized macromolecules are presented. In this study, macromolecules incorporating several lumophores covalently bonded to the vertices of a cubical core structure based on Polyhedral Oligomeric Silsesquioxane

(POSS) in multiple configurations are implemented as light-emitting centers. The hole-transporting polymer poly(*N*-vinylcarbazole) (PVK) and electron-transporting additive 2-(4-biphenylyl)-5-(4-tert-butylphenyl)1,3,4-oxadiazole (PBD) are used as a two-part host to enhance the carrier transport in these simple solution-processed single-layer devices. A study of energy transfer in several systems is carried out to understand the requirements needed to create white-light emission from a single macromolecule. A single macromolecule incorporating twenty-one blue and one yellow lumophore is shown to exhibit field-independent stable white-light electroluminescence with Commission Internationale de l'Eclairage (CIE) coordinates of (0.31, 0.37). An external quantum efficiency of 0.55 percent and a maximum brightness of 1600 cd/m^2 are attained with simple solution-processed single-layer devices. High solubility and ease of purification give these macromolecule white-light emitters advantages over their small molecule and polymeric type counterparts.

OUTLINE OF DISSERTATION

Data storage is the first topic to be discussed in this dissertation (Chapters 1-6). Chapter 1 provides an introduction to data storage techniques in the current consumer market and novel memories still in their developmental stages. Chapter 2 presents a historical review of previous work done on the investigation of conductance switching and memory phenomena found in thin-film structures including both organic and inorganic materials. This review is of utmost importance due to the lack of an agreed upon theory of the mechanism(s) behind the switching phenomenon. Chapter 2 will include the vast number of materials used, mechanisms proposed, structures fabricated, and evidence found in previous publications. Chapter 3 will provide information of the device fabrication techniques and materials used in single and multilayer devices tested in our laboratories. In addition, Chapter 3 will give a description of the SPM characterization that was used in the probing of the devices. Chapter 4 shows a detailed look at programming techniques and I-V characteristics of our memory devices. I-V curves showing regions of high stability, low stability, and negative differential resistance will be examined. The current response to voltage pulses will be shown and switching speeds of the device will be investigated. Chapter 5 will show examples of the cyclic switching reliability and the nonvolatile nature of the multilevel conductance states in several materials and device structures. Temperature and active layer thickness dependence will be investigated in relation to switching reliability, threshold voltage, current densities, and stability of states. Chapter 6 will highlight a possible mechanism behind the switching phenomenon found in our devices and discuss experiments to gain direct evidence of filament existence.

The next two chapters (Chapters 7 and 8) are dedicated to macromolecule-based WOLEDs for use in solid-state lighting applications and LCD displays. Chapter 7 will introduce the topic of WOLEDs and discuss the many approaches to this technology. Chapter 8 will present work on single-layer white light-emitting electroluminescent devices based on solution-processed organic-inorganic lumophore-functionalized macromolecules. Chapter 9 concludes this study on organic memory and macromolecule-incorporated WOLEDs. A discussion of potential future work and possible applications of these technologies is included.

CHAPTER 1

INTRODUCTION TO DATA STORAGE TECHNOLOGIES

1.1 Motivation of this study

As conventional data storage technologies reach their fundamental limits, new techniques to store information increasingly gain interest and excitement. Memories that will increase data densities, decrease storage costs, quicken read/write speeds, and utilize less power are needed to quench the relentless thirst of the new digital electronics. New devices that utilize flexible displays, employ light-weight materials, and require a high degree of integration will demand a memory that is more versatile than the memories of today. Nonvolatile organic thin-film memory is a promising candidate in the quest for this ultimate memory technology. The underlying mechanism(s) responsible for the switching phenomenon is still under debate and this study attempts to further its understanding. In addition, pinpointing the mechanism may quite possibly give insight to some of the degradation and device efficiency problems found in OLEDs. The conduction mechanism responsible for switching and memory phenomena in these thin films is in direct competition with normal charge injection and transport resulting in the emission of light. Completely eliminating the mechanism for memory effects will increase efficiencies and lifetimes of OLEDs.

1.2 Traditional data storage technologies

This section will give an overview of proven and widely used data storage techniques that are common in many products. The purpose of the following review is to familiarize the reader with what the current technology is capable of and what aspects of the performance of these memories can still be improved upon. There are many types of memories used in many types of ways, and it would be futile to make a direct comparison of every aspect of each. However, there are some common sought-after qualities such as fast read/write times, low cost, high data density, nonvolatility, and low energy consumption to name a few. Although no single memory device has attained immortality by dominating all of these aspects of data storage, the standards are set incredibly high. Any new memory technology will have an incredible barrier to overcome before market share can be gained.

1.2.1 Optical disc storage

Optical data storage is most commonly known in the form of optical discs like compact discs (CDs) for music storage, digital versatile discs (DVDs) for video, and the next generation blue laser technology of high definition DVDs and Blue Ray Discs for high definition movies and large-scale data storage. Optically rewritable discs typically use phase-change materials for storing information, which, by using a laser beam, are switched between their crystalline and amorphous states. Since the optical reflectivity of the phase-change material differs in its crystalline and amorphous states, a change of phase can be used to store and read digital information. To change the phase of the material, a laser beam is focused on the surface of the disc medium. The spot size of the beam at the surface of the disc is estimated by

$$s = \lambda / \sin \theta = \lambda / NA \qquad (1)$$

where s is the $1/e^2$ width intensity of the Gaussian spot illumination, NA is the numerical aperture of the illumination optics, θ is the marginal ray from the illumination optics, and λ is the wavelength of the laser light. As the disc spins the intensity of the beam is modulated. Data is stored when the beams energy is absorbed and the phase-change medium is heated up beyond a critical temperature. At this temperature, the phase of the material changes along with its index of refraction and reflectivity.

Lasers with shorter wavelengths, a larger optical illumination NA, and multiple layers of storage are used to increase the densities of data stored. The Federal Communications Commission **(**FCC) has mandated broadcasters to switch to digital broadcasts by 2009. This will establish the need for an optical disc to hold high-definition content exceeding the 4.7 GB (single-layer) or 8.5 GB (double-layer) capacity of today's DVD media. An example of the storage capacity of several optical disc formats is shown in Table 1.1.

Table 1.1 Parameters and storage capacities of several optical discs.

Media Format	Wavelength	NA	Track Pitch	Substrate Thickness	Capacity
CD	780 nm	0.45	1.6 μm	1.2 mm	0.65 GB
DVD	650 nm	0.6	0.74 μm	0.6 mm	4.7 GB
Blue Ray Disc	405 nm	0.85	0.32 μm	0.1 mm	27 GB

1.2.2 Hard disk drive (HDD)

A second type of disc or disk memory and one of the most common ways to store vast amounts of data for many years is the HDD (Figure 1.1). Invented in the 1950's, this technology has evolved from storing a few megabytes of data on a 20 in. diameter disk to today's performance of nearly half a terabyte of data stored on a 3.5 in. diameter disk (by the time this dissertation gets published it will likely be a terabyte). The reason it's called "hard" is that it has a hard platter that holds magnetic medium (and to distinguish it from the floppy disk drives from the past). Hard disks, floppy disks, and cassette tapes use the same magnetic recording techniques. The benefits of magnetic storage include excellent rewrite-ability and the ability to hold the magnetic flux patterns stored onto the medium for many years.

Figure 1.1 Toshiba's 0.85 in. HDD can store 4 GB of data (*February 2005 issue of Smartphone & Pocket PC).*

HDDs are fabricated by implementing a very simple but very precise technology. The platter is made of high precision aluminum or glass with a coating of magnetic material that is polished to mirror-like smoothness. These platters that hold the bits of information in the form of extremely small magnetic domains spin at speeds up to 15,000 rpm. To program and read the bits of data, a head is scanned over the magnetic surface at a height of only a few nanometers. Data rates (number of bytes per second that the drive can deliver to the central processing unit (CPU)) of more than 500 MB/s and seek times (length of time between the CPU’s request of a file and the detection of the first byte of that file sent to the CPU) of less than 5 ms can be found in products today.

1.2.3 Random access memory (RAM)

One of the most commonly known forms of computer memory is RAM. This type of memory is considered "random access" because the access of any memory cell can be done directly if the location of the row and column intersection is known. The most common type of RAM is dynamic random access memory (DRAM). At each row and column intersection, a transistor and a capacitor are paired representing a single memory cell. The capacitor holds the information (0 or 1) as stored electric charge and the transistor serves as a switch that allows the circuitry of the chip to read or program the capacitor. The capacitor is like a leaky bucket that is used to store electrons. For the memory cell to store a 1, the capacitor is filled with electrons. In just a few milliseconds, the electrons leak out, and the circuitry of the chip must quickly read the state of the cell and refill the capacitor. This is done many times every second for the entire array of memory cells that are storing a 1 in their capacitor. This is a very time consuming process that utilizes a large amount of energy.

When fabricating RAM, memory cells are etched onto a silicon wafer in an array of columns (bitlines) and rows (wordlines). The intersection of a bitline and wordline constitutes the address of the memory cell. DRAM works by sending a charge through the appropriate bitline to activate the transistor at each cell in the column. When writing, the row lines contain the state the capacitor should take on. When reading, the sense-amplifier determines the level of charge in the capacitor. If it is more than 50 percent, it reads a 1; otherwise it reads a 0. The counter tracks the refresh sequence based on which rows have been accessed and in what order. The length of time necessary to do all this is on the order of nanoseconds. What RAM memory lacks in high fabrication cost and low electrical efficiency, it makes up in high speed and reliability.

While DRAM is considered a fast type of memory, static random access memory (SRAM) is even quicker. Using a flip-flop technique and 4 to 6 transistors at each cell, the replenishing of electrons for each capacitor is no longer needed. Although this saves on energy and greatly increases the speed of the RAM, the increase in components adds cost and size to this type of memory. Each type of RAM has its own niche in the computer industry. SRAM is used for the CPU's speed-sensitive small capacity cache and DRAM is used for general large-capacity RAM needs.

1.2.4 Read only memory (ROM)

ROMs are nonvolatile, inexpensive, and reliable. A ROM chip contains a grid of rows and columns similar to RAM but without transistors. A diode or the absence of a diode is located at each intersection of the memory cell array. If a diode is present at a given intersection and the probing bias is above a certain threshold (usually about 0.6 V), a charge will be sent to ground indicating an on state or a "1". If no diode is present, there will be no charge sent to ground, and an off state or "0" will be realized. The way a ROM chip works necessitates the programming of perfect and complete data when the chip is created. A standard ROM chip cannot be reprogrammed or rewritten. If it is incorrect, or the data needs to be updated, it must be discarded. Creating the original template for a ROM chip can be a laborious process. Once the template is completed, the actual chips can cost as little as a few cents each. They use very little power, are extremely reliable, and in the case of most small electronic devices, contain all the necessary programming to control the device.

Programmable read only memory (PROM) is a type of ROM that can be programmed by the purchaser (write-once read-many times). A PROM chip is the same as a ROM chip except that at each intersection instead of a diode or the absence of a diode there is a fuse. Since all the cells have a fuse, the initial (blank) state of a PROM chip is all “1s”. To change the value of a cell to “0”, a specific amount of current is sent to the cell. The higher voltage breaks the connection between the column and row by burning out the fuse.

1.2.5 Flash memory

Flash memory, similar to electrically erasable programmable read only memory (EEPROM), is a relatively new data storage technology and is found in many devices including digital cameras, computer’s BOIS chips, radios, and portable data storage devices (memory sticks). Faster access time, smaller size, and lightness in weight are a few reasons to use flash memory over HDD. Some drawbacks include lack of storage capacity and higher cost. It is a solid-state memory that is comprised of a grid of rows and columns where two transistors (floating gate and control gate) are placed at each intersection. This is the case, although different numbers of transistors can be used. The two transistors are separated from each other by a thin oxide layer where electrons can be trapped to alter the electrical field (Figure 1.2). The electrons trapped on the oxide layer create an electric field that acts like a barrier which can be sensed by passing current through the floating gate and measuring its difference. If the flow through the gate is greater than 50 percent of the charge, it has a value of 1. When the charge passing through drops below the 50-percent threshold, the value changes to 0. The electrons stored in the thin oxide layer can be removed by the application of an appropriate bias thereby returning the state of the cell to a 1.

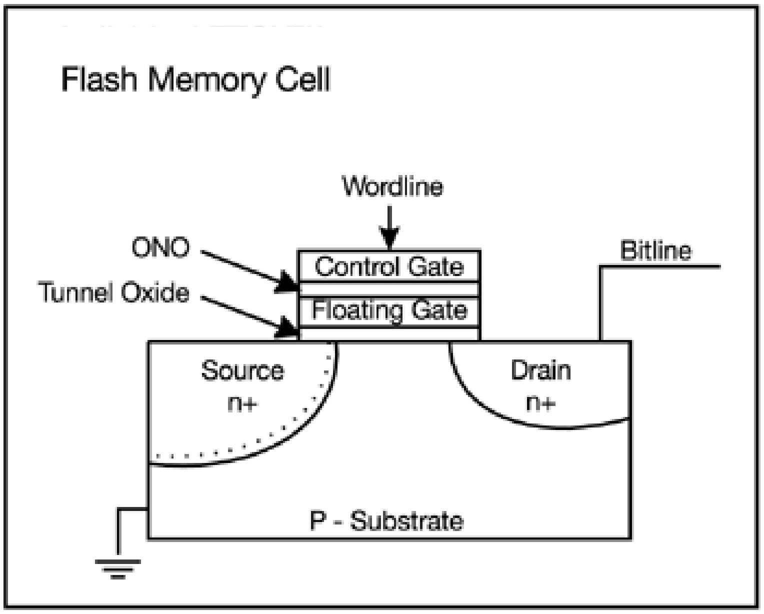

Figure 1.2 Flash memory cell (www.intel.com).

1.3 New data storage technologies

The semiconductor data storage industry has been increasing data densities for the past four decades, just as predicted by the famous Moore's Law. It states that the data densities and circuit complexities will double every 18 months. As Moore's Law comes to an end and the resolution limits (lithography, etching, etc.) come into effect, new data storage techniques will need to further the progress of our memory devices and exceed the performance and scalability limitations of traditional technologies. Memories that can combine the best attributes of several proven data storage techniques into a single memory cell are poised to flourish. Although new memories are rare, this section will cover several data storage techniques that show promise and/or are beginning to enter the consumer market.

1.3.1 Phase-change memory

Phase-change memory uses the rapid reversible amorphous-to-crystalline phase-changing ability of chalcogenide alloys to switch the resistance of a given memory cell.[2] When electrically initiated, a resistor is used to rapidly heat the chalcogenide alloy to a temperature in which a phase change will occur. The general device structure is shown in Figure 1.3. When starting in a high resistance amorphous state, a low resistance state can be programmed into the cell by heating the active region for a length of time and to a temperature necessary to crystallize the alloy. Once crystallized, the amorphous state can be regained by a shorter and higher temperature pulse of energy. This pulse melts the material and allows it to cool quickly enough to regain the glassy amorphous state. The programming techniques and I-V characteristics can be seen in Figure 1.4.

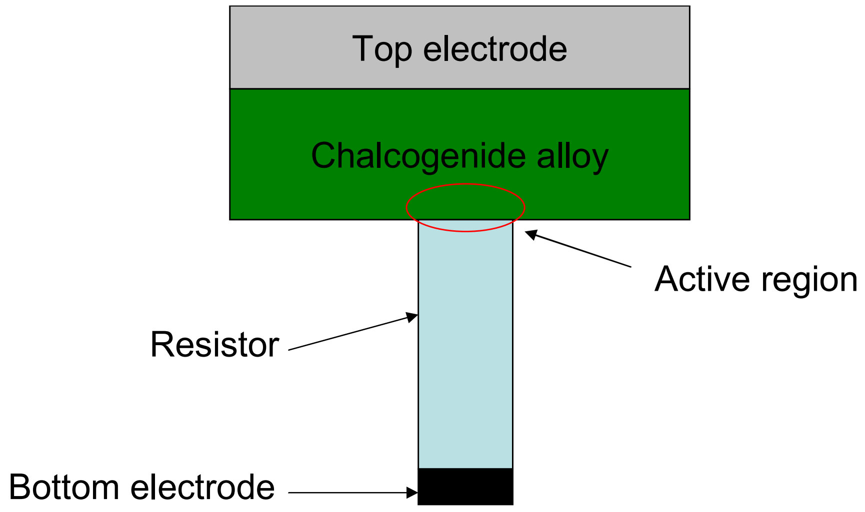

Figure 1.3 Storage element for phase-change memory.

The first reports of electrically-initiated phase-change memory were given by Ovshinsky in 1968.[3] Improvements over time have increased the viability of these devices which now show long cycle life, low energy requirements for switching, and high data densities. Challenges such as low volume manufacturability, cross talk, and device reliability hinder this technology from competing with flash memory.

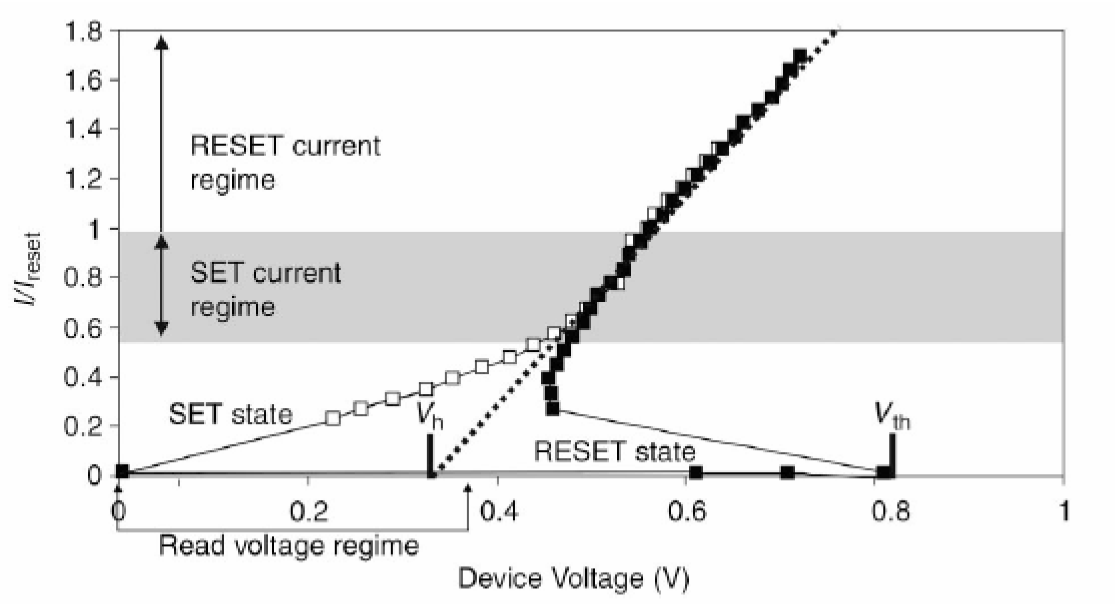

Figure 1.4 I-V characteristics and programming techniques of a basic phase-change memory cell.[2]

1.3.2 Ferroelectric RAM

Ferroelectric RAM (FeRAM) uses ferroelectric material which exhibits a spontaneous electrical polarization that can be reversed or reoriented by the application of an electric field.[4-7] The ferroelectric material in the form of a thin film is sandwiched between two electrodes creating a capacitor-like memory cell (Figure 1.5). A voltage is applied to the plates of this capacitor, and the ferroelectric film is polarized in one of the two possible net spontaneous polarization states. Once the bias is removed, the state is stable. To regain the previous polarization state, an equal but opposite voltage is applied. When the application of a writing pulse occurs, a charge pulse is drawn from the electrical circuit and stored in the capacitor. The memory state of the cell can be read by sensing the presence or absence of this switching pulse when the switching electric field is sent to the ferroelectric capacitor. Consequently, the reading of the state destroys the information stored, and refreshing of the cell is required.

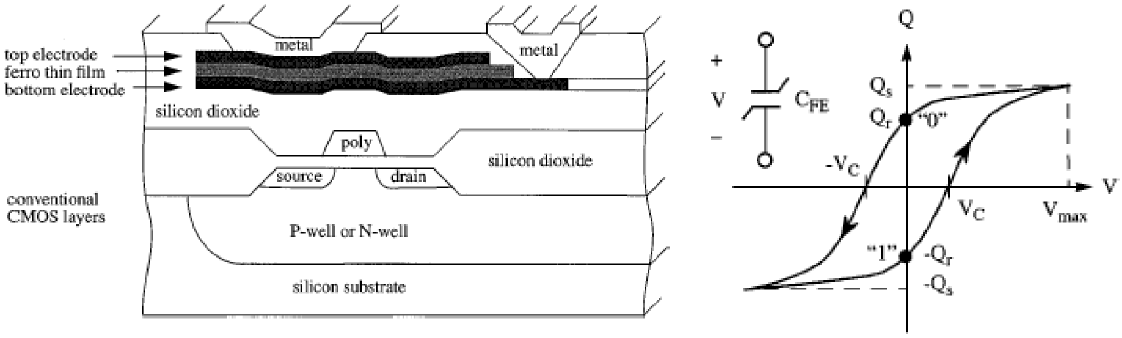

Figure 1.5 Structure and hysteresis curve of FeRAM memory.[7]

The most commonly used ferroelectric materials in FeRAM memory are multi-metal oxides with perovskite substructures such as PZT ($PbZr_xTi_{(1-x)}O_3$) (x = 0.2-0.5), SBT ($Sr_{(1-y]}Bi_{(2+x)}Ta_2O_9$) (x and y are small), or BLT ($Bi_{(4-x)}La_xTi_3O_{12}$) (x is small). Platinum and a few conductive oxides such as IrO_2, $SrRuO_3$, and RuO_2 are commonly used as electrodes due to their barrier properties, high crystallization temperatures, and lack of fatigue.

FeRAM exhibits high write/read speeds comparable to DRAM. It is a nonvolatile solid-state storage that can be easily embedded in large-scale logic circuits with low power requirements. Processing complexity and the same scalability issues that plague the traditional entrenched technologies have hampered the development of this memory.

1.3.3 Magnetoresistive RAM

Magnetoresistive RAM (MRAM) is a high-speed nonvolatile high-endurance memory that stores information in the form of magnetic polarization.[8] It uses a magnetic tunnel junction (MTJ) in conjunction with standard silicon-based electronic circuitry. As can be seen in Figure 1.6, the structure is relatively complex but highly scalable from a manufacturing standpoint. The MTJ consists of ultra-thin dielectric layers sandwiched between two ferromagnetic conducting layers. The resistance of the junction can be high or low depending upon if the magnetic moments of the two ferromagnetic layers are parallel or antiparallel. To read the state of the device, the isolation transistor is opened, and a current is passed through the MTJ.

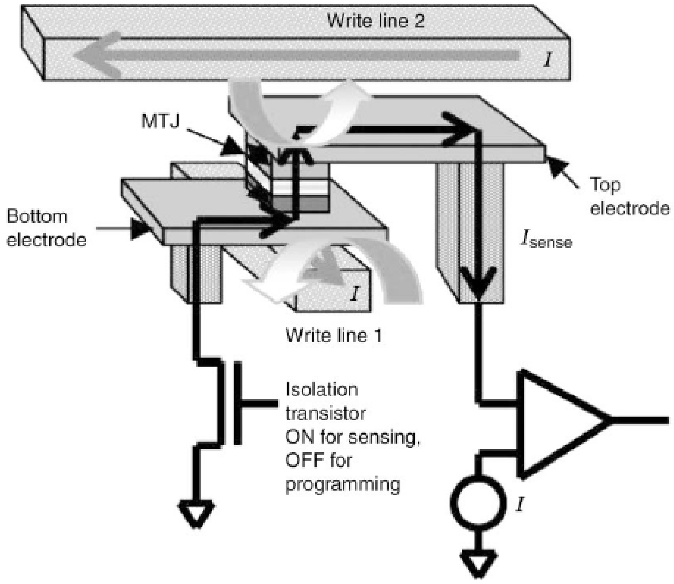

Figure 1.6 Structure of a MRAM cell.[8]

MRAM offers highly sought-after attributes that are currently realized only by separate traditional technologies. The quick read/write times of MRAM are competitive with SRAM, and the small size of MRAM is competitive with DRAM. The nonvolatility and endurance of MRAM can be compared to HDD storage without its moving parts. Consequently, MRAM has the potential to replace these memory devices and become the so-called universal memory. However, the high cost and complexity of fabrication will need to be overcome before high-volume production and industry acceptance is accomplished.

1.3.4 Nano-crystal memory

As semiconductor scaling enters the 45 nm node technology, researchers believe that nano-crystal memory will succeed flash memory and become the dominate data storage for numerous devices.[9,10] Similar to flash memory in several aspects including write/read/erase operations and general architecture, nano-crystal memory shows promise of higher storage density, faster writing/erasing times, higher durability, and longer retention times. This increased performance is attributed to the replacement of the polysilicon or nitride floating gate with discrete nano-sized particles (Figure 1.7). The separation of the nano-crystals allows for less lateral leakage currents, which are common in flash memory cells. This is due to the localized trapping on each nano-crystal. If a leakage path due to a defect occurs, only the single nano-crystal node located near this area will lose its charge.

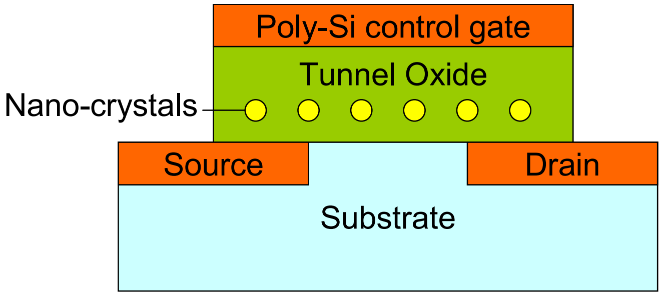

Figure 1.7 Schematic of a nano-crystal memory cell.

There have been several cell structures cited that utilize different self-assembly methods for the nano-crystal layer.[11-13] There have also been improvements in performance by using metal nano-crystals instead of semiconductor materials.[14,15]

1.4 Introduction to conductance switching in thin films

New data storage materials and concepts have increasingly gained interest in recent years. Conductance or resistive switching in a two-terminal device (generically called resistive random access memory (RRAM)) is a memory technology in initial development. Several companies (Unity Semiconductor Corp., Tegal Corp., Samsung Electronics Co. Ltd., Sharp Corp., IBM, LSI Logic Corp., Matsushita Electric Industrial Co. Ltd., Winbond Electronics Corp., and Sony Corp.) and many research groups are investigating this type of data storage. However, as of today, there are no products in the consumer marketplace.

In general, the device structure is simple. A two-terminal nonmagnetic nonvolatile memory comprised of a sandwich structure with metallic electrodes is the basic design.

Requiring relatively few mask layers for fabrication, this memory is potentially ideal since its size can be made arbitrarily small. The simple and highly scalable structure of this memory can be seen in Figure 1.8. The key feature of this memory is the ability to switch the resistance or conductance of the cell by simply applying a voltage or current pulse across the storage medium. Switching in both organic and inorganic materials has been cited. The conductance state of the device is then measured by a small bias, which does not perturb the state significantly, and if the system is disconnected from the electric circuit, the conductance state can remain stable. The ability to access several conductance states allows the storage of multiple bits per memory cell, which will drastically increase data storage densities.

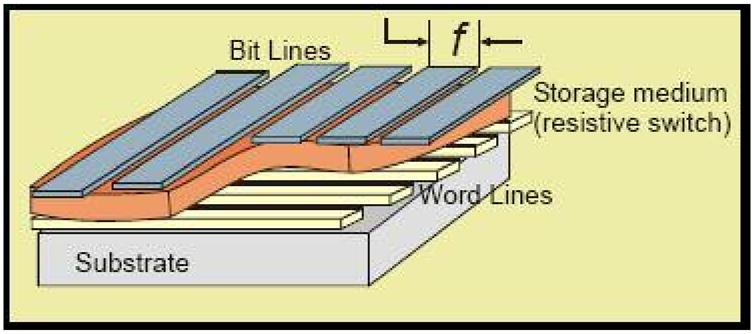

Figure 1.8 Basic structure of RRAM device.

There is a vast history of conductance switching and other memory effects in these thin film structures. Uses of various materials, device structures, and programming techniques have been cited since the 1960’s. Despite the many variable parameters involved, there has been a remarkable agreement between researchers as far as results. In contrast, conclusions and explanations for these results are widely disagreed upon. In the next chapter, the history of thin-film conductance switching including the many theories and proposed device structures will be discussed.

CHAPTER 2

HISTORY OF CONDUCTANCE SWITCHING IN THIN FILMS

Conductance or resistive switching, generically termed RRAM, has been observed in thin-film structures since the 1960's in both inorganic [1,3,16-45] and organic [46-87] materials. By simply applying a potential difference across the active layer, a conductance state can be programmed into the device and then read by applying a smaller bias which does not disturb the state. Despite the many variable parameters involved (materials used, thicknesses of films, programming techniques, etc.), data from many research groups (in the form of I-V characteristics, successful switching cycles, nonvolatile retention of states, etc.) have been in remarkable agreement. Still, the conclusions and explanations for the mechanism(s) responsible for the memory phenomenon are far from agreement and are still under intense debate today. If an all-encompassing theory is proposed to explain the mechanism(s) at hand, it must explain and account for the vast number of evidences that have been found in the many materials and thin-film structures over the past 40 years. Understanding the history of this research can give great insight to what the future holds for this technology.

2.1 Switching in inorganic materials

A wide variety of inorganic materials have shown the ability to switch between conductance states when sandwiched between two metal electrodes in a metal-insulator-metal (MIM) structure. Experiments have been done on many inorganic materials such as metal oxides,[16-20,28,30] amorphous semiconducting chalcogenide glass alloys,[3] Ge-Ge-T1 systems,[21] and ZnSe-Ge heterojunctions [16]. Insulating layers from 10 to 2000 nm [35] placed between many different metal electrodes have been cited to show switching effects and other memory phenomena. Several mechanisms have been cited such as field-induced structural changes (ie. phase transformations),[3,42,43] metallic filament formation,[18,34] elimination of either positional or compositional disorder,[44,45] and charge trapping by impurities [1]. Although there have been many publications and research groups that have contributed to the study of these electrical phenomena, the early history of MIM devices is dominated by a few noteworthy groups. A review of their contributions and a comparison of their viewpoints on this subject will be presented.

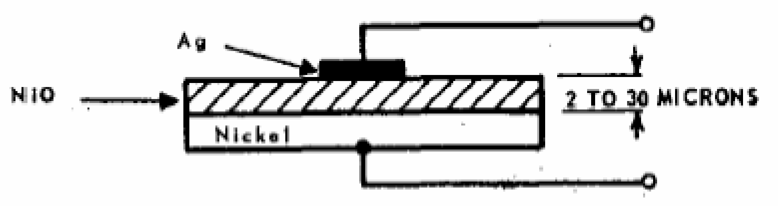

Figure 2.1 Structure of a MIM type device used in the studies of Gibbons et al.[18]

One of the first observations of reversible switching between two conductance states in an inorganic structure was through the use of an oxidic semiconductor thin film by Gibbons et al. in 1964.[18] In these studies, a NiO film with thicknesses ranging from 2 to 30 microns was sandwiched between a top Ag and bottom Ni electrode and shown to switch between two conductance states with a difference in current of about 5 orders of magnitude (Figure 2.1). In the low conductance state, the typical off resistance was cited to be 100 to 200 MΩ and in the high conductance state the typical on resistance was 10 to 20 Ω. Filament formation was the mechanism suggested to be responsible for the switching phenomenon seen in these devices. As described by Gibbons et al., filaments are metal-like bridges that partially or completely bridge the insulator gap thereby creating a pathway between the two electrodes. In his experiments, the filament material was Ni and in the "on" state, Ni atoms were arranged into a conducting bridge. To attain the "off" or highly resistive state, high current was applied to break the filament just like an electrical fuse. Once the filament(s) have been broken, and switching the device back to the on state was desired, much less power was needed to repair the broken filament (how a medium bias repairs a broken filament is never described). Therefore, the threshold voltage or voltage needed to attain the on state was at a much lower value compared to the very first switch. This widely observed characteristic has been commonly known as "forming". Forming occurs when a fresh device is biased at relatively high values for a relatively long time and is believed to allow the filaments to be formed for the very first time (requires more energy than regular switching).

An interesting report by Simmons and Verderber followed in 1967.[1] They investigated a MIM structure comprised of an Al cathode, Au anode, and a SiO_x insulating layer. Their studies propose that the forming process introduces gold ions into the thin-film insulator, which then results in a change in the electrical current of the device. The ions are believed to create a broad impurity band in the SiO_x layer. This band is able to store and release charge thereby modifying the potential barrier of the device.

When the bias applied to the device is in excess of the bias needed for maximum current, charge is injected into the depletion layer. Then, the rapid reduction of the bias, in conjunction with band bending, sends charge to the center of the insulator by phonon-assisted tunneling. This gives rise to a low conductivity state. Several important experiments were conducted involving temperature dependence, switching speed (dynamic characteristics), and general I-V characteristics. Their work represented a material dependent theory which was found later to weaken their claims.

An all-encompassing model for a filamentary mechanism was presented in 1970 by Dearnaley et al.[35,37] This theory contradicts the work by Simmons and Verderber but supports the findings by Gibbons et al. Several oxides of Si, Ta, Zr, Ti, together with halides of CaF_2 and LiF were investigated with electrodes made from Cu, C, Si, and Ni. The work describes the growth and thermal rupture of many conducting filaments through the insulating layer and how this mechanism accounts for the observation of voltage-controlled negative resistance, electron emission, electroluminescence, and other memory phenomenon. Both groups agree that there is a forming process that needs to occur before switching can take place, but the absence of anode material in the insulating layer and long-term stability of the memory states induced a rejection of the Simmons and Verderber model. Also, localized electron emission from damaged areas in the top electrode and step-like increments in current during switching suggested an inhomogeneous insulator for which a band theory could not apply. Calculations for the events of filament rupture due to Joule heating were conducted. The mean resistance per filament was estimated to be about $2.5 \times 10^7\ \Omega$ and the number of filaments to be about 5

× 10^6 per cm^2. The reformation of the filament was suggested to depend on several factors such as local temperature, electric field, and possible space charge effects, but the precise conditions were not specified. Finally, the switching phenomenon in this model allows for the use of more materials than just amorphous oxide films.

In 1971, Sutherland [36] reviewed and expanded upon the work by Simmons et al. and Dearnaley et al. by conducting several experiments using zinc sulphide as the inorganic material ranging from about 30 to 300 nm in thickness and electrodes made from a variety of metals including Au, Ag, and Al. Combining the theoretical models, he declared that it is impossible to conclude the precise nature of the filaments. He suggest that each filament consists of a chain of positive centers that do not conduct in an ohmic way but conduct by a similar conduction mechanism cited by Simmons and Verderber.

Although much theoretical groundwork was presented in the 60's and 70's, more theories and results followed through the 80's and 90's. Sharp et al. added new ideas and experimental evidence to the metallic filament theory.[88,89] He gave an in-depth description of the metallic filaments rupturing and reforming process. Still, even more recently published works involving several new oxides such as BaSrTiO3, SrZrO3, SrTiO3, CaNb2O7, and Ta2O5 [17] have been conducted. A charge transfer and trap mechanism is believed to affect the current in these devices. Models have been developed that propose charge accumulation by charge traps in small domains,[38] electron accumulation at the electrode insulator interface,[39] and the creation of crystalline defects by electric field [40,41]. Many new inorganic thin-film memory devices have accumulated over the past several years without a unifying theory of the mechanism responsible for the memory effects observed.

2.2 Organic-based devices, recent structures, and mechanisms proposed

Organic thin-film memory has been investigated since the late 1960's in both thermally-evaporated [46,69,80] and solution-processed [61,63,68,90-93] thin films. The ability to tailor the properties of organic materials as well as low fabrication cost and high mechanical flexibility give many advantages over their conventional inorganic counterparts. New device structures and switching mechanisms have been cited. Switching has been observed in multilayer devices (metal/organic/metal /organic/metal),[62,66,87] single-layer devices,[47,49,65] monolayers of material,[70,94,95] and individual molecules [74-77,96]. Switching has been observed by macro-scale contacts and by the use of an AFM tip [61,70,96]. Still, the new data produced resembles the data of the past, and there is still a disagreement on an all-encompassing theory of the mechanism responsible for switching.

The first thermally evaporated organic memory device by Szymanski et al.[80] was made from an Al-tetracene-Au sandwich with the middle layer being 600 nm in thickness. Two conductance states were observed. The on state (low resistive), said to arise from space charge conduction, exhibited a current value that was five orders of magnitude higher than that of the off state (high resistive). The I-V characteristics of this device can be seen in Figure 2.2. No mechanism was cited.

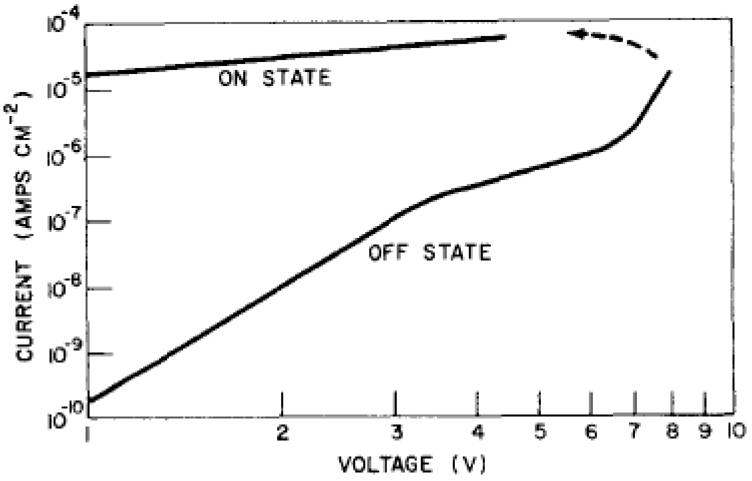

Figure 2.2 I-V characteristics of the Al/tetracene/Au device by Szymanski et al.[80]

The use of polymers in memory devices soon followed in the early 1970's.[68-70] Several types of memory phenomena have been observed in solution-processed films such as spun-on polymers [61,63,68,91-93] and sol-gel materials [90]. Using solution-processed organic material allows for high-volume production and simplified fabrication techniques such as stamping, blade coating, ink-jet printing, and roll-to-roll processing increasing the commercial viability of the devices.[97,98] Organic polymers have shown distinct bistable states with reported current ratios ranging from 10^3 to 10^7.[61,63,68-70,92,93] Many different pristine metal-polymer-metal structures,[68,70,92,93] as well as polymers doped with gold nanoparticles [61,63,99,100] or C60 mixtures, have shown this electrical bistability. Observations of these memory effects when using a variety of polymers and metals in metal-polymer-metal structures show that this switching effect must be, to some extent, material independent.

Extravagant mechanisms such as conformational changes (Figure 2.3),[18] redox mechanism,[92] and electric-field-induced charge transfer between polymers and metal nano-particles are just some of the recent theories introduced by the numerous works of the last 10 years. Their data which is described in the form of I-V characteristics, successful switching cycles, and nonvolatile retention of states have been in remarkable agreement. Still, the mechanisms proposed to govern these results are very different. Also, the material dependence of these theories drastically reduces their validity. In addition, several authors have claimed that multilayer devices (requiring the insertion of a metal island layer)[55,101-103] are needed to observe the switching effect. This assertion has been challenged by groups observing the same switching in a single-layer [57] structure when using the same materials (Figure 2.5).

A write-once read-many-times (WORM) memory has also been shown using both the polymer polyethylenedioxythiophene (PEDT): polystyrene sulphonic acid (PSS) (PEDOT) [91] and polyaniline doped with camphorsulfonic acid (PANI/CSA). In these fuse-type memory devices, a critical voltage is applied across the polymer thereby permanently changing its electrical characteristics. This is sufficient for some applications, but rewritability is essential for most data storage applications.

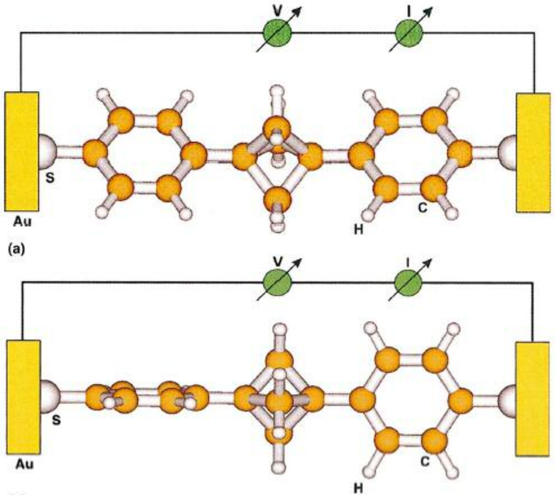

Figure 2.3 A schematic of a conformational switching of a Au/π(benzenethiol)-σ(bicyclopentane)-π(benzenethiol)/Au device.[104]

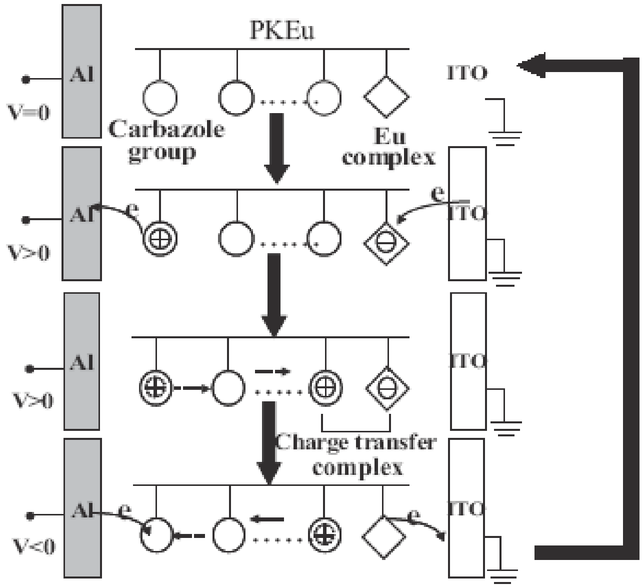

Figure 2.4 Redox mechanism controlled by a donor acceptor system.[92]

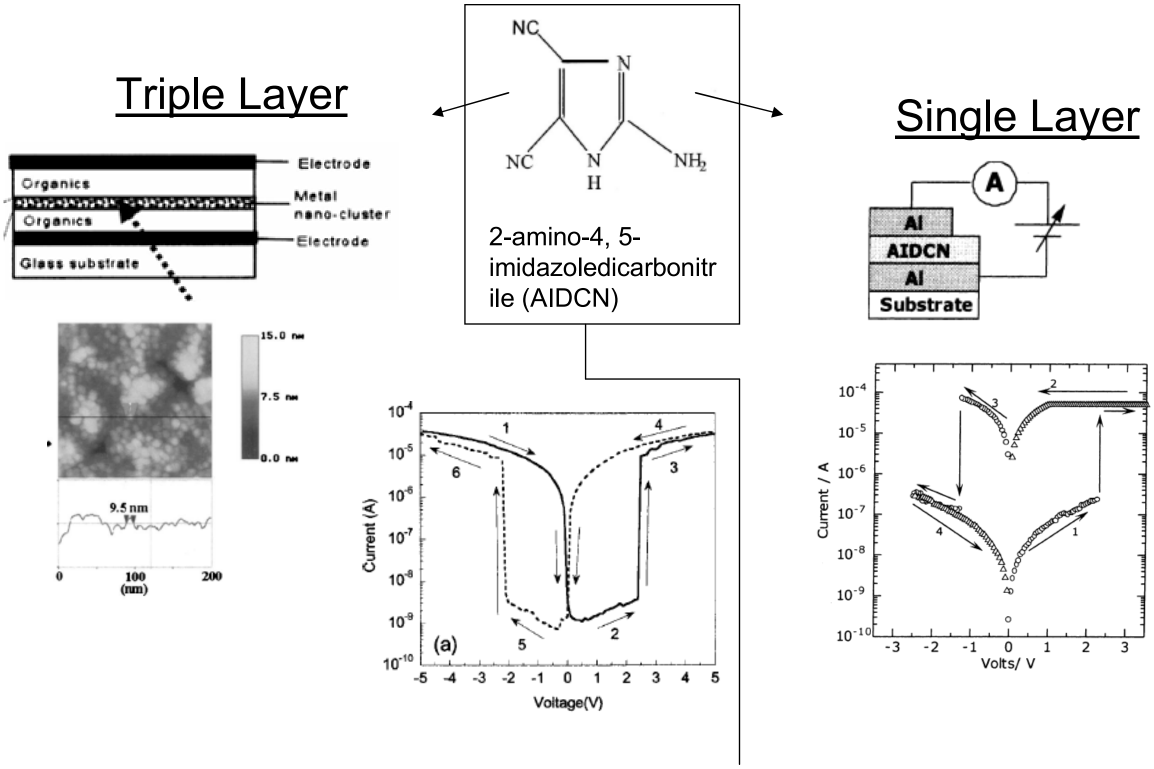

Figure 2.5 Comparison of data taken from a multilayer device (right) and a single layer device (left) using the same materials for organic and metal.[57,103]

CHAPTER 3

FABRICATION TECHNIQUES, MATERIALS, AND SCANNING PROBE MICROSCOPY (SPM)

3.1 Device fabrication

All devices showing conductance switching and other memory effects were fabricated by well-known OLED fabrication methods. In most cases, the substrates used for these devices consist of a 100 to 250 nm thick layer of ITO (sheet resistivity of about 15 Ω/square) on soda lime glass that measures 1mm in total thickness. Substrates were acquired from multiple sources to investigate if the memory phenomenon was substrate/anode dependent. Several companies (i.e. Colorado Concept Coatings LLC, Nitto Denko, etc.) and governmental agencies such as the Defense Advanced Research Projects Agency (DARPA) were common sources for ITO substrates in our experiments. The substrates were cut into 1 in.^{2} pieces, cleaned using consecutive ultrasonic baths of acetone, methanol, and isopropanol for 30 min each, and dried in static-free nitrogen gas. The ITO anode was patterned either with a thick silicon oxide insulating layer or by etching the ITO with an acid bath. As switching in thin silicon oxide films has been observed, it should be pointed out that device performance was the same for both patterning processes, demonstrating that the oxide layer in our studies does not contribute to the device's electrical behavior. After patterning, the same cleaning procedure was implemented again. In addition, air plasma ashing for 2 min was used to remove any residual organic contamination and to allow further enhancement of the ITO work function.

The substrates were then ready for the application of organic layers which were completed through either solution-processing techniques or thermal vapor deposition. Solution processing of organic layers was commonly completed by spin coating, blade coating, or printing techniques. The thermal vapor deposition of organic layers was completed at a pressure of about 1.0×10^{-6} Torr with the use of an Angstrom Engineering vacuum evaporation system integrated into a nitrogen-filled glove box. Organic materials were deposited at rates from 0.2 to 3.0 A/s to investigate the effects of deposition rates on switching ability, but a rate of 1 A/s was most commonly used for organic films. While depositing, thicknesses were monitored with a pre-calibrated quartz crystal oscillator. In addition, calibration and further thickness measurements were carried out using AFM or a Dektak 3030 surface Profilometer.

After completion of the organic layers, a cathode was commonly deposited by thermal evaporation. Cathode materials used in these experiments consisted of metals such as Ag, Mg, Al, Au, Cu, or their alloys in multiple ratios. A thermally-evaporated LiF layer was also used in some devices due to its common presence in many highly-efficient OLEDs as an adhesion/electron-injection layer. The layer is deposited between the organic layer and metal cathode and ranges from 0.1 to 2.0 nm in thickness. We also investigated solution-processed cathodes made from Ag nanoparticles. These films were created by inkjet printing or solution dropping from micropipette. When Ag nanoparticles were implemented, baking at 100°C for 8 h was necessary to remove solvents thereby increasing conductivity. Note that this temperature is not sufficient to get rid of the polymer binder. Moreover, such temperature is far too low to transform the Ag film into a fully conductive metal.

Although most devices were electrically and optically characterized by using thermally-evaporated or solution-deposited top electrodes, some devices were tested with the use of an AFM tip as a top electrode. The use of AFM and conductance AFM (CAFM) allowed nanoscale probing of electrical characteristics and direct investigations of the mechanism which makes conductance switching possible.

All fabrication steps were completed with extreme care, and all precautions were taken to keep substrates and layers free of dust and particle contamination. Cleanliness is a very important part in the fabrication of these thin-film structures. The organic layer or insulating layer is extremely thin. The total thickness of the layers is on the order of 100 nm. Homogeneous thicknesses and interfaces cannot be taken for granted, for the ratio of the lateral dimensions to the thickness of the film is typically about 10,000:l. This relatively large surface area can be subjected to thousands of dust particles ranging from 1 to several 10's of microns in size. Particles are commonly found in such great numbers when substrates are not properly cleaned. So common, that Tang et al. proposed that all memory effects and conductance switching are a direct result of their infiltration.[56] Our substrates and layers were inspected by the use of optical microscopes and interferometery techniques ensuring the absence of such particles.

After fabrication, the devices were immediately transferred from vacuum to a nitrogen-filled glove box where electrical characterization was performed at room temperature (except for experiments involving temperature dependence). The devices' general I-V characteristics were investigated with a Keithley 2400 Sourcemeter connected to a PC via general purpose interface bus (GPIB). Making contact to the thermally-evaporated electrodes was generally accomplished with indium-tipped clips which provide a soft but secure electrical contact. To conclude that the switching effect found in our devices was independent of this contact point, several other metal clips were used such as Cu, Ag, and steel. In addition, the use of Ag paste and copper tape in place of a clip was also investigated, with all contacts showing similar results.

3.2 Materials and device structure

Both small molecules and polymeric organic materials were investigated for conductance switching and memory effects. Several OLED material classes were used including electron-transporting, hole-transporting, charge-blocking, and emissive materials. These materials were employed in single-layer and multilayer devices in the quest to uncover any type of material dependence on the switching mechanism (discussed in Chapter 5). Many of the devices fabricated for conductance switching experiments were regularly structured OLEDs. The co-existence of normal electroluminescence and conductance switching was possible in these devices when an appropriate bias (one above the operational voltage of the OLED) was applied. The data presented in the following chapters has been taken from several different structures and materials, and they will be indicated in each case. There is no specially-featured device structure for the conductance switching experiments reported in this dissertation.

3.3 Characterization of surface morphologies

SPM has become an indispensable tool when studying a wide range of materials properties in the nanoscale regime. Among the increasing number of SPM techniques, AFM has been the most widely used. Both the morphologies of the ITO-covered substrates and the subsequent organic films were characterized using a Digital Instruments multimode, Dimension 3100, Nanoman SPM purchased from Veeco Instruments, Inc. The AFM employed in our studies uses an optical detection mechanism to sense the surface of the sample which is depicted in Figure 3.1. A laser beam is reflected off the back of a cantilever, which has a very small protruding tip facing the surface whose radius of curvature ranges from 10 to 200 nm that is attached to a piezoelectric ceramic scanner. As the cantilever is scanned over the sample, it is deflected up and down due to the local profile of the surface. This bending in the cantilever is then detected through the movement of the laser beam. The reflected laser light is directed to a position sensitive double photodiode, and the level of the deflection is compared to a predetermined set-point value. The angular displacement of the cantilever results in one photodiode collecting more light than the other photodiode, thereby producing an output signal (the difference between the photodiode signals normalized by their sum) which is proportional to the deflection of the cantilever. This method can detect cantilever deflections of <0.01 nm. Depending on the mode of operation, the piezo-scanner moves the tip up and down and records its movement (constant-force mode) or just records the deflection of the tip as detected on the photo-detector without moving the piezo (constant height-mode). The dominate force contributing to the deflection of the AFM cantilever is the interatomic van der Waals forces. The AFM can operate in three different modes: contact mode (Figure 3.2), non-contact mode, and tapping mode (Figure 3.3). To measure hard surfaces like ITO-covered substrates, contact mode was used while the extremely soft surface of most organic thin films were characterized using tapping mode.

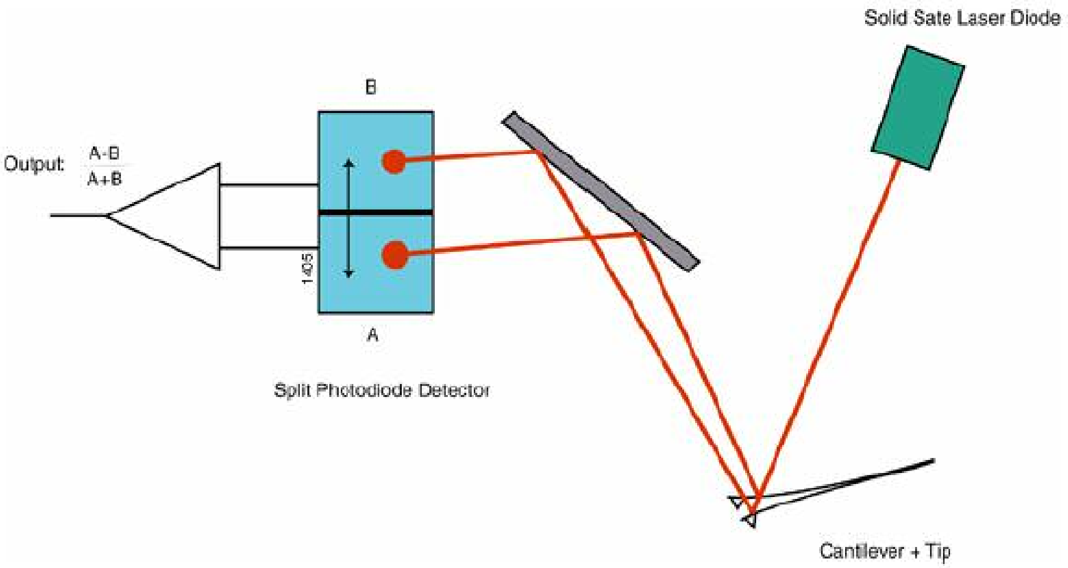

Figure 3.1 Schematic of basic SPM optical-detection system.

In contact mode, the tip scans over the sample in the repulsive force region (Figure 3.4) while physically touching the surface. The tip should have a lower spring constant than the effective spring constant holding the atoms of the sample material together. This will allow the tip to properly bend to accommodate the changes in the morphology of the sample. There are two types of forces present between the tip and the sample. There is a capillary force due to the thin water layer present in the ambient environment and a force due to the spring constant of the cantilever itself. The total force that the probe exerts on the sample is the sum of these two forces which must be balanced by the repulsive van der Waals forces. The magnitude of the force usually applied to the surface is between 10^{-8} N and 10^{-6} N. The former value is the amount of force when the tip is being pulled away from the surface, and the latter is the force when the tip is pushing hard on the sample.

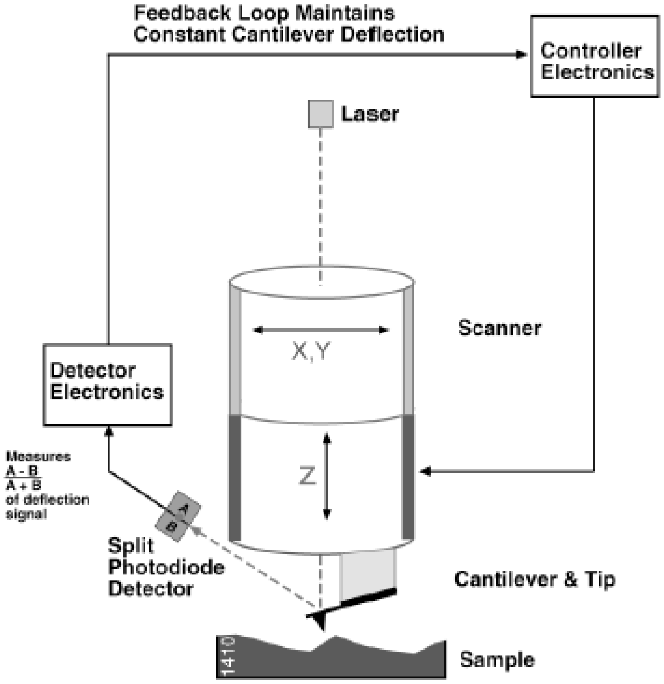

Figure 3.2 Diagram of AFM in contact mode.

In tapping mode or sometimes called intermittent-contact mode (IC-AFM), the tip is oscillated at a particular frequency near the repulsive regime (Figure 3.4) of the surface. There, it lightly taps the surface of the sample (Figure 3.3). This enables imaging of soft samples such as organic thin films without damaging the structure of the surface of the sample. The applied force is typically less than ~10^{-10} N. In order to sustain the tip a distance from the sample, the cantilever must be stiffer than those used in contact mode. The morphology of the surface is detected by changes in the resonant frequency or vibration amplitude.

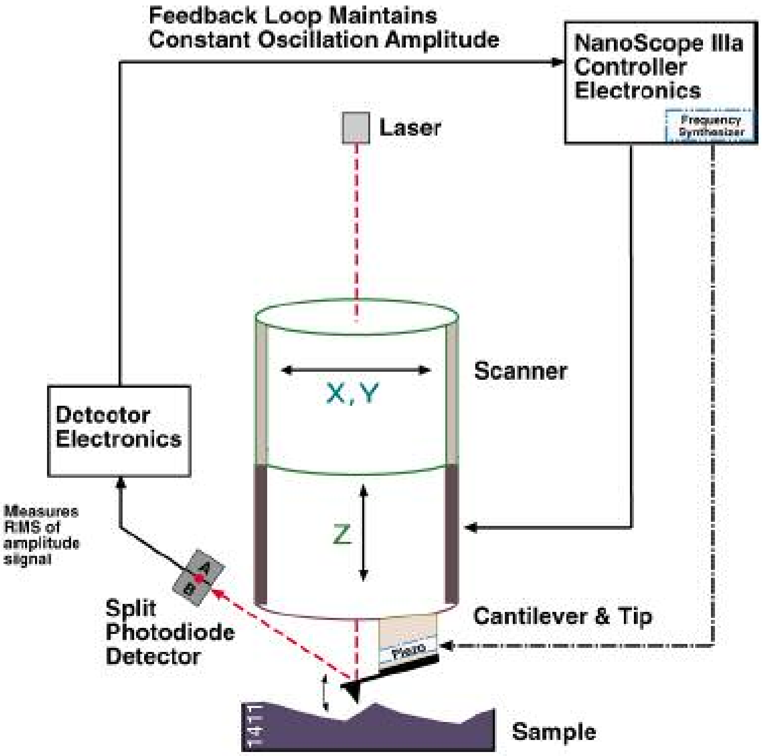

Figure 3.3 Diagram of AFM in tapping mode.

There are several advantages and disadvantages for both contact and tapping mode AFM. The advantages of contact mode over tapping mode are that higher speeds and atomic resolutions can be attained. A few disadvantages are that lateral (shear) forces can distort features, and there is normally high tip-to-sample force interaction due to capillary forces from the absorbed fluid layer. The advantages of tapping mode are higher lateral resolutions for most samples, and there are lower contact/lateral forces which equates to less damage to soft materials (no dragging of the tip). With these advantages and new techniques to increase scanning speeds, tapping mode AFM is used increasingly for many surface morphology characterizations.

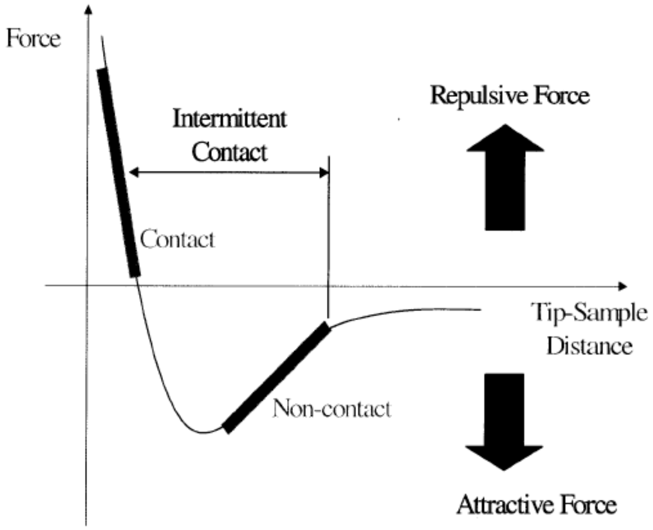

Figure 3.4 Van der Waals forces as a function of tip-to-sample distance. There are three areas of application: contact, intermittent contact (tapping mode), and non-contact.

3.4 Atomic force microscopy (AFM) contact probe as cathode

To further explore the electrical properties of these thin-film structures, the use of an AFM contact probe was implemented as a top electrical contact. The characteristics of very specific areas of the organic-covered anode/substrate area were investigated. CAFM and TUNA can be used as valuable current-sensing techniques for the conductivity variations in organic thin films. The electronics for these techniques are well integrated in small application modules, which can be readily mounted on the Digital Instruments multimode, Dimension 3100. CAFM can be used for mapping variations in electrical conductivity of materials with current sensitivities in the range of 1 pA to 1 µA (imaging mode). In imaging mode, an electrically-conductive tip is scanned over the sample surface as a feedback loop keeps the deflection of the cantilever constant while the height of the sample is measured (Figure 3.5). During scanning, a DC bias can be applied between the tip and the sample. A low-noise linear current amplifier senses the resulting current passing through the sample as the topography image is simultaneously obtained. The observed current can be used as a measure for the local conductivity or leakage currents of the thin film in question. The abilities of our CAFM module also allow for the collection of I-V data at a single location (spectroscopy mode). In order to obtain this I-V spectra, the imaging scan is stopped, and the tip is held in a fixed location while the sample bias is ramped. When collecting I-V data, the start and end voltage of the ramp, ramp direction, and ramp rate can be adjusted allowing for a complete characterization of the electrical properties.

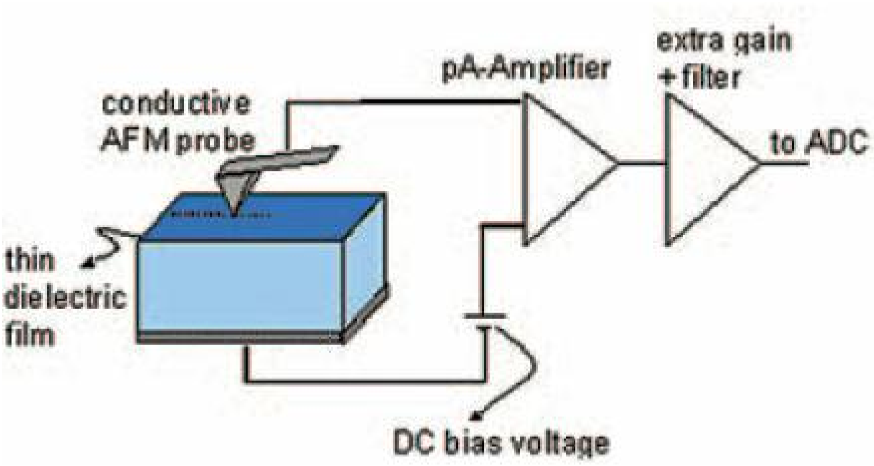

Figure 3.5 Schematic representation of the TUNA and CAFM setup.

TUNA measures especially low currents on low-conductivity samples. As with CAFM, a DC bias is applied between the sample and the conductive tip while the tip is scanning the sample in contact mode. A linear current amplifier with a range of 60 fA to 120 pA senses the resulting current passing through the sample. In this way, the sample's topography and current are measured simultaneously, enabling direct correlation of a sample location with its electrical properties. The noise level of the TUNA module allows one to perform extremely sensitive current measurements. In addition, the TUNA module also exhibits the ability to take local measurements of current-voltage spectra on the sample.

CHAPTER 4

CURRENT-VOLTAGE (I-V) CHARACTERISTICS

4.1 General I-V characteristics

The switching behavior in organic thin films can be easily illustrated by the use of I-V sweeps. As a voltage is applied across the organic film, the current is measured through the use of an in-series resistor. Figure 4.1 depicts the electrical switching of an ITO/PVK/Al device. The middle layer was formed by spin coating the polymer PVK from a chloroform solution resulting in a film thickness of about 70 nm.

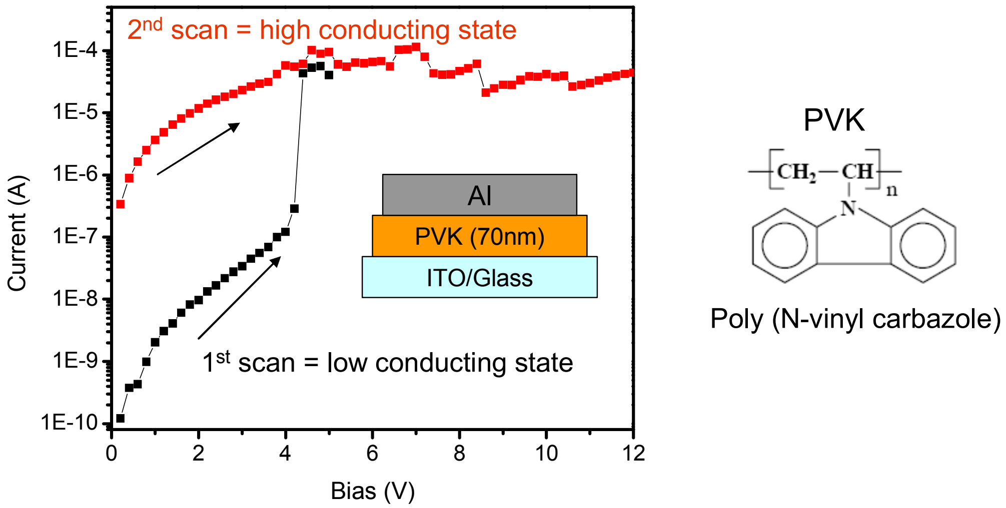

Figure 4.1 Two I-V scans indicating two possible conductance states in an ITO/PVK/Al device. The chemical structure of PVK is indicated on the right.

The first voltage scan from 0 to about 5.5 V indicates a low conductance state. Towards the end of the first scan, a higher conductance state is programmed into the device. After the first scan is completed, a second scan from 0 to 12 V is conducted. The second scan shows that the device is now in a higher conductance state. This state is more than 3 orders of magnitude higher in conductivity than the initial state. Accessing the conductance state of the device without perturbing its state can be accomplished by applying a low bias across the device such as 1 mV to 2 V. Although this example of switching is shown using PVK as an active middle layer, many other materials have shown similar switching and memory effects. In addition, the reliability of the switching, current values, and overall performance varies from device to device (even with the same device structure). Although there are inconsistencies between devices, there are many tendencies and predictable events which provide evidence for the mechanism(s) behind the switching.

4.2 Detailed programming techniques of multiple conductance states

Section 4.1 provided an introduction to the conductance switching found in our devices. Understanding the details of the many regions of the I-V curves produced by these experiments can give insight to a possible mechanism. As stated before, the switching mechanism shows minimal material dependence. In this section, the detailed reading and programming of an ITO/poly[2-methoxy-5-(2’-ethyl-hexyloxy)-1,4-phenylene vinylene] (MEH-PPV)/Al device’s multiple conductance states is done by applying certain biases (scan always in the forward direction with ITO positive).

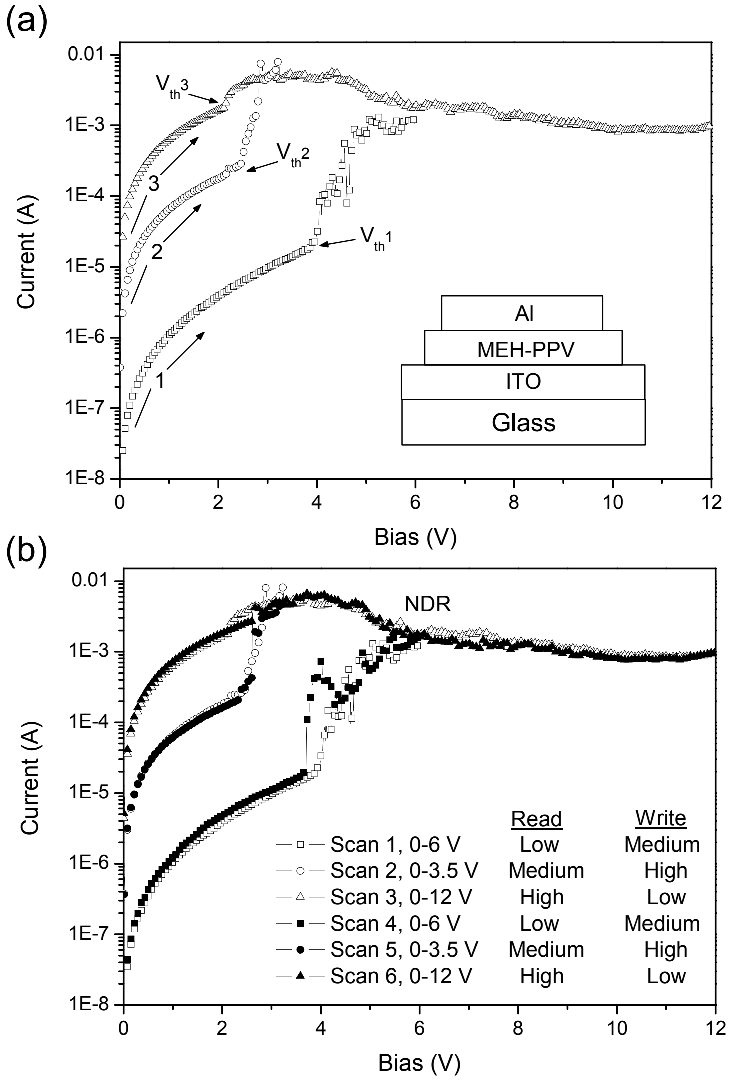

Figure 4.2 (a) Bias scan 1 (□) 0 to 6 V, scan 2 (○) 0 to 3.5 V, and scan 3 (Δ) 0 to 12 V depict three of the many possible conductance states of an ITO/MEH-PPV/Al device. The location of V_{th} for each of these states is indicated. The inset shows the device structure. (b) Six current-voltage scans show the cyclic behavior of the switching between three distinct conductance states. A region of NDR can be seen when a given scan exceeds a peak conductance.

Reading of the device's conductance state is accomplished with an applied bias below a certain critical V_{th}. Below V_{th}, the device is stable and can be read repeatedly without changing the state of the device. An appropriate reading voltage for all states was typically found to be about 1 V or less. To program the device into a different conductance state, a bias higher than V_{th} is needed. The value of V_{th} is not constant but decreases for conductance states with higher current values. Once V_{th} is exceeded, the state of the device can be changed to a higher or lower conductance state depending upon the value of the applied bias with which the scan is ended.

To explain this further, Figure 4.2 (a) shows a single device exhibiting three different conductance states. These are the results of three consecutive I-V scans performed on the device, which differ by the voltage at which the measurements are terminated. In the first scan, indicated with open squares, the voltage is ramped from 0 to 6 V. At the beginning of this scan and below V_{th}, the current is low indicating a low conductance state. The current is also stable and increases with increasing voltage. Above V_{th}, the current becomes relatively unstable and abruptly increases in value, and it is in this region that the device switches to a higher conductance state. This can be observed in the second I-V scan (0 to 3.5 V, indicated by open circles) where the current in the region below V_{th} is at least an order of magnitude higher than the previous scan, thus demonstrating that the device has been programmed into a higher conductance state. During the second scan and once a new V_{th} is exceeded which is lower in value than the first conductance state's V_{th}, the current again increases rapidly, programming a third and even higher conductance state. In the third I-V scan (open triangles, 0 to 12 V) the current below V_{th} is much higher than previously measured, thereby demonstrating the multistable behavior of this device. There are several unique features noticeable in this state, such as the observation of a local current maxima, the lack of a predominant V_{th} (region of abrupt increase in current), and a region of negative differential resistance (NDR) where current decreases with increasing voltage. Although a small unstable increase in current can be seen around 2.1 V (indicating a weak V_{th}), the current does not abruptly increase with the same magnitude as in the first and second scans. This might indicate that a conductance state close to the highest possible in the MEH-PPV film has been reached. The voltage needed to change the conductance state of the device to a lower one is found in a region of NDR which occurs directly after the local current maxima of a given state. The farther the I-V scan is allowed to progress into the region of NDR, the lower the conductance state that will be programmed into the device. To show the possible cyclic behavior of this device, the third I-V scan was terminated at 12 V which programs the device into the conductance state originally observed by the very first I-V scan.

4.3 A continuum of conductance states possible

Many researchers have shown that organic memory devices are able to switch between two nonvolatile conductance states (termed bistable).[61,63,68-70,92,93] There has been only a few reports of organic devices showing more than two conductance states.[56,101] Even with these “sightings” of several states, no thorough explanation of how to access the states has been introduced. In the previous section, the programming of three distinct states was outlined. In Figure 4.3, sixteen nonvolatile conductance states are shown. The number of total possible states useable in application depends on the noise or reproducibility of a given state and its closeness to its neighboring states. In theory, a continuum of states is possible between the lowest and highest states of the device.

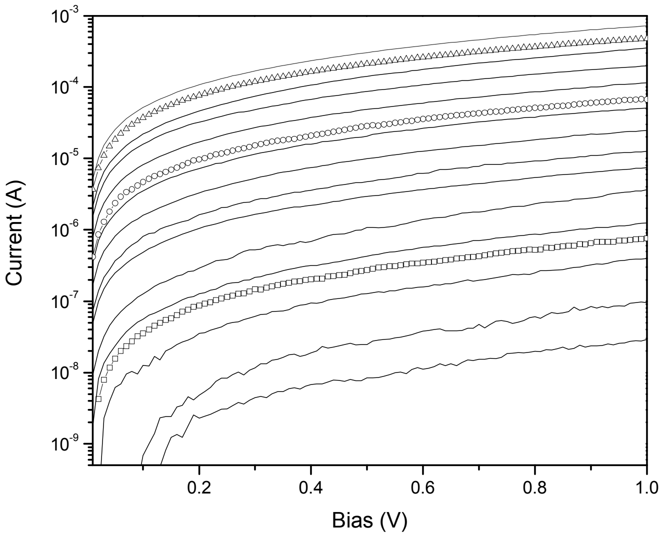

Figure 4.3 A demonstration of several conductance states at low read voltages (hinting that a continuum of states is possible). The programming voltages for these states are 3, 3.5, 4, 4.5, 5, 5.5, 6, 7, 8, 9, 10, 11, 12, 13, 15, and 17 V (from top to bottom). Once programmed, a scan from 0 to 1 V is used to read the state of the device.

The device used to generate the data shown in Figure 4.3 consists of the polymer MEH-PPV sandwiched between ITO and Al. The several states of this device were accessed by the use of an I-V scan starting at a 0 bias and ramping to an ending bias which depended upon the state trying to be accessed. Once the conductance state of the device was programmed, a reading sweep was performed that started at 0 V and ended at 1 V (thereby accessing the conductance state of the device). To begin the experiment, the device was programmed into the highest state attainable by sweeping to 3 V (not shown). This state was then read by a 0-1 V sweep which is shown as the highest curve in Figure 4.3. To program the next state, the region of NDR was accessed by the use of a programming sweep ending at 3.5 V (not shown). Then, this state was read by a 0-1 V sweep shown as the second highest curve in Figure 4.3. The remaining lower states were accessed in the same fashion as the first two, thereby completing the graph. The states indicated by symbols instead of lines correspond to states previously accessed in Figure 4.2.

4.4 Programming and reading with voltage pulses

The application of voltage pulses can also be used to program and read the conductance states of our devices. In Figure 4.4, square voltage pulses of 2.75 s in length are used to switch a regular-structured OLED between a high conductance state (~2.0 × 10^{-6} A) and a low conductance state (~2.0 × 10^{-8} A). The double-layer OLED makes use of a hole-transporting layer of N, N’-diphenyl-N, N’-bis(1-naphthyl phenyl)-1, 1’-biphenyl-4, 4’-diamine (α-NPB), electron-transporting layer tris (8-hydroxyquinoline) Al (Alq_3), and an efficient electron-injecting cathode made from a thin layer of LiF (1 nm) covered by a thick Al cathode. Electroluminescence from the active area of this device was seen when the programming biases of 6 V and 12 V were applied. This shows that the memory phenomenon can coexist with electroluminescence of the device, giving promise for OLED/memory cells in which a conductance state can be programmed into the device and read out optically. One requirement for this device is a turn-on voltage of less than V_{th}. This will allow a state to be read optically without changing the memory state of the device. Unfortunately, most OLEDs exhibit operation voltages of 2 V or more which is right around the V_{th} of most conductance states. More work must be done in this area to assure the viability of OLEDs used in parallel readout.

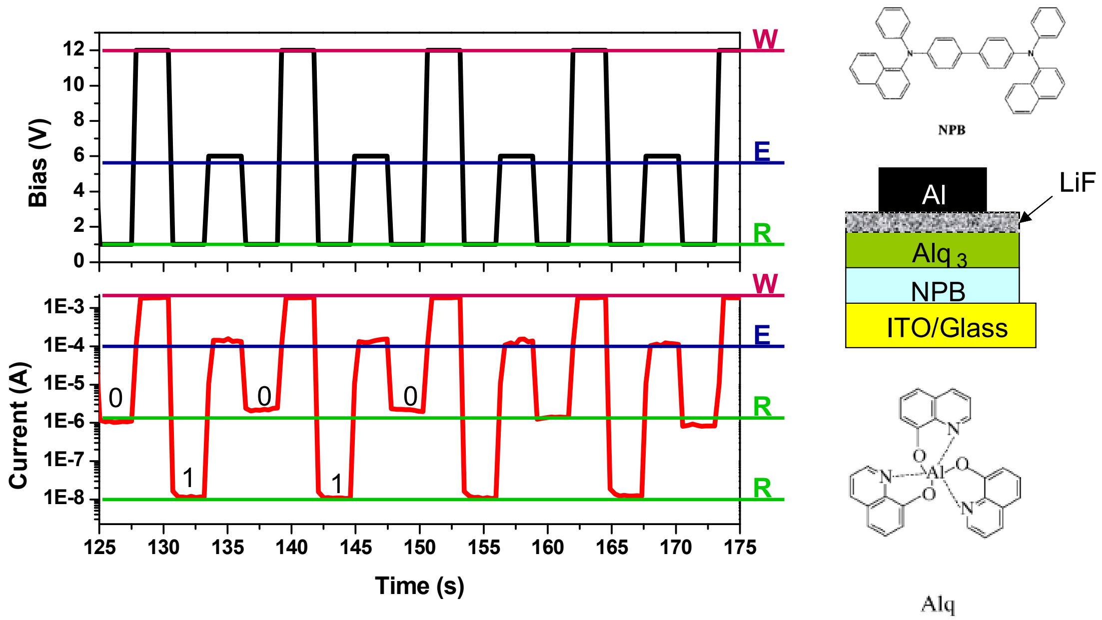

Figure 4.4 Current responses to write-read-rewrite-read voltage cycles. The voltage pulse lengths are about 2.75 s. The device structure is indicated on the right.

4.5 Time response to nanosecond voltage pulses

To further explore the mechanism(s) responsible for the memory effects seen in these thin films, time-response measurements were conducted and switching energy requirements were calculated. Knowing the speed in which two conductance states can be switched between allows the ruling out of some physical processes that take longer than the measured speed. Great care must be taken when measuring the electrical characteristics of these devices. The electrical diagram of the experimental setup is shown in Figure 4.5. The switching times measured for these devices were found to be 50 ns or less when switching from a high conductance state to a low conductance state. Further decreases in pulse size below about 30 ns were limited by the available HP 3314A pulse generator used in our experiments. Switching from a low conductance state to a high conductance state was much less reliable and varied drastically from device to device but in general was on the order of 100's of ns. The nano-second transition time suggests that the switching mechanism is due to electronic processes rather than chemical reactions, conformational changes,[96] or isomerizations,[105] as reported for other organic memory devices.

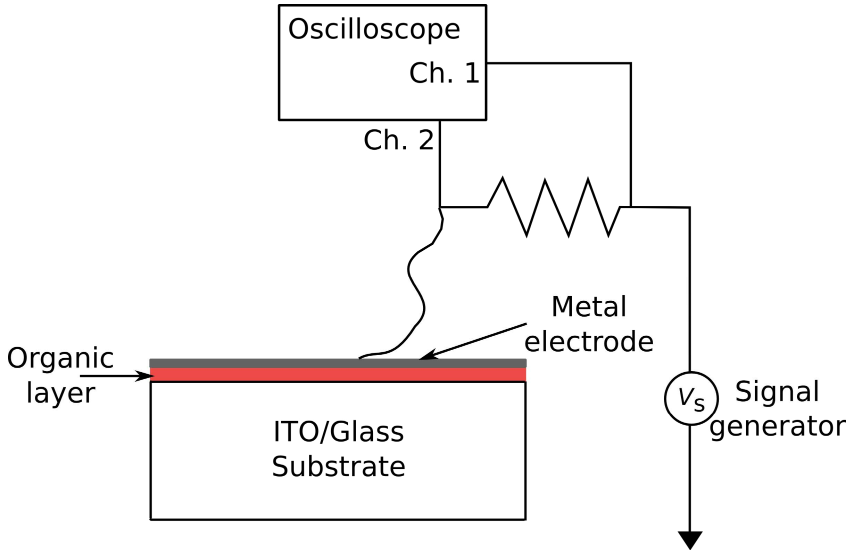

Figure 4.5 Electrical diagram for the nano-second switching experiment.

The amount of energy needed to program or read a given conductance state was calculated by multiplying the duration of the pulse times the bias times the corresponding current.

$$\text{Electrical Energy (J)} = \text{Duration of Pulse} \times \text{Voltage} \times \text{Current} \qquad (2)$$

The energy needed to program or write to the device was calculated to be about 100 pJ. To read the state of the device, it is estimated that an energy requirement of less than 0.1 pJ is needed ($V = .01$ V, $I = 1 \times 10^{-9}$, and pulse duration = 50 ns). This energy requirement is less than most solid-state memory cards available today.

The graph in Figure 4.6 shows two distinct conductance states. The device was first programmed into the high conductance state (not shown). The state was read using a voltage sweep from 0 to 1 V, indicated by the solid line. Then, a nearly square voltage pulse of 12 V in magnitude and 50 ns in length was sent across the device. The device was then read with another I-V scan from 0 to 1 V depicted as a dotted line in Figure 4.6. It shows that the device was successfully switched to a lower conducting state about 3 orders of magnitude lower than its previous state. Then, using a pulse of 100 ns in length and 6 V in magnitude the device was switched back to its original state (indicated by the dashed curve). An attempt to acquire the current data as the bias was sent across the device was unsuccessful due to the limitations of our experimental setup. The Tektronix 500 MHz oscilloscope (model number TDS 3054B, I M-ohm, 13 pF input impedance) would not allow a large enough voltage drop across the device and the in-series resistor to read any significant current due to the oscilloscopes 1 MΩ internal resistor. This could be fixed by increasing the resistance of the in-series resistor, but by doing this a higher voltage pulse was needed to switch the state of the device. The pulse generator in our experiments was unable to produce such a magnitude needed.

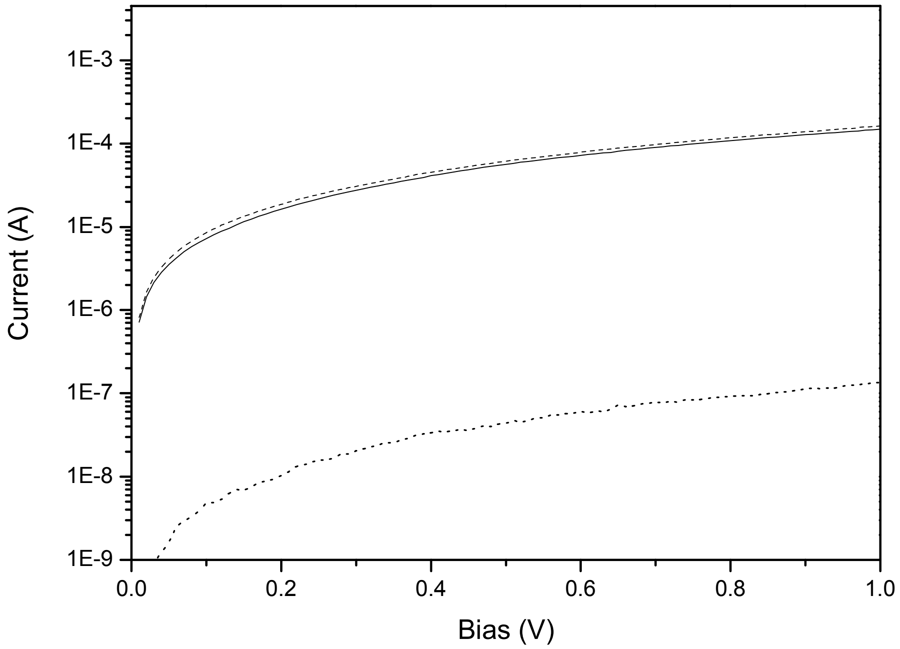

Figure 4.6 High and low conductance states of an ITO/PVK/Al device switched with nanosecond voltage pulses.

CHAPTER 5

RELIABILITY OF SWITCHING AND RETENTION OF STATES

5.1 Reproducible switching cycles

The reliable and reproducible switching between storing a 0 and 1 in a given memory cell is crucial to all rewritable memory technology. In this case, the programming of the device requires a voltage pulse instead of an I-V curve ending at a given programming bias. An example of the switching cycles performed on an ITO/NPB/Alq/LiF/Mg:Ag device is shown in Figure 5.1. The NPB and Alq layers in this device were each 60 nm in thickness. Only a portion of 20,000 successful write-read-erase-read cycles are depicted. A successful switching cycle is indicated by the absence of overlap between the high and low conductance states. The upper section of the graph indicates the input bias pulses. The sequence starts with an erase pulse of 6 V; this programs the device into a high conductance state which can be read out with a following read pulse of 1 V. The 1 V read pulse induces a current of about 1×10^{-6} A indicating that a 1 has been stored. Next, a write pulse of 12 V is used to program the device into a low conductance state, which again can be read out with a read pulse of 1 V. A new current value is read that is about two orders of magnitude lower than the previous current (about 1×10^{-8} A).

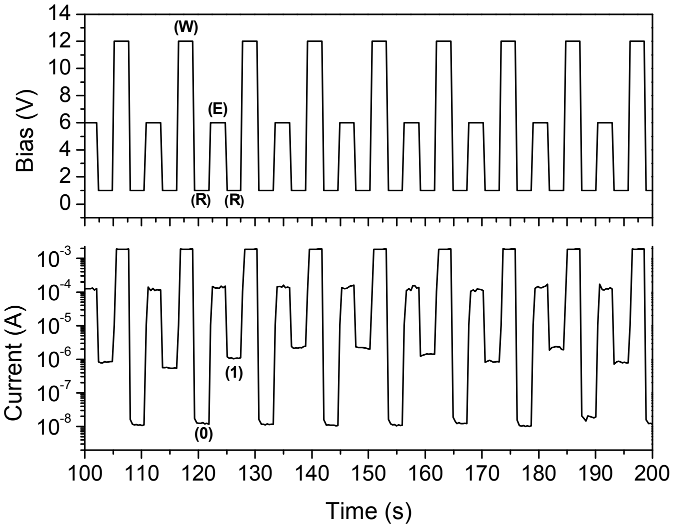

Figure 5.1 Typical current responses to the write-read-rewrite-read voltage cycles with write (W) biases of 12 V, read (R) biases of 1 V, and erase (E) biases of 6 V. The sequence of voltage pulses is shown in the upper depiction while the current response is shown in the lower one. The voltage pulse lengths are about 3 s, and the difference in current between the states is about two orders of magnitude.

Further testing of the reliability of switching between two states was conducted on a device utilizing the structure of ITO/Alq/Al. The middle Alq layer measured 120 nm in thickness (corresponding to the combined organic thickness of the ITO/NPB/Alq/LiF/Mg:Ag) structure. This device exceeded the switching ability of the ITO/NPB/Alq/LiF/Mg:Ag device and successfully switched more than 48,000 times. A portion of these cycles is shown in Figure 5.2. It is believed that the device not incorporating an efficient electron-injecting cathode provides a higher electrical field at the Alq/Al interface. This higher field contributes to the switching mechanism thereby increasing the reliability of the device (explained further in Chapter 6). In addition, the area of the ITO/Alq/Al device was nearly 100 times larger than the area of the ITO/NPB/Alq/LiF/Mg:Ag device adding more switching centers to the device's active area.

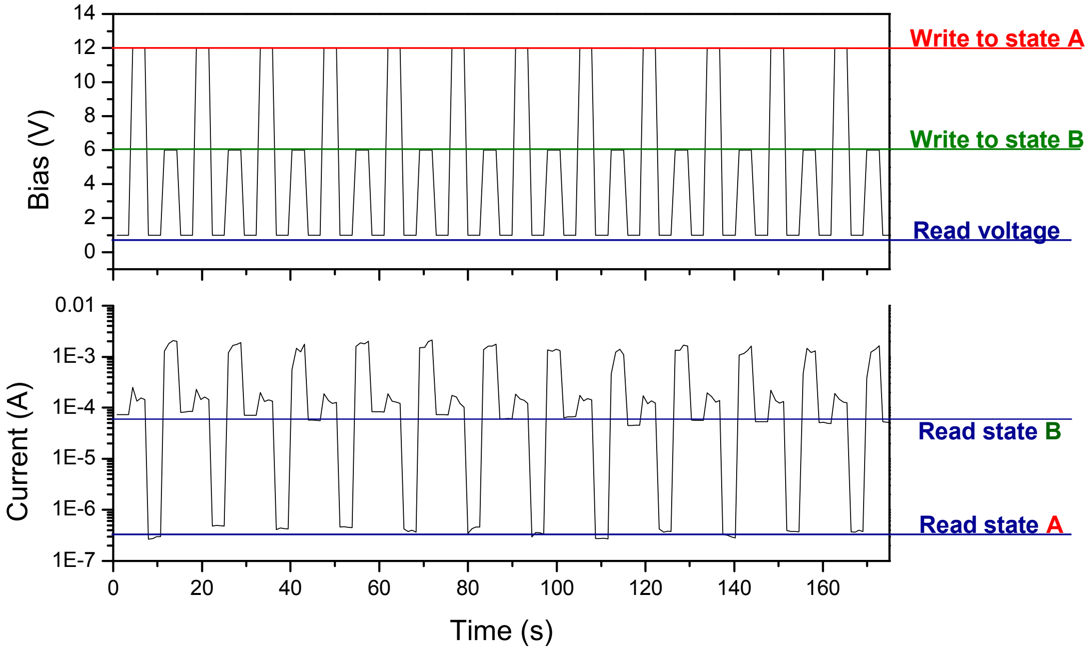

Figure 5.2 A portion of more than 48,000 write-read-rewrite-read voltage cycles using a ITO/Alq/Al device. The voltage pulse lengths are about 3.5 s, and the difference in current between the states is more than two orders of magnitude.

Although some devices switch 10's of thousands of time before failure, many do not make it past 100 cycles. Figure 5.3 depicts the high quality switching of an ITO/PS:C60/Al device. Although initial stages of switching show extremely reproducible behavior with nearly 3 orders of magnitude difference in conductance states, the switching failed at just over 1000 cycles. The cause of failure was due to electrical shorting from electromigration of the electrodes. We believe this is attributed to the middle layer thickness of this device being 42% less than the previous two examples. An investigation of the thickness dependence on device reliability is presented in the last section of this chapter.

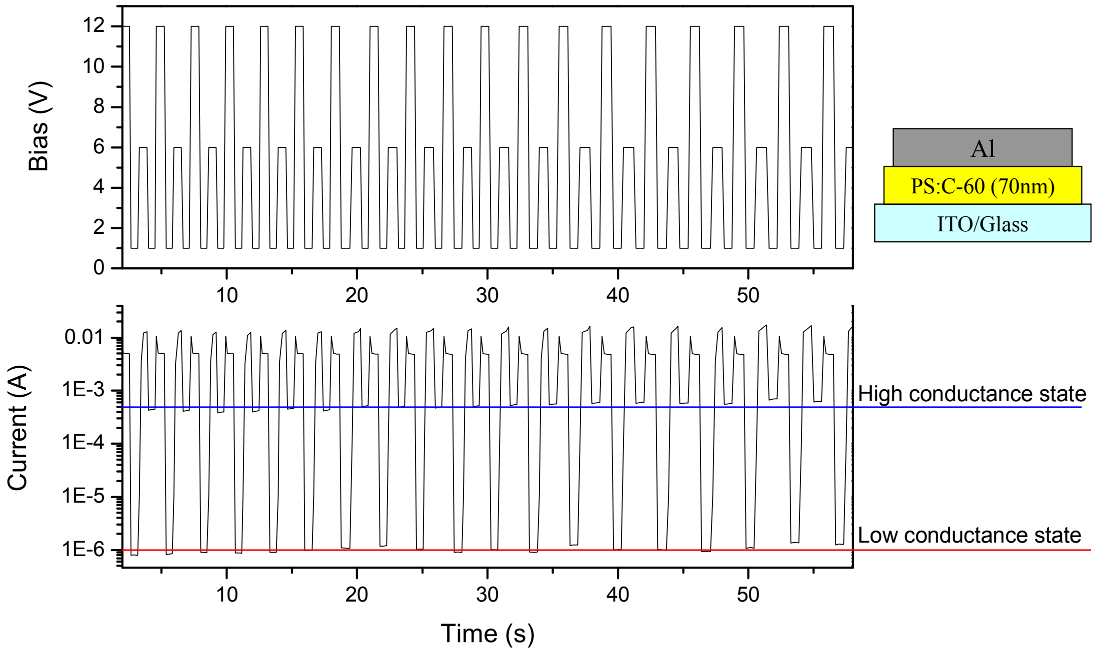

Figure 5.3 A portion of 1000 successful cycles of an ITO/PS:C60/Al device.

Much work is needed to increase the reliability of these devices. Although the conductance states are separated by orders of magnitude in current, there is a significant deviation from one current read to the next for a given state as cycles are performed. The source of failure in these devices usually arises from device electrical shorting or the gradual decrease in the difference of current values between states. A measure of bit error rate was attempted but seemed to be non-applicable due to the wide variation in device performance. Only a slight material dependence on switching reliability was seen. Devices with good electron-transporting abilities usually showed less reliability than others.

5.2 Examples of the nonvolatile nature of the memory effect

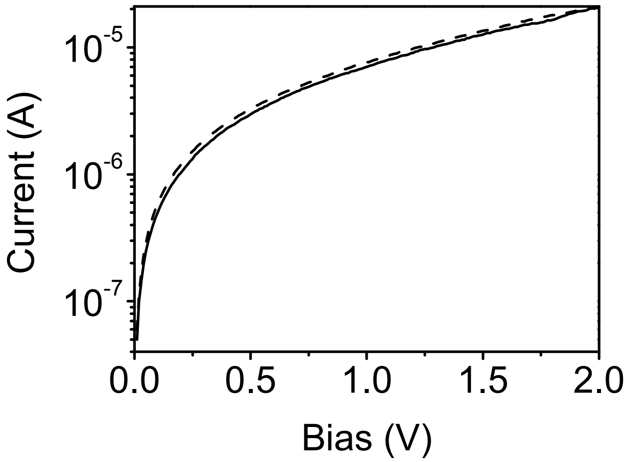

Figure 5.4 Example of the nonvolatile nature of a given conductance state in an ITO/NPB/Alq/LiF/Mg:Ag structured device. An initial I-V curve is shown as a solid line, and an I-V curve after seven weeks is shown with a dashed line.

These devices are non-volatile, readily retaining a given conductance state for at least several weeks without any applied bias as shown in Figure 5.4. This is only in the case of devices stored in a nitrogen (or other inert gas) environment. Devices set in air normally show much less stability. Once the device is in a given memory state, it can be reliably read many times without degradation as shown in Figure 5.5. Here, each state is first programmed by applying a write voltage above V_{th}. States (1) through (7) have been programmed with voltages of 6, 6.5, 7, 8, 10, 12, and 15 V respectively. Once the state is programmed into the device, the state can be continuously read using a probe bias of 1 V for 18 hours or more. The difference between the highest and lowest conductance states is several orders of magnitude, and there is a continuous range of states possible between these extremes. This allows multiple bits of information to be stored per cell in application. The data provided in Figure 5.5 was taken from an ITO/NPB/Alq/LiF/Mg:Ag structured device and exhibit visual electroluminescence at biases above 6 V.

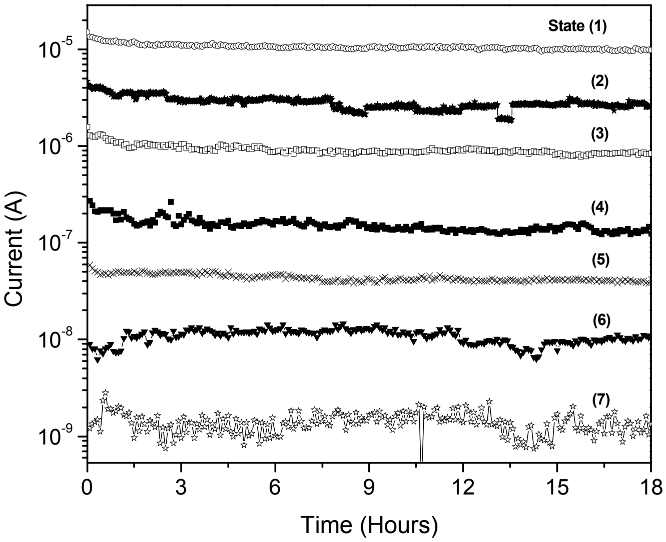

Figure 5.5 Extended time response of different conducting states. States (1) through (7) have been programmed with voltages of 6, 6.5, 7, 8, 10, 12, and 15 V respectively. A probe bias of 1 V is used to show the non-volatile nature of the seven states over an 18-hour period.

5.3 Temperature dependence

The temperature dependence on the retention of states was investigated by the use of a hot plate and liquid nitrogen. First, the device was subjected to an increase in temperature through the use of a hot plate. The devices extended time response of two different conductance states is shown in Figure 5.6. The temperature was gradually increased from 23°C to 150°C for both the low and high state. A probe bias of 1 V shows that both conductance states are stable over this range of temperature.

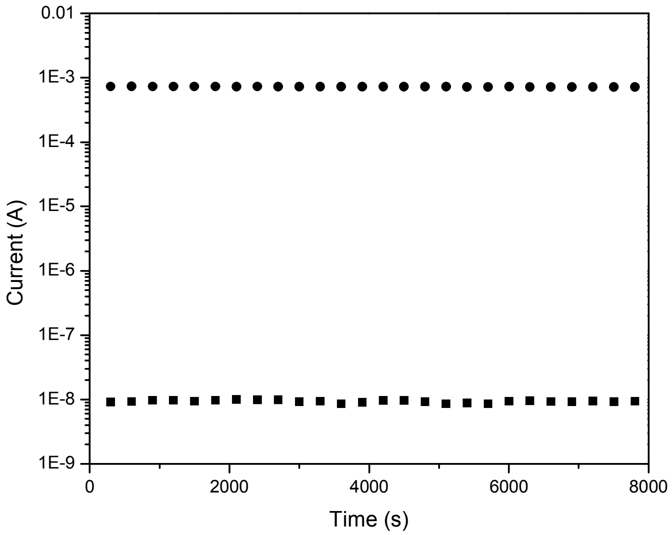

Figure 5.6 Extended time response of two conducting states. A probe bias of 1 V is used to show the non-volatile nature of the two states as the temperature is raised from 23°C to 150°C over a period of about 2 h and 15 min. Data is from an ITO/Alq/Al structured device.

The stability of the two conducting states was also tested while the device was cooled by liquid nitrogen. The 1 V probe bias revealed the same stable results as the heat test. What did change when the devices were cooled to liquid nitrogen temperature was its ability to switch from the low conductance state to the high state. The device could not be switched to the high conductance state until the device was returned to room temperature. This temperature dependence was also observed by Williamson and Collins[106] who cite a filament mechanism responsible for the switching effects seen in their devices.

5.4 Thickness and area dependence

Conductance switching and other memory effects have been shown to exist in our devices which consist of middle layers ranging in thickness from about 50 to 300 nm. In thickness dependence experiments, Alq was used as the organic layer in an ITO/Alq/Mg:Ag device structure. Although switching was seen throughout the range of thicknesses indicated, devices with middle layers near 100 nm in thickness were the best performing in all aspects (nonvolatile, cycle life, etc). Devices with thicknesses near 50 nm switched well for an initial 10 cycles but soon electrical shorts ended their operation. Devices with thinner organic layers generally showed an upward shift in current values for all possible conductance states and a peak conductance slightly shifted to lower voltages (about 1-2 V for the entire 50-300 nm range). Devices with thicker organic layers generally showed a downward shift in current values for all possible conductance states and peak conductance shifts to higher voltages. When thickness increased beyond 300 nm, devices normally showed no switching effects and remained in a low-conducting state. Again, performance varied from device to device.

The device’s area dependence was also investigated. Devices with areas of 6.5 cm^2 down to 0.0625 mm^2 have shown to successfully switch between conductance states. In general, devices with less area show weaker switching reliability although many small area samples exhibited high performance switching similar to the large area devices. This gives evidence that the mechanism responsible for switching is localized. If the mechanism was located throughout the entire area of the device (bulk phenomenon), a proportional decrease in memory effects should be seen as device area is decreased.

CHAPTER 6

SUPPORTING EVIDENCE FOR A PROPOSED MECHANISM RESPONSIBLE FOR SWITCHING AND MEMORY EFFECTS

The mechanism responsible for the memory effects found in MIM structures is not well understood and has been argued by many researchers. We hypothesize that localized current channels are formed between the cathode and anode called filaments. These are formed due to high fields created by departures from the theoretically planar films used in these devices. Electronic conduction through these structures is possible by activated tunneling between metal particles created in the filament forming process. This chapter presents several experiments that give possible evidence to this proposed mechanism responsible for the memory effects observed in our devices.

6.1 Variation in threshold voltage as a function of turn-off voltage

As stated in Chapter 4, the V_{th} of a device is not a constant value. When a device is in a lower conductance state, it exhibits a higher V_{th}. This interesting result has been overlooked by others who have reported multistability.[1,101] In our devices, the variation in V_{th} as a function of turn-off voltages follows an exponential curve indicated in Figure 6.1. In creating this graph, the device is first programmed into the lowest conductance state by executing an I-V scan that ends in a bias of about 25 V. Next, a second scan is conducted to an ending bias just beyond the V_{th} of lowest conductance state. This second scan provides the ending bias value of the second-to-lowest conductance state and V_{th} of the lowest conductance state. This is repeated for several higher conductance states thereby completing Figure 6.1. The data presented for this experiment is collected from an ITO/Alq/Al structure with a middle layer thickness of 100 nm. I-V scans are terminated in the usual manner; however, the addition of a relay utilizing a 30 Ω resistor is used to discharge any stray circuit capacitance. This is implemented to ensure that no significant bias is left across the device at the end of each I-V scan.

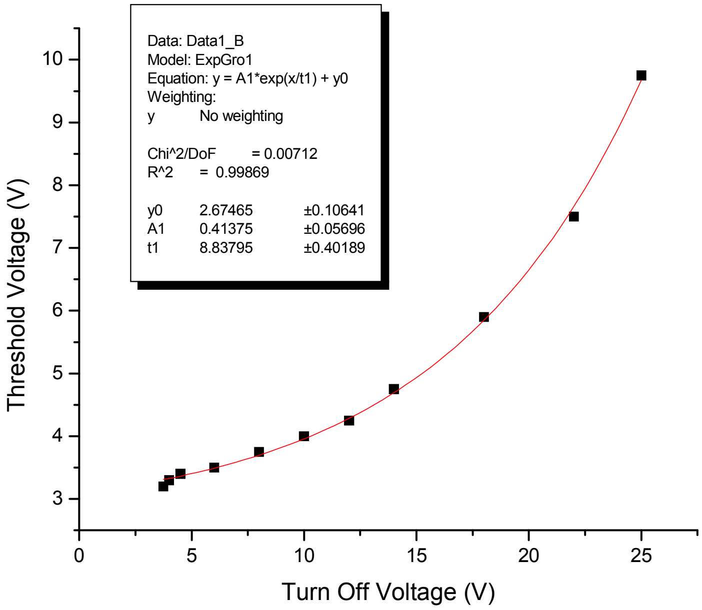

Figure 6.1 Variation in V_{th} as a function of turn-off voltages.

6.2 Shift in peak conductance as a function of turn-off voltage

In our devices, it is found that the peak current of a given state shifts to higher voltages for lower conductance states. Figure 6.2 shows several conductance states and their corresponding peak electrical current. A linear vertical axis is used in this case to more clearly show the current peak of each I-V curve and the region of NDR that follows. In addition, the magnitude of the peak conductance also varies depending on which state the device is in. The several states depicted in Figure 6.2 are located below an I-V locus which has also been cited by the works of Simmons and Verderber.[1] Their data was collected from an inorganic MIM structure incorporating SiO as an insulator sandwiched between Au and Al electrodes (Figure 6.3). There are several similarities between the two graphs, but a locus peak for our data is shifted to near 8 V compared to 4 V for Simmons and Verderber's data. This may be due to a material dependence of either the middle layer or electrodes. It appears as though several processes are competing against each other in this region of instability (region of V_{th} through NDR).

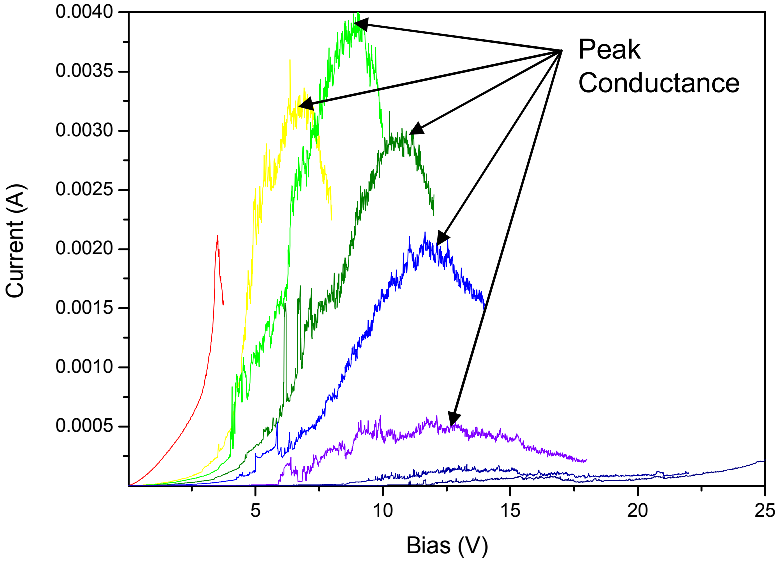

Figure 6.2 Multiple I-V scans indicating the peak current values of several conductance states in an ITO/Alq/Al device.

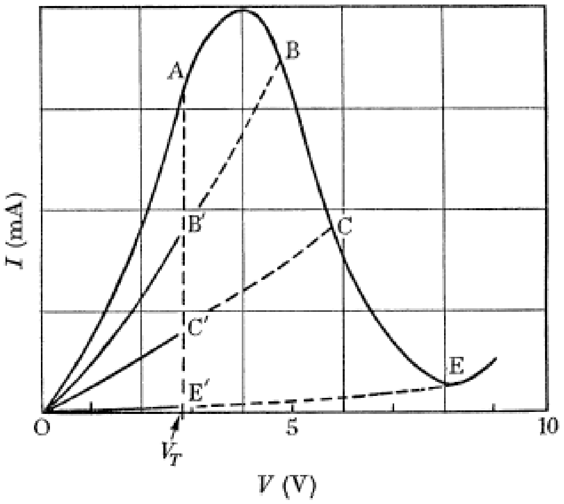

Figure 6.3 Several conductance states found beneath the OABCE locus by Simmons and Verderber.[1] The constant value of the threshold voltage (V_T in this figure) is in disagreement with our data.

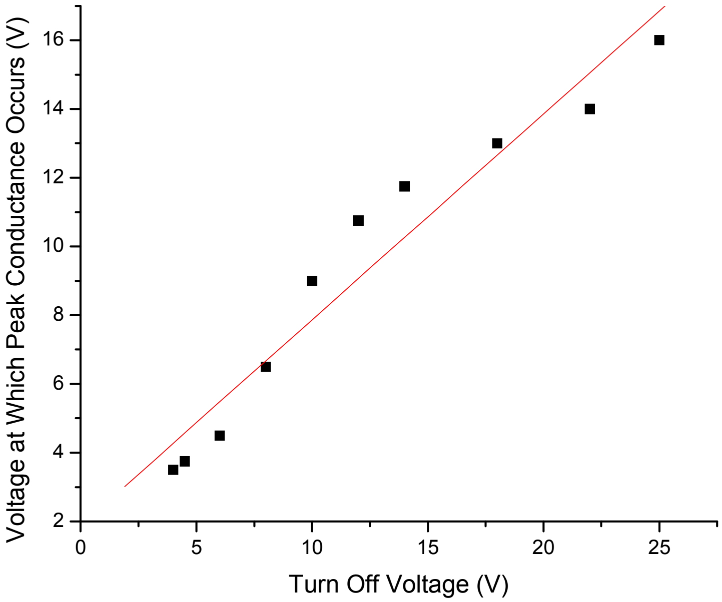

Figure 6.4 Shift in peak conductance as a function of turn-off voltage.

Figure 6.4 shows the shift in peak conductance as a function of turn-off voltage for several states of the ITO/Alq/Al device. The peak current of a conductance state becomes less discernable for lower conductance states (or higher turn-off voltages) but seems to show a linear dependence.

6.3 Effects of oxygen on device performance

As of this point in the dissertation, all experiments have been conducted in a nitrogen-filled glove box with an oxygen and water content of less than 0.5 PPM. For this particular experiment, a separate chamber is used. Flushed with nitrogen and then evacuated to 50 mTorr, a nearly oxygen-free environment is created. The device is placed in the chamber, and a bias is applied above V_{th} but below the voltage that corresponds to a peak current. As the chamber is flushed with air, the current will decrease at roughly an exponential rate depending upon the value of the voltage applied and what conductance state the device is in (the device's current was unaffected by the introduction of air when it was biased below V_{th}). This phenomenon is most easily observed for devices in their high conductance states. In addition, the device's current may increase after an oxygen-free environment is reestablished, but recycling the device to higher voltages is needed to access the previously attained high conductance states. In contrary, when the device is set into a high conductance state and a bias is applied that is above the peak current voltage and in the region of NDR, the device "locks" into a lower conductance state when air is allowed into the chamber. It is extremely difficult to access the original high current values no matter how many voltage recycles are conducted on the device. The hypothesis proposed is that many high-current transporting areas and possibly the locations of the switching centers are accessible through the top electrode. These areas allow oxygen to enter and modify the electrical current of the device.

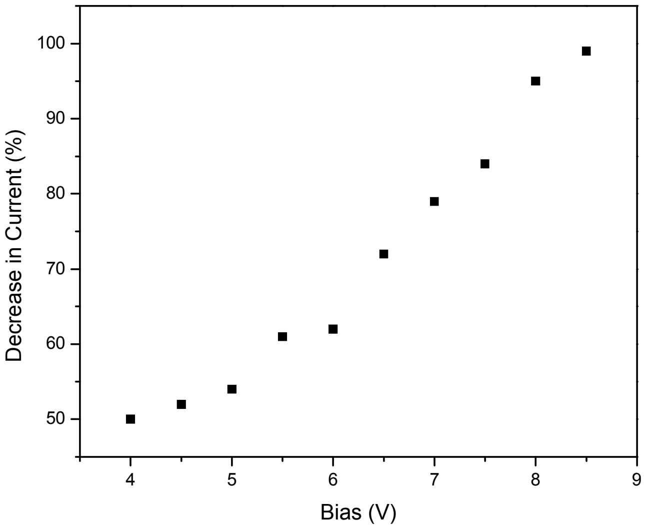

Figure 6.5 Percent decrease in current for a medium conductance state as a function of applied bias when exposed to air.

To test this theory, an experiment involving the additional application of cathode material is conducted while applying a voltage across the device which consists of an ITO/Alq/Mg:Ag structure. The device is first set into a low conductance state by the application of a 12 V bias. Next, this state is read with a 1 V probe bias while the evaporation of Ag is completed at a slow rate. As can be seen in Figure 6.6, the device remains in the low conductance state until a short time after the shutter is opened. At this time, the current drastically increases, clearly showing that metal is being deposited in locations where major current channels reside. The data scan depicted in Figure 6.6 ends at 6 min, and once a new scan was employed, the device’s current was still at a value of about 1.5 mA indicating that a complete short was not the outcome of this test. Although this experiment gives possible evidence of the existence of localized switching centers that are accessible from the top cathode, multitude, size, and the process of formation remain.

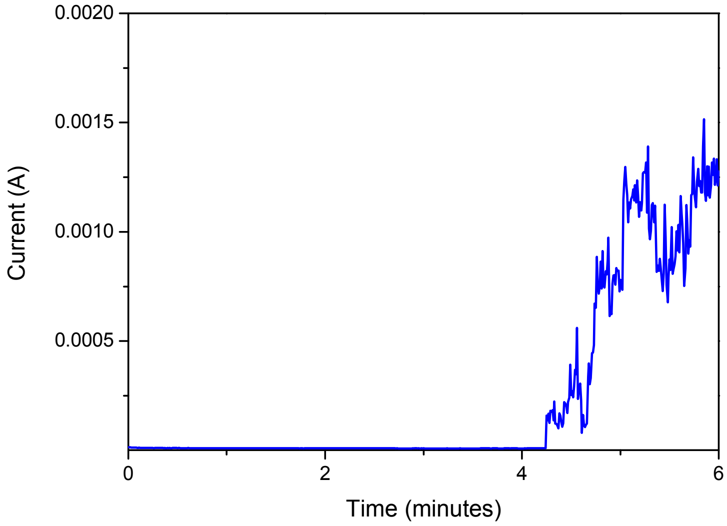

Figure 6.6 Current of a device in a low conductance state while additional cathode material is deposited. The shutter was opened at the 4 min mark.

6.4 Deviations from ideal planar interfaces

In the previous section, it was hypothesized that localized current paths in these thin-film structures could be accessed through the top cathode and are sensitive to oxygen. This section presents a discussion of the possible formation of these localized high-conducting areas by examining the multiple surfaces with several SPM techniques. In addition, the use of PEDOT as an anode-smoothing layer is also implemented to examine its effects on conductance switching.

The organic layer or insulating layer is extremely thin in these devices. The total thickness of the layer is on the order of 100 nm. Homogeneous thicknesses and interfaces cannot be taken for granted in these devices, for the ratio of the lateral dimensions to the thickness of the film is typically about 10,000:l. The roughness of the ITO substrate can vary over the active area of the device. In addition, the cathode, which is normally thermally evaporated, will occupy any irregularities found on the organic films surface. When applying a bias across the two parallel plates, a high electric field will build at any of these protruding irregularities (Figure 6.7).

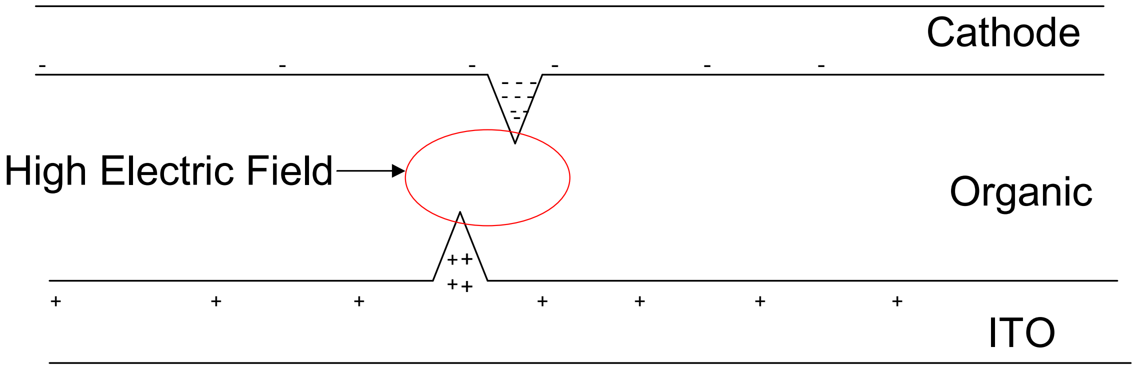

Figure 6.7 Depiction of a high electric field existing at two non-planar areas in a thin-film device.

To investigate the topography of the anode used in our devices, a surface morphology study of our ITO substrates was conducted for a number of samples from several sources (Figures 6.8, 6.9, and 6.10). The surface morphologies of the several types of ITO samples show differences in roughness and general surface structure. There are a wide variety of "roughness" measurements that can be employed. The three most common are the maximum roughness (Rmax), mean roughness (Ra), and root mean square roughness

(Rq). The Rmax is defined as the difference in height between the highest and lowest points on the surface relative to the mean plane (can be helpful for characterizing large peaks and valleys). The Ra represents the arithmetic average of the deviations from the center plane, and the Rq is the standard deviation of the height values within a given area.

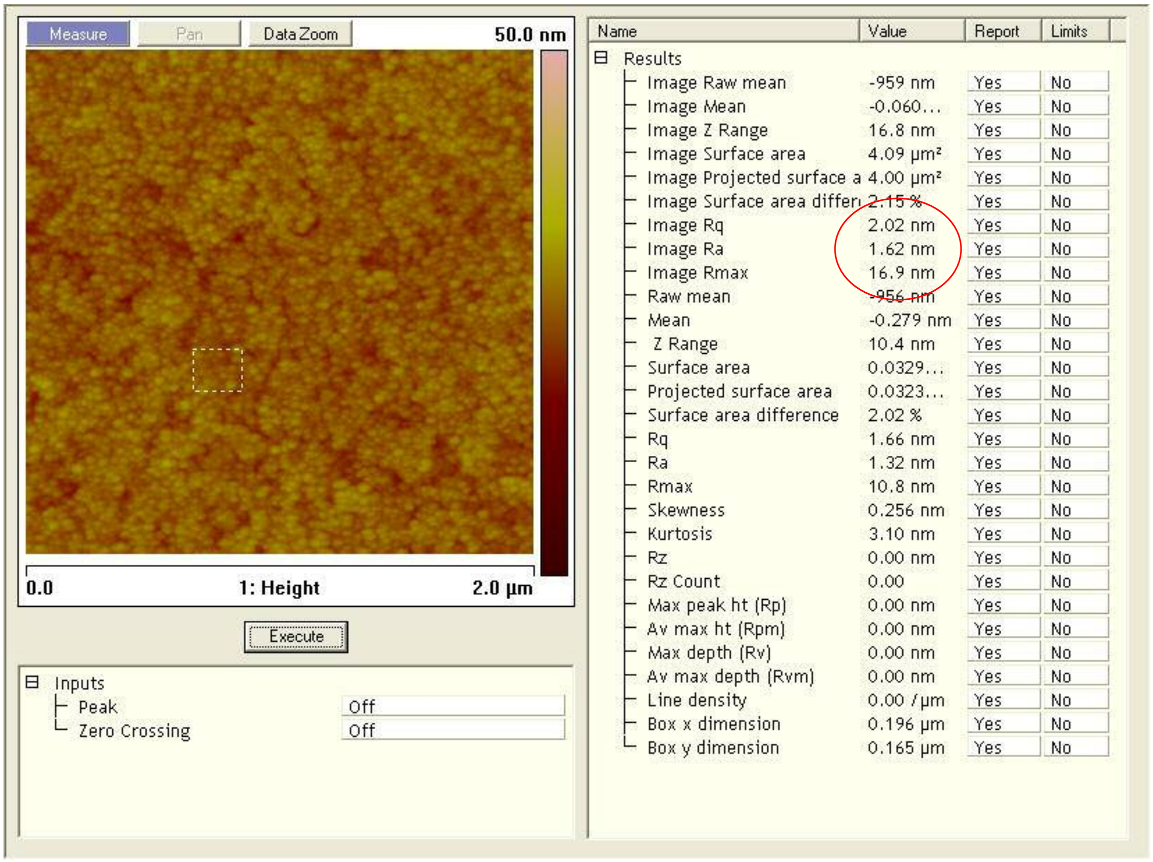

⊟ Inputs
- Peak: Off
- Zero Crossing: Off

Name	Value	Report	Limits
⊟ Results			
Image Raw mean	-959 nm	Yes	No
Image Mean	-0.060...	Yes	No
Image Z Range	16.8 nm	Yes	No
Image Surface area	4.09 µm²	Yes	No
Image Projected surface a	4.00 µm²	Yes	No
Image Surface area differ	2.15 %	Yes	No
Image Rq	2.02 nm	Yes	No
Image Ra	1.62 nm	Yes	No
Image Rmax	16.9 nm	Yes	No
Raw mean	-956 nm	Yes	No
Mean	-0.279 nm	Yes	No
Z Range	10.4 nm	Yes	No
Surface area	0.0329...	Yes	No
Projected surface area	0.0323...	Yes	No
Surface area difference	2.02 %	Yes	No
Rq	1.66 nm	Yes	No
Ra	1.32 nm	Yes	No
Rmax	10.8 nm	Yes	No
Skewness	0.256 nm	Yes	No
Kurtosis	3.10 nm	Yes	No
Rz	0.00 nm	Yes	No
Rz Count	0.00	Yes	No
Max peak ht (Rp)	0.00 nm	Yes	No
Av max ht (Rpm)	0.00 nm	Yes	No
Max depth (Rv)	0.00 nm	Yes	No
Av max depth (Rvm)	0.00 nm	Yes	No
Line density	0.00 /µm	Yes	No
Box x dimension	0.196 µm	Yes	No
Box y dimension	0.165 µm	Yes	No

Figure 6.8 AFM image of the topography of an ITO substrate with corresponding data spreadsheet (ITO purchased from Colorado Concept Coatings LLC).

When comparing Figures 6.8 and 6.9, the Rq and Ra of the two samples are nearly identical (about 2 nm and 1.6 nm respectively) throughout a 2 µm^2 area. In contrast, the

Rmax value, which can help indicate peak or “spike” roughness, is twice as high for the ITO sample depicted in Figure 6.9.

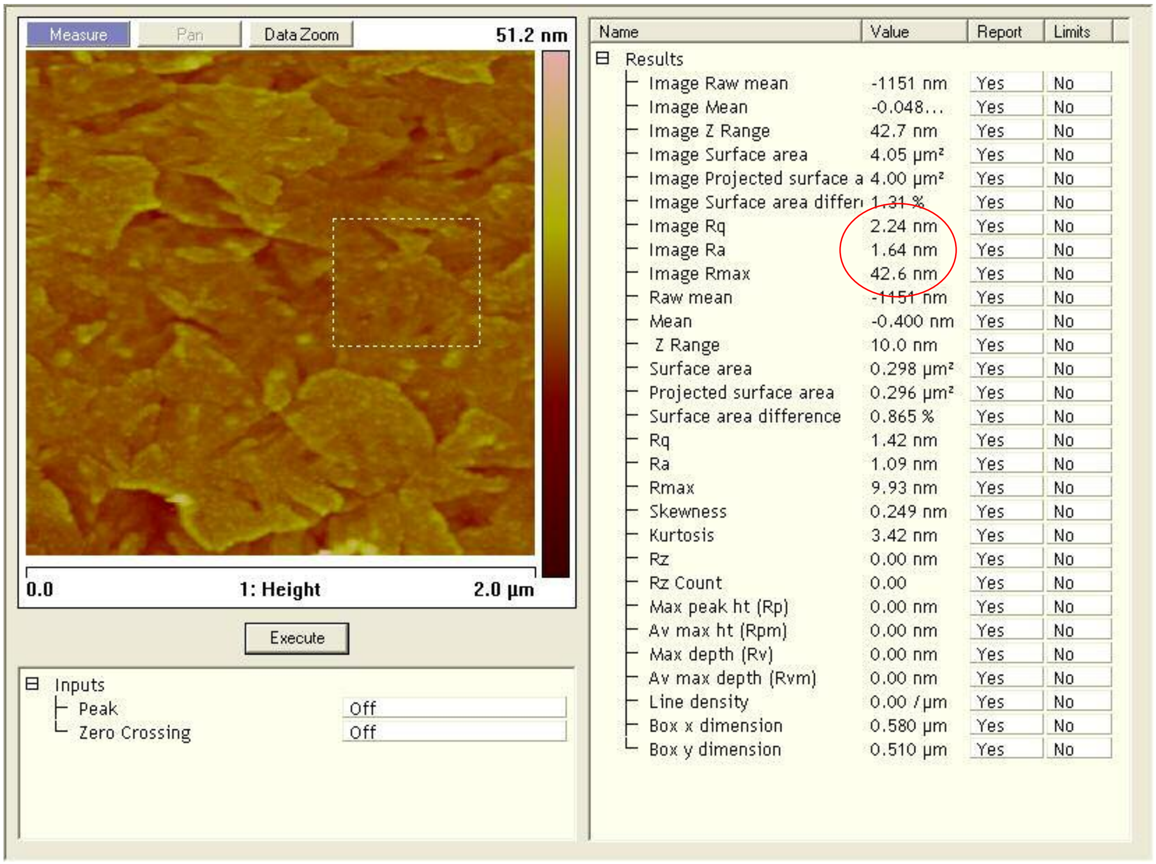

Inputs
- Peak: Off
- Zero Crossing: Off

Name	Value	Report	Limits
Results			
Image Raw mean	-1151 nm	Yes	No
Image Mean	-0.048...	Yes	No
Image Z Range	42.7 nm	Yes	No
Image Surface area	4.05 µm²	Yes	No
Image Projected surface a	4.00 µm²	Yes	No
Image Surface area differ	1.31 %	Yes	No
Image Rq	2.24 nm	Yes	No
Image Ra	1.64 nm	Yes	No
Image Rmax	42.6 nm	Yes	No
Raw mean	-1151 nm	Yes	No
Mean	-0.400 nm	Yes	No
Z Range	10.0 nm	Yes	No
Surface area	0.298 µm²	Yes	No
Projected surface area	0.296 µm²	Yes	No
Surface area difference	0.865 %	Yes	No
Rq	1.42 nm	Yes	No
Ra	1.09 nm	Yes	No
Rmax	9.93 nm	Yes	No
Skewness	0.249 nm	Yes	No
Kurtosis	3.42 nm	Yes	No
Rz	0.00 nm	Yes	No
Rz Count	0.00	Yes	No
Max peak ht (Rp)	0.00 nm	Yes	No
Av max ht (Rpm)	0.00 nm	Yes	No
Max depth (Rv)	0.00 nm	Yes	No
Av max depth (Rvm)	0.00 nm	Yes	No
Line density	0.00 /µm	Yes	No
Box x dimension	0.580 µm	Yes	No
Box y dimension	0.510 µm	Yes	No

Figure 6.9 AFM image of the topography of an ITO substrate with corresponding data spreadsheet (ITO acquired from DARPA).

In some cases, large spikes of nearly 60 nm in height have been observed. This has been reported by several authors.[107,108] It is believed that spikes like these can create localized high electric fields capable of forming high current paths and contributing to the possible breakdown of the organic film and cathode above. Two such spikes can be seen in Figure 6.10. Here, each spike measures about 50 nm in height. The

Ra is small (1.98 nm) when the spikes are not included. A three-dimensional picture of the upper peak can be seen in Figure 6.11.

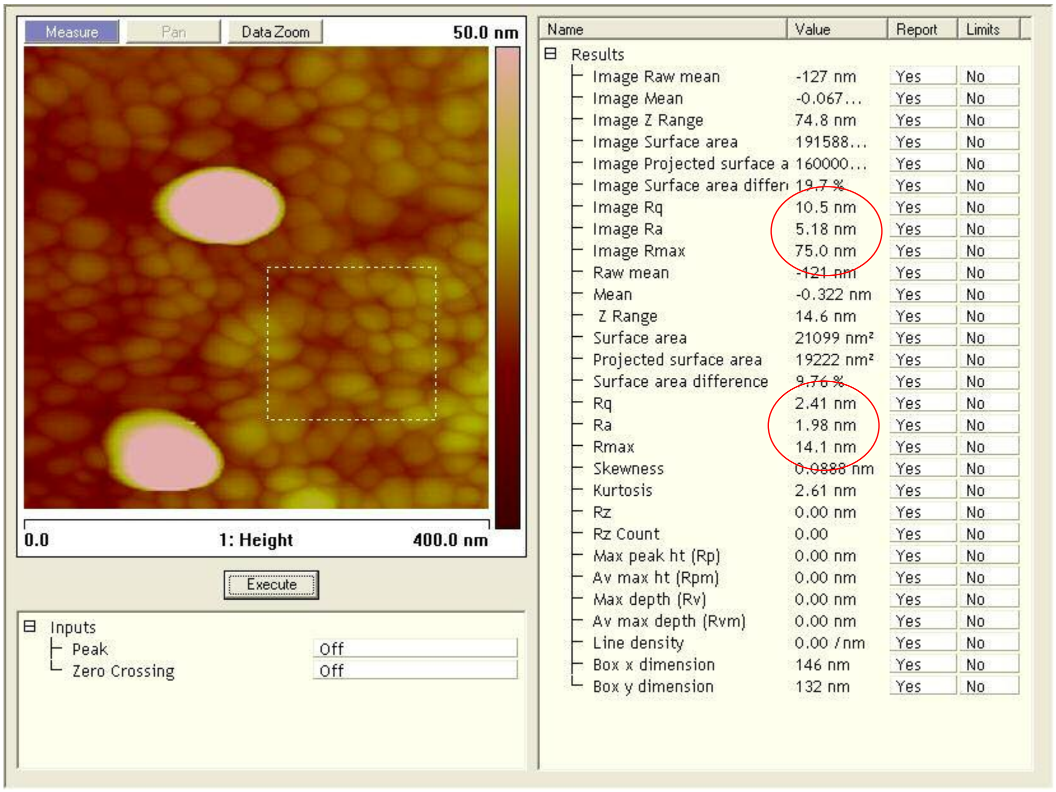

Inputs
- Peak: Off
- Zero Crossing: Off

Name	Value	Report	Limits
Results			
Image Raw mean	-127 nm	Yes	No
Image Mean	-0.067...	Yes	No
Image Z Range	74.8 nm	Yes	No
Image Surface area	191588...	Yes	No
Image Projected surface a	160000...	Yes	No
Image Surface area differ	19.7 %	Yes	No
Image Rq	10.5 nm	Yes	No
Image Ra	5.18 nm	Yes	No
Image Rmax	75.0 nm	Yes	No
Raw mean	-121 nm	Yes	No
Mean	-0.322 nm	Yes	No
Z Range	14.6 nm	Yes	No
Surface area	21099 nm²	Yes	No
Projected surface area	19222 nm²	Yes	No
Surface area difference	9.76 %	Yes	No
Rq	2.41 nm	Yes	No
Ra	1.98 nm	Yes	No
Rmax	14.1 nm	Yes	No
Skewness	0.0888 nm	Yes	No
Kurtosis	2.61 nm	Yes	No
Rz	0.00 nm	Yes	No
Rz Count	0.00	Yes	No
Max peak ht (Rp)	0.00 nm	Yes	No
Av max ht (Rpm)	0.00 nm	Yes	No
Max depth (Rv)	0.00 nm	Yes	No
Av max depth (Rvm)	0.00 nm	Yes	No
Line density	0.00 /nm	Yes	No
Box x dimension	146 nm	Yes	No
Box y dimension	132 nm	Yes	No

Figure 6.10 AFM image containing two peaks found on the surface of an ITO substrate. Roughness measurements taken from the box are indicated by the lower red circle.

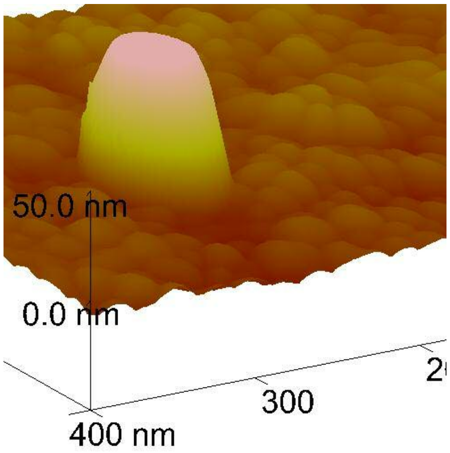

Figure 6.11 3D AFM image of an ITO spike and surrounding area.

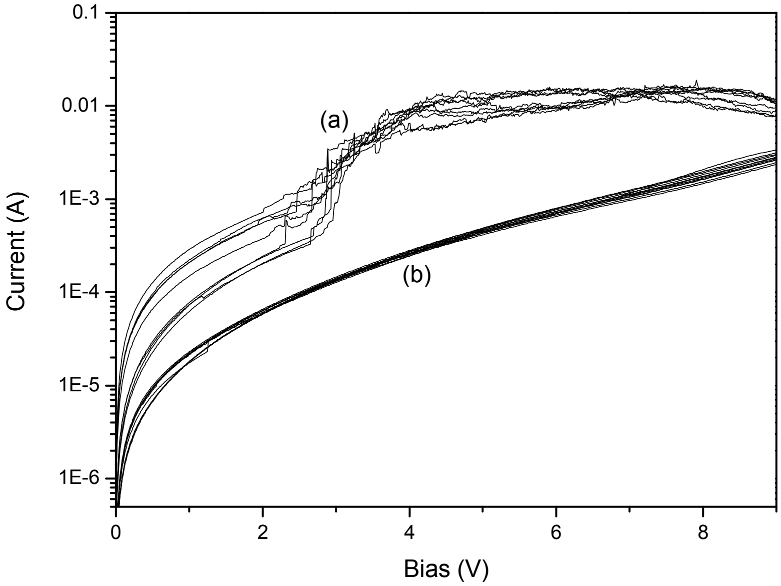

Figure 6.12 Comparison of I-V characteristics of several ITO/Alq/Al devices (a) and several ITO/PEDOT/Alq/Al devices (b) when scanning to a 9 V termination bias.

To investigate the effects of the ITO peaks (or their absence) on the conductance switching exhibited in our devices, a PEDOT layer is used to cover or smooth the relatively rough anode surface. Electronic grade BAYTRON VP CH 8000 PEDOT spin coated at 1500 RPM is used to create a 200 nm thick smoothing layer for several devices. These devices were compared to bare anode devices utilizing an ITO/Alq/Mg:Ag structure. Figure 6.12 shows the I-V scan results of devices without the PEDOT layer exhibiting the normal memory effects as seen in previously characterized devices. The several devices tested without PEDOT all show normal memory effects such as a region of low voltage stability, $V_{th,}$ peak conductance, and a region of NDR. Devices utilizing a layer of PEDOT show no memory effects and smooth I-V curves when biased up to 9 V. The absence of memory effects at low voltages is believed to be due to the PEDOT layer's ability to planarize the ITO anode and nullify the once prominent localized high electric fields produced by spikes found on the ITO surface. This is only the case for small biases. When the I-V scan is allowed to progress to larger ending voltages, memory effects are once again visible but now in a less pronounced way. We believe this is due to the relatively high electric field still occurring around the highly conductive ITO spikes buried beneath the PEDOT film.

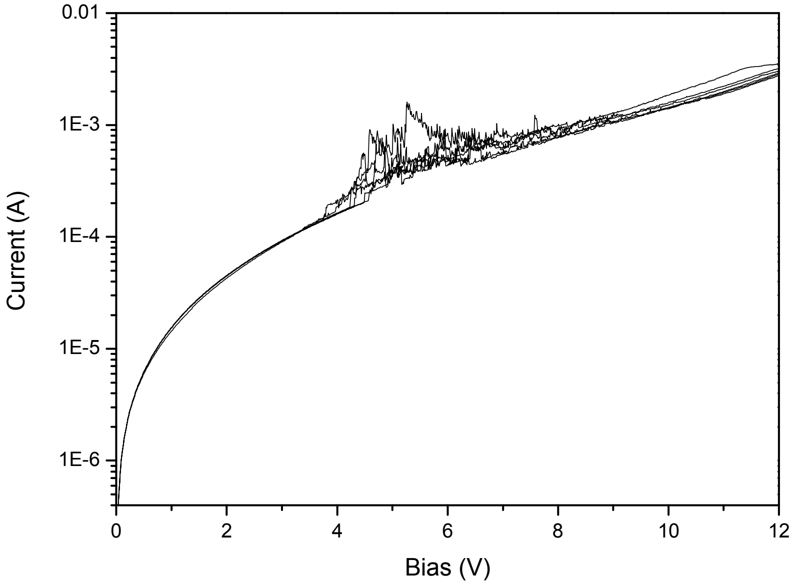

Figure 6.13 I-V scans of several ITO/PEDOT/Alq/Al devices after being subjected to a 12 V bias.

Although these experiments do not provide direct evidence of high current channels or “filaments”, they do provide evidence that the roughness of the anode affects the device’s ability to show conductance switching. In addition, this study cannot conclude that the ITO anode is the only source of irregularities found in these thin-film devices. The organic layer, thermally-evaporated cathode, and any particle contamination could also contribute to localized high electric fields and the formation of high-conducting channels.

6.5 SPM characterization of filaments

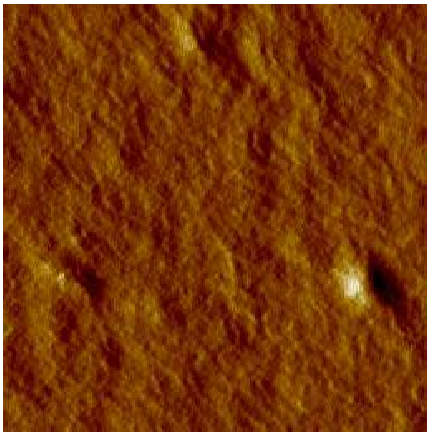

Figure 6.14 AFM image of surface morphology on bare PVK film.

An attempt to gain direct evidence of high-conducting channels or “filaments” is made by creating a device with a special structure and probing it with TUNA and CAFM. An ITO anode is covered with a 60 nm thick layer of the polymer PVK. Next, the thermal evaporation of an Ag metal island layer is completed on top of the organic film. Great care is taken in the deposition of the Ag metal layer so discontinuous regions of metal are separated by only a few nanometers. An AFM image of the PVK surface before and after the application of the thin metal island layer can be seen in Figures 6.14 and 6.15 respectively.

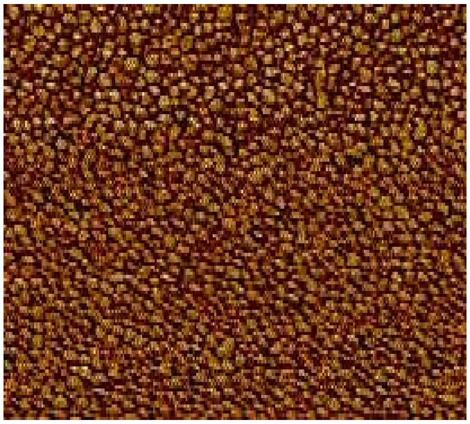

Figure 6.15 AFM image of Ag metal islands on a PVK film.

While in a nitrogen atmosphere, the device is programmed into a high conductance state. Next, TUNA is used to probe an area of the device with a 1 V bias scan (Figure 6.16). Several high-conducting areas can be seen in this scan which exhibit current readings from 1 to 50 pA. Then, without movement of the sample, a low conducting state is programmed into the device using a bias of 12 V from a separate macro-scale contact which is previously connected. A second TUNA scan is then conducted showing the absence of many of the high-conducting areas seen in the first scan (Figure 6.17). Several high-conducting areas still remain, making the number of filaments responsible for conductance switching difficult to estimate. An attempt to switch the device back to the high conductance state was unsuccessfully made which is believed to be due to the device's contact with an oxygen environment.

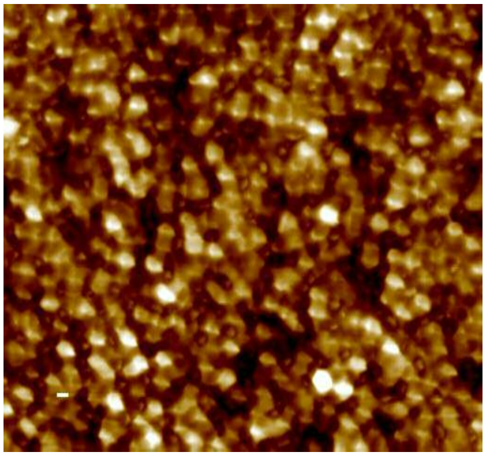

Figure 6.16 TUNA image device in a high conductance state.

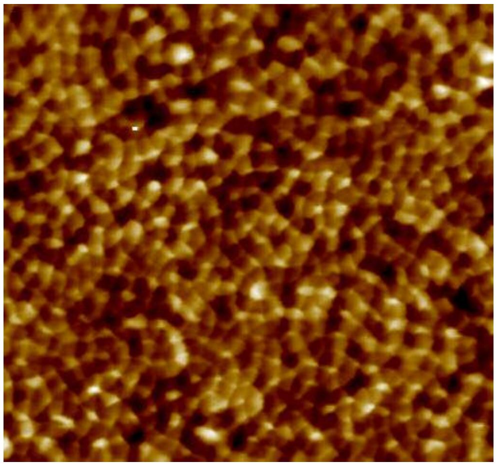

Figure 6.17 TUNA image of device in a low conductance state.

6.6 Filament theory

A filament theory is introduced as the mechanism believed to be responsible for the conductance switching and other memory effects found in our devices. Due to high local fields introduced by irregularities in one or several of the thin films comprising the

ITO/organic/metal devices, high current channels or *filaments* are believed to develop in great numbers. The high local fields are proposed to occasionally damage areas of the cathode[109] creating pinholes and facilitating metal migration from both the anode[107,110-113] and cathode into the organic layer which then forms the filament structure. The damaged areas of the cathode allow the access of the surrounding gaseous environment to infiltrate the device thereby modifying the filament's current behavior. In addition, the metal particles now positioned through the organic layer serve as sites for electronic conduction by activated tunneling.[114] The tunneling barriers' heights are determined by the amount of trapped charges in-between the conducting metal particles. Oxygen molecules are believed to play a significant role in the trapping of the electrons responsible for the barriers between the metal particles.[115,116] In addition, a portion of the electrons traveling through the filament structure can be scattered into the organic material thereby increasing the tunneling barrier between the metal particles. An illustration of the proposed physical process is shown in Figure 6.18.

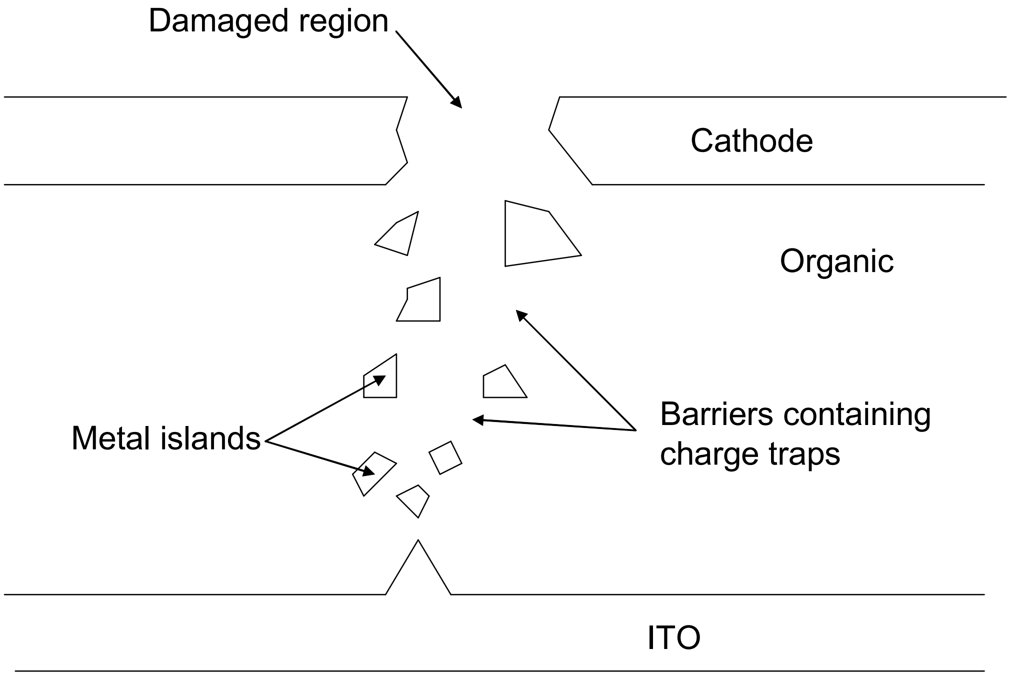

Figure 6.18 Physical features of a typical filament.

A series of metal particles and corresponding barriers are shown in Figure 6.18. Each barrier is believed to employ several traps of different energies that can capture electrons which increase the barrier height and reduce the tunneling current. When the devices are exposed to air and high biases, they tend to lock into lower states (described in section 6.3). We believe this is due to the ample supply of oxygen in air which provides a significant source of traps.[115,116]

When induced by an electrical bias, electrons provided by the cathode will hop between traps and the metal particles until they finally reach the anode. When the device is biased at higher voltages (corresponding to the region of NDR), electrons can be scattered into oxygen molecule traps and into the surrounding organic layer thereby depositing a negative charge and increasing the tunneling barrier between the metal particles. At higher turn-off biases more tunneling traps will come into play and more electrons will be trapped. Lower currents and a higher V_{th} will be seen in the following scan. Evidence for this process was shown by the dependence of V_{th} and the peak conductance on the turn-off voltage (outlined in sections 6.1 and 6.2). Once the electrons are trapped, they can be induced to escape by thermal activation and the electric field.

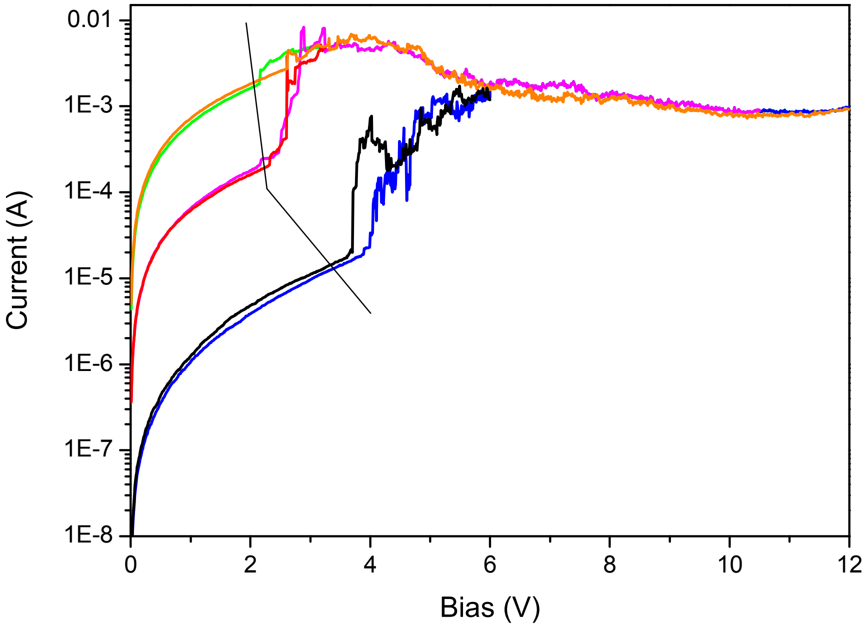

Figure 6.19 Two main regions of I-V characteristics.

The I-V characteristics found in these devices can be divided into three regions (Figure 6.19) and explained in the following way. In the first I-V region, extending from a 0 bias to V_{th}, the current in the copious amount of filaments is governed by activated tunneling, and the device is in its most stable state. The value of current that the state exhibits is dependent upon the history of the device. No hysteresis or conductance switching is exhibited in this region. The tunneling barriers' heights are stable, and electrons are neither trapped nor released in this voltage region. The effects of oxygen are small and much less than what are seen at higher biases.

In the second I-V region ($>V_{th}$), competing processes govern the current characteristics. The conduction mechanisms indicated in the first voltage region are still in effect, but now with the application of higher electric fields, the bias dependent scattering of electrons into traps (decreasing overall current) and the thermally assisted releasing of electrons from traps (increasing overall current) compete to create a region of instability.[117] Captured electrons will be under constant force by the electric field, and with thermal assistance, their subsequent release to a neighboring metal particle will occur thereby opening the trap to another electron. This hopping will occur until the anode is reached, or the bias is removed. If the bias is removed, electrons in traps will remain resulting in the storing of a conductance state in the device. To attain a higher conductance state, the filaments need to release electrons trapped in the tunneling barrier. This can be accomplished by introducing the critical V_{th} bias. The exact detail in the trap and release mechanisms involved in the barriers between the metal particles are not provided due to the complexity of the filamentary system. More work is needed to be done to understand these processes completely.

As higher biases are applied to the device the electron's energy increases. The accessing of deeper traps and the increase in the probability of trapping leads to an overall decrease in current or a region of NDR.

6.7 Chapter summary and conclusions

The nonvolatile multilevel conductance states and other memory effects found in ITO/organic/metal devices have been shown. Several experiments have provided evidence into filament formation and the electrical processes that result. We believe that thermally activated electron tunneling between metal particles entrapped in the organic layer and energy dependent trapping and freeing of electrons in tunneling barriers are responsible for the current characteristics seen in these devices. We believe oxygen has a prominent effect on the amount and size of the traps available. An in-depth understanding of this mechanism is still needed. Once the mechanism behind the switching effect and existence of multiple conductance states is well understood, steps of optimization and advancement of fabrication can take place to push these devices towards a high-density, low-cost, and reliable data storage application.

CHAPTER 7

INTRODUCTION TO WOLEDs

7.1 Motivation of this study

Since the pioneering work of Tang and Vanslyke,[118] the materials and device structures for OLEDs have developed rapidly. An extensive amount of work has been done to improve efficiencies, lower operating voltages, extend lifetimes, and tune color emissions of these increasingly viable devices. WOLEDs implementing multifunctional macromolecules represent a unique route to producing low-cost and highly-efficient white-light illumination. Macromolecules can be easily purified, which is critical to the lifetime and quantum efficiencies of OLEDs. They are highly soluble, making them prime candidates for simple, high-volume, large-area manufacturing.[98] The ability to functionalize macromolecules with several moieties (emitter, charge transport, etc.) allows possibilities of an all-in-one material. Although these new materials are still in their infancies, there has been much progress in their performance. The development of new functionalized cores will enable WOLEDs to attain higher quantum efficiencies, simplified device architecture, superior white color purity, and longer device lifetimes. This work shows further strides in the improvement of macromolecule-incorporated WOLEDs aiding their advancement to future application.

7.2 Applications for WOLEDs

Organic electroluminescent devices capable of emitting white light are desirable because of their potential utility as backplane lights for LCDs, overhead lighting, and other lightweight, low profile, low power lighting applications. Their high efficiencies, minimal operating voltages, and supreme color gamut make them prime candidates for the next generation of white-light illumination. WOLEDs inherent lightweight, mechanical flexibility, and extremely thin profile will allow for a high degree of integration with the next generation of electronics and new fashion trends in home lighting.

7.2.1 Solid-state lighting

With world energy consumption at an all-time high, there has been increasing interest and excitement to create new solid-state lighting technologies that are cheaper to manufacture and more efficient to use than the present lighting methods. General lighting accounts for about 20% of all the electricity produced in the world.[119] In the United States alone, about 765 TWh/yr of electricity is used for lighting which costs consumers nearly $60 billion annually. Inefficient incandescent bulbs and high-costing fluorescent tubes are the most common lighting technologies used today. Filament bulbs account for 63% of all light sources used in the United States.[120] Developed more than 100 years ago, they convert only about 10% of electrical energy to light and the rest is lost to heat. Typical efficiencies range from 12-20 lm/W for these simple low-cost (less then $.01 to produce) light sources. Although not efficient light sources, the incandescent bulb produces light with similar color temperature and color rendering index as the sun. This makes incandescent bulbs more pleasing to the average person. Fluorescent lamps are more efficient than incandescent bulbs. Their efficiencies can reach more than 90 lm/W. However, they can be dangerous to the environment due to their mercury content. Moreover, the CRI of fluorescent lights is usually between 70 and 90. Consequently, a high-efficient lower-cost alternative to these mature technologies that is solid-state in nature and environmentally safe in composition is desired.

The potential to fulfill these general illumination needs has brought OLEDs a tremendous amount of attention. With low driving voltages of about 5 V, high-power efficiencies of 30-60 lm/W (as demonstrated in laboratories), and internal quantum efficiencies of nearly 100%, these solid-state devices show much promise in the replacement of older technologies in some of the current applications, and the creation of a new paradigm in lighting applications.

7.2.2 Backlighting for liquid crystal displays (LCDs)

Displays for office automation and image-processing equipment come in a variety of forms, including cathode ray tubes (CRTs), plasma displays, LCDs, and others. Of these, LCDs have gained the widest acceptance because they are thin, lightweight, require less power, and can reproduce colors better than many other types of displays. A diagram of the many LCD components is depicted in Figure 7.1. In today's information-intensive society, these superior characteristics have led to LCDs being used in a variety of imaging and information-related equipment in offices, homes and vehicles, as well as outdoors. Direct-type panels best manifest the LCD qualities of being thin, lightweight, and energy efficient. Both black-and-white and color types are used in a variety of equipment such as calculators, game machines, personal digital assistants (PDAs), digital cameras, and compact cellular telephones. Conversely, projection-type LCDs are preferred for some applications because of their size, relative low cost, and high resolution. Both types of panels require quality backlights to guarantee good visibility.

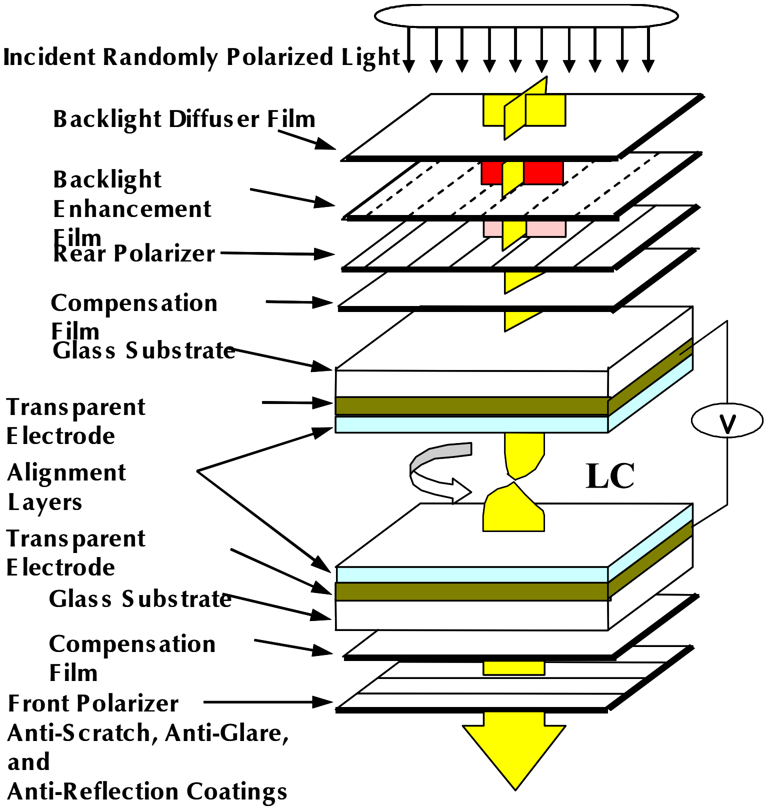

Figure 7.1 Diagram of LCD components (Liao and Tang, China FPD Conf. Oct. 2004).

Light sources that are used as backlights include incandescent bulbs, light-emitting diodes (LED)s, fluorescent lamps, and metal halide lamps. Of these, fluorescent lamps are most commonly used for direct-type panels (although recent advancements have demonstrated the use of LEDs) while metal halide lamps are generally used as backlights for projection-type panels. However, all of these lighting sources cannot be integrated into a flexible display setting. OLEDs can fill this niche application. In addition, they can be used as backlights in PDAs, cell phones, digital electronics, and other mobile lightweight high resolution displays. Furthermore, by using white OLEDs as the light mechanism, one can use only color filters (normally used in an LCD display) to simplify even further the structure and manufacturing of the display. Recently, Samsung demonstrated a 40 in. full color display based on a white OLED emitting layer and the use of red, green, and blue filters (Figure 7.2). In this case the white OLED replaces at least both the backlight and the liquid crystal material.

Figure 7.2 Illustration of a 40-inch prototype AMOLED (from Samsumg.com).

7.3 Theory and device physics of organic light-emitting devices (OLEDs)

Electroluminescence from organic materials was first observed and extensively studied in the 1960's.[121,122] One of the first reports of electroluminescence was made by Helfrich and Schneider using several micron-thick anthracene crystals (Figure 7.3). Due to charge-transport deficiencies, hundreds of volts were required to operate these initial devices equating to quantum efficiencies and lifetimes significantly lower than those obtained for inorganic systems at this same time period. Still, more work followed to decrease the thickness of the anthracene thin films by the use of fabrication techniques such as thermal evaporation. Even with the employment of much thinner films, quantum efficiencies were still limited to less than 0.1% due to unbalanced charge transport and cathode quenching. Then in the 1980's, interest in organic materials was revived due to a team of researchers from Kodak. Led by Tang and VanSlyke, reports were given of the first efficient double-layer OLED (Figure 7.4).[118] This work was followed by further advancement in quantum efficiencies and color gamut by using a doped emitter of highly-fluorescent organic dyes.[123] Low-operating voltages of less than 10 V and higher quantum efficiencies of approximately 1% were reported, thereby igniting an intense investigation by scientist and engineers alike. These new studies were fueled by the apparent potential of the OLED in displays and solid-state lighting.

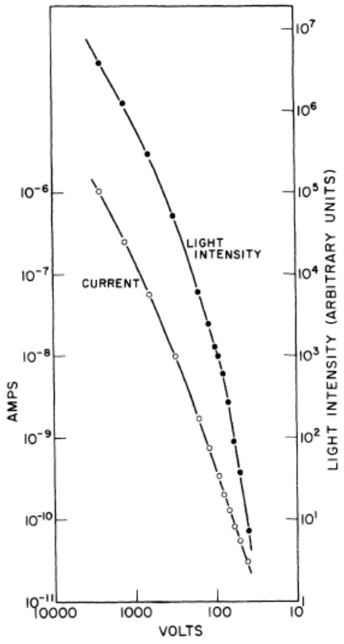

Figure 7.3 Organic electroluminescence characteristics of anthracene crystals reported by Helfrich and Schneider (1965).[122]

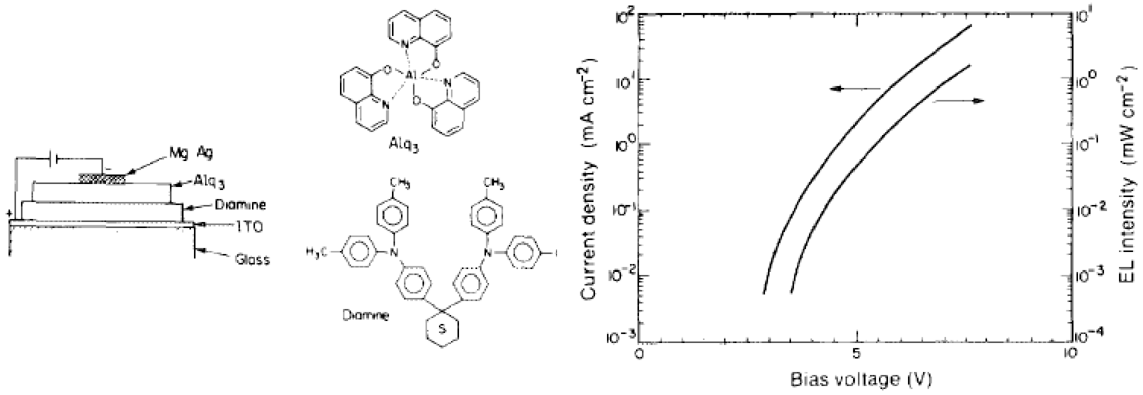

Figure 7.4 Electrical and luminescent data from the first hetro-structured OLED by Tang and VanSlyke (1987).[118]

An OLED consists of one or more thin films (usually <200 nm in combined thickness) of organic material sandwiched between an anode and a cathode. In a two-layer device, one layer is specifically designed to transport holes and the other layer to transport electrons. Ideally, the electron and hole form an exciton at the interfacial region of the two layers and result in electroluminescence. Once photons are created, they must exit the device through either or both electrodes. To do so, one or both of the electrodes must be transparent. An ITO-covered glass substrate is usually used as an anode due to its relatively high work function of 4.5 to 5.0 eV and transparency in the visible spectrum. A low work function metal such as Ca, Mg, Al, or In can be used as cathode materials to facilitate electron injection. The common use of a Mg:Ag alloy at a 10:1 ratio or a heterostructure of LiF(very thin ~1 nm)/Al provide cathodes with low work functions, strong adhesive properties, and good chemical stability.

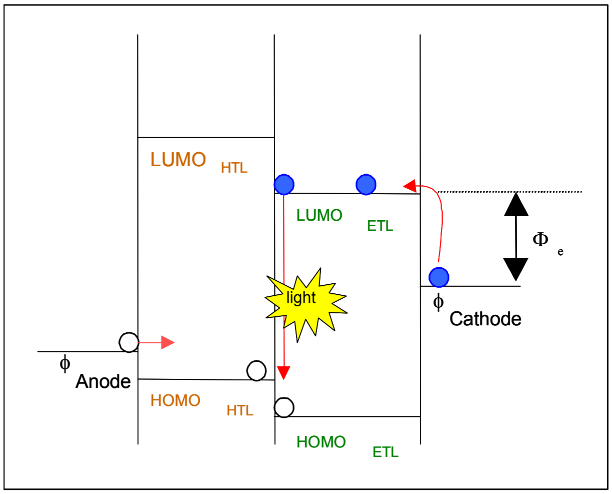

Figure 7.5 Energy level diagram of double-layer OLED.

By applying an external potential difference between the cathode and anode, charge carriers (*i.e.* holes at the anode and electrons at the cathode) are injected into the organic layers (Figure 7.5). Holes are injected into the highest-occupied molecular orbital (HOMO) of the hole-transport layer (HTL), while electrons are injected into the lowest-unoccupied molecular orbital (LUMO) of the electron-transport layer (ETL). In the presence of an electric field the holes and electrons migrate to the opposite electrode. The current travels via thermally-activated charge hopping from one molecular site to another. The hole and electron mobilities in organic materials usually range from 10^{-9} to 10^{-2} cm^2 $(V\ s)^{-1}$.[124] Hole mobility in amorphous organic material is generally orders of magnitude higher than electron mobility due to the intrinsic p-type conductive nature of most organics. The holes and electrons are non-radiatively discharged unless they encounter each other while moving through the organic layers. If they encounter one another, an excited singlet or triplet state might form called an exciton. Light emission based on excited singlet state relaxation to the ground state is known as fluorescence; whereas, an emission from the triplet state is termed as phosphorescence. A more detailed explanation of the electroluminescence process is outside the scope of this dissertation but is provided in Ref [125]. The ratio of the total number of photons produced to the number of electrons injected is termed the internal quantum efficiency η_{int} of an OLED and can be calculated by measuring the external quantum efficiency η_{ext} and the use of equation (3). According to ray trace optics, only about 20% of the light generated inside the OLED exits through the front face of the device. This is only an estimation. Parameters such as the OLED structure, ITO thickness, metal reflectivity, orientation of the emitting dipole, and the organic layers complex index of refraction affect the amount of light that exits the device through the front face.[126-129]

$$\eta_{int} = 2n^2\ \eta_{ext} \qquad (3)$$

A simple two-layer structure can be modified to a three-layer structure where an additional layer is inserted between the HTL and the ETL to serve as a recombination site for the production of electroluminescence and to allow formation of excitons away from the quenching cathodes. With this geometry, each layer can be optimized for its specific function. The electroluminescent layer can utilize a chosen material that will emit a desired color with high-quantum efficiency, while the HTL and ETL layers can be tuned to transport and block certain charge carriers. Further layers can be implemented, fluorescent and/or phosphorescent dopants can be used to increase quantum efficiencies and tune color outputs. Hole and/or electron blocking layers can be added and their thicknesses can be controlled to confine recombination zones for the balancing of color emission and increasing device efficiencies.

Organic materials can be tuned to emit a wide gamut of colors with high luminescent efficiencies. The color of the light generated depends on the energy difference between the molecular excited states and the ground level of the organic material. Although selective emission from the ultra-violet to the infrared is possible for organic materials, to this day there has been no published reports (to the best of our knowledge) on single organic molecule that efficiently emits light broadly enough to cover the entire visible spectrum. Consequently, many device structures and combinations of materials are used when white-light emission is desired. These techniques will be discussed in section 7.5.

7.4 Photometry and white light standards

Photometry is a science that involves the measurement of visible light, which is defined as electromagnetic radiation detectable by human vision. Thus, it is restricted to the wavelengths ranging from about 360-780 nm and weighted according to the spectral response of the eye. The brightness, color quality, and hue of white light illumination that the eye perceives are of crucial importance in the general illumination industry. There are many terms and characterization techniques that are important to understand when grasping the science behind WOLED technology and when developing new device designs. This section will provide an overview of the human eye, several definitions of photometric quantities, and three gauges of white light quality.

7.4.1 Human eye

The human eye is used to perceive the color and intensity of light originating from the surroundings. No human being detects light quantitatively or qualitatively the same. Age, race, sex, and many other factors affect our visual perception of the world around us. Although the detection of light can be explained physically, the perception of color and brightness is a psychological phenomenon. Therefore, the standards for quantifying color, which have been created by organizations such as the Commission Internationale de l'Éclairage (CIE), are average values for a representative group of tested individuals.

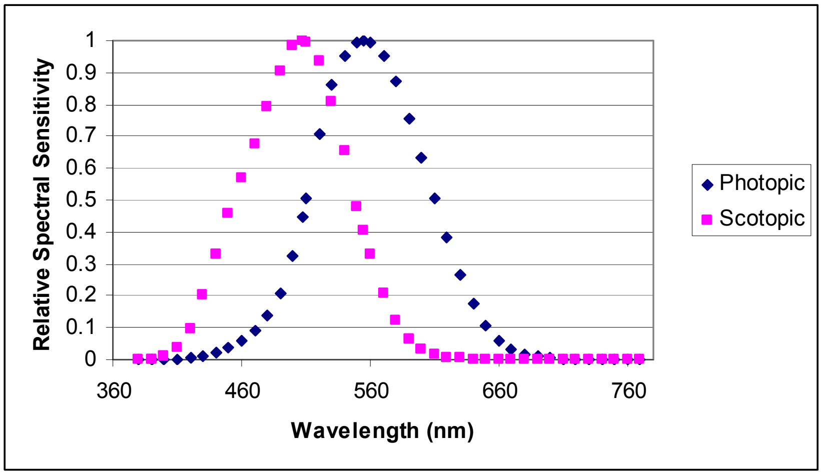

Figure 7.6 Photopic and scotopic response of the human eye.

Once light is collected, the eyes detectors (cones and rods) convert photons to electrons. When the intensity of the light entering the eye is low, the extremely sensitive rods control the responsivity of the eye (scotopic response) which is most sensitive at a 505 nm wavelength peak. When the intensity of the light entering the eye is high, the more color sensitive cones (photopic response) control the responsivity of the eye which is most sensitive at a 555 nm wavelength peak (Figure 7.6). Thus, in day light our vision is photopic, while at night and in the dark it is scotopic.

7.4.2 Photometric definitions

Luminous flux Φ_L (optical power with respect to the response of the human eye) has units of Lumens (lm) and is given by:

$$\Phi_L = A \int \Phi(\lambda)\, V(\lambda)\, d\lambda \qquad (4)$$

where A is the maximum spectral luminous efficacy, 683 lm/W at a wavelength of 555 nm for photopic vision and 1700 lm/W at a wavelength of 505 nm for scotopic vision. $\Phi(\lambda)$ is the radiant power in units of W/nm and $V(\lambda)$ is the photopic or scotopic response curves (Figure 7.6).

Using this newly defined measure of optical power (lumen) several additional terms can be introduced (Table 7.1) Illuminance (lux) is measured in lm/m^2 and takes into account irradiance that is photopically weighted power per unit area incident from all directions onto a surface. Light meters usually measure this quantity. Luminous intensity which is commonly used for approximating small sources and measured in candelas (cd), is spectrally weighted power per unit solid angle. Finally, luminance (cd/m^2) is spectrally weighted power per unit projected area per unit solid angle and is commonly termed brightness. Many argue this equality, due to the concept that brightness is a sensation that depends on the state of the eye; therefore, the term luminance will be used in this dissertation and not brightness.

Table 7.1 Radiometric and photometric units.

Radiometric	Photometric
Watt (W)	Lumen (lm)
Watt/meter^2 (W/m^2)	Lumen/meter^2 = lux
Watt/steradian (W/sr)	Lumen/steradian = candela (cd)
Watt/meter^2 steradian (W/m^2 sr)	Lumen/meter^2 steradian = (cd/m^2)

7.4.3 Gauges of white light quality

There are three gauges of white light quality. The CIE chromaticity coordinate system, CIE color rendering index (CRI), and color-correlated temperature (CCT) values are used in the characterization of white light sources. Depending on the application, the relative importance of a single parameter might significantly outweigh the others. Some applications where illumination sources are viewed directly, such as traffic lights (Figure 7.7 (a)), will require pure white-light emission with CIE chromaticity coordinates of about (0.33, 0.33) but do not require a high CRI value. This can be attained by the mixing of just two complementary colors such as yellow and blue depicted in Figure 7.8. Still other lighting applications such as the illuminations of artwork in a museum (Figure 7.7 (b)) or fresh fruits at a grocery store will require CIE values of (0.33, 0.33) and a high CRI value of nearly 100. In this case, a broad spectrum covering the visible spectrum similar to a black body radiator is needed to accurately reproduce the intended colors being illuminated.

Figure 7.7 Examples of lighting applications for low (a) and high (b) CRI values.

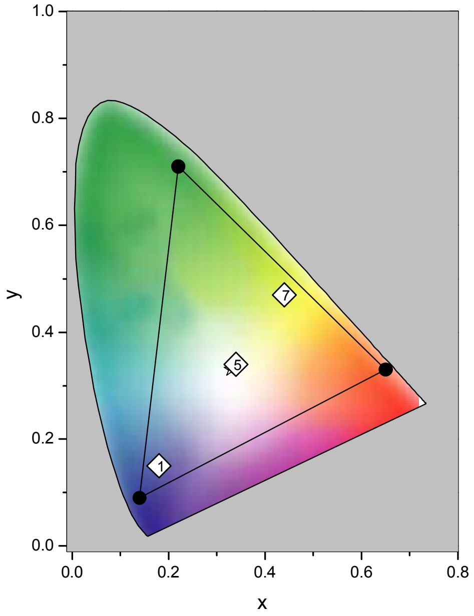

Figure 7.8 Depiction of a bi-color system attaining CIE coordinates of (0.33, 0.33) by balancing blue and yellow emission.

The chromaticity of light emission from an OLED is commonly defined by the CIE chromaticity coordinate system which was developed in 1931.[130-132] Avoiding negative values, the color of the spectral light in question must be reproduced by the mixing of unreal primaries resulting in the tristimulus values *X*, *Y*, and *Z*.[132] They are equated by projecting the spectral distribution of the radiant power of the source of interest S(λ) onto the color matching functions shown in Figure 7.9:

$$\begin{aligned} X &= \int \mathrm{S}(\lambda)\ \mathrm{x}\ (\lambda)\ d\lambda \\ Y &= \int \mathrm{S}(\lambda)\ \mathrm{y}\ (\lambda)\ d\lambda \qquad (5) \\ Z &= \int \mathrm{S}(\lambda)\ \mathrm{z}\ (\lambda)\ d\lambda \end{aligned}$$

Note, *X*, *Y*, and *Z* are the tristimulus values, S(λ) is the spectral irradiance of the source, and x (λ), y (λ), and z (λ) are the color matching functions. Finally, the chromaticity coordinates (x, y, z) can be calculated using:

$$\begin{aligned} \mathrm{x} &= X / (X + Y + Z) \\ \mathrm{y} &= X / (X + Y + Z) \qquad (6) \\ \mathrm{z} &= X / (X + Y + Z) \\ 1 &= \mathrm{x} + \mathrm{y} + \mathrm{z} \end{aligned}$$

The chromaticity coordinates are used to normalize the brightness of the object. The z coordinate is not independent of x and y, so a two dimensional space is created. Once the chromaticity coordinates (x, y) are calculated, they can be plotted in a rectangular coordinate system as shown in Figure 7.10. In this diagram, completely saturated color or light representing a very narrow wavelength band is found on the outer horseshoe-shaped locus of possible values. The line joining the red and violet ends of the locus is termed the purple boundary and can only be accessed by combining both saturated red and violet light at different ratios. White colored light, which is found near the center of the diagram, can be created in many ways using two or more wavelengths or wavelength bands of saturated light at specific intensities.

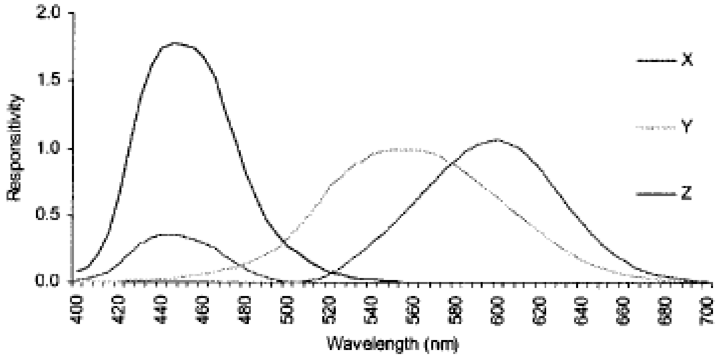

Figure 7.9 Color matching functions.[132]

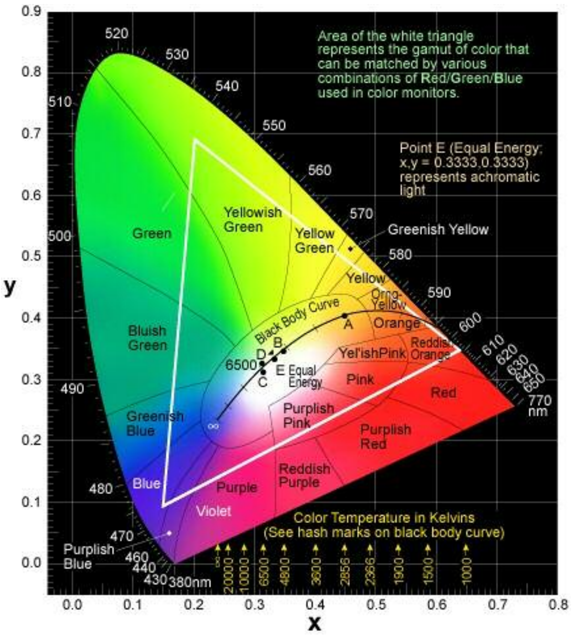

Figure 7.10 1931 CIE chromaticity coordinate diagram.

Standards for lighting have also been developed based on the radiation from a blackbody. The color temperature of a blackbody is defined as its temperature for a particular perceived color. For example, a blackbody radiator with a color temperature of 10,000 K appears blue. For non-blackbody radiators, the CCT is the temperature of a blackbody radiator which has a color that most closely resembles that of the light source. The CCT, therefore, only specifies chromaticity and gives no information about the spectral power distribution. Besides being used as a measure of chromaticity, the CCT is also used to specify the color rendering index of a light source. The color of two light sources may appear identical when viewed directly and will therefore have the same color temperature; however, the color of the reflected light from an object illuminated by these two sources may be significantly different. A method defined by CIE to distinguish between two identical sources uses a color rendering index (CRI). The reflection from an object of a light source of a particular correlated color temperature is compared to the reflection from the same object under illumination from a blackbody radiator of the same color temperature. The similarity between the two sources is ranked on a scale of 0-100, where a rating of 100 is a perfect match. Sources with a CRI value above 80 are considered high-quality lighting sources. A source with CRI below 70 is considered undesirable for natural lighting requirements. The CRI and CCT reflect the chromaticity and spectral output of a light source compared to the sun and can represent very unsaturated colors between red and blue. A more comprehensive chromaticity measure is, however, needed for colors such as green. An intensity versus wavelength spectrum of a source describes the source in much more detail than chromaticity numbers and should always be referenced, since much information is lost converting spectral characteristics into chromaticity data.

7.5 Previous techniques and structures for WOLEDs

Although improving the color quality and saturation of the red, green, and blue organic emitters for full color flat-panel display applications has been a goal for researchers for the past two decades, creating white-light emission is believed to be equally or possibly more important. The first WOLED was produced by Kido et al. in 1993.[133] Since this time the color purity, efficiency, lifetime, and brightness have drastically increased. With most organic materials emitting in only one third of the visible spectrum, there has been extensive work done to create WOLEDs using multilayer multi-emitter configurations. This brings an increase of complexity to the fabrication process of these devices. Although high efficiencies, long lifetimes, and high color quality is achieved, higher fabrication cost and lower color reproducibility plague these devices. New techniques involving excimers, dimmers, and macromolecules decrease fabrication complexity but introduce new problems in some cases such as color purity. This section will introduce the techniques in creating white-light emission from electroluminescent devices.

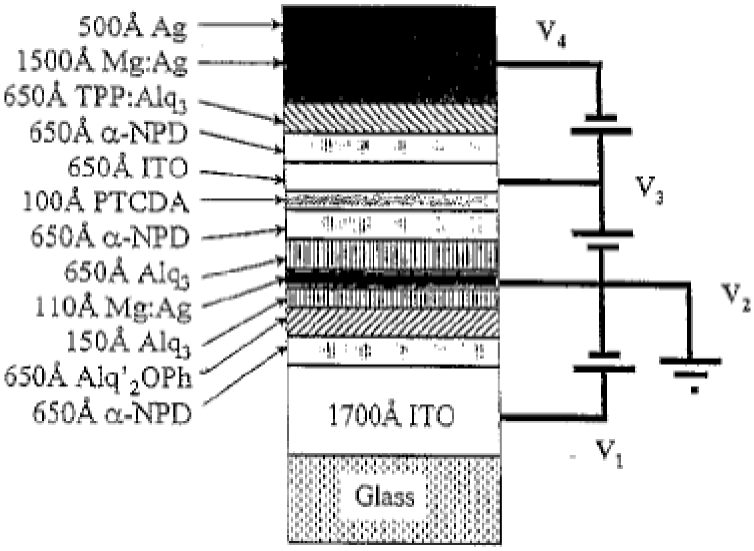

Figure 7.11 Complex WOLED using a stacked OLED structure.[134]

In general, white light can be produced by mixing the emissions of two complementary colors or three primary colors each at specifically balanced intensities. WOLEDs can take advantage of this idea by the stacking of multiple OLEDs (Figure

7.11) or by the use of a single OLED that emits red, green, and blue light from a multilayer/emitter device, where each color is produced by a certain thin-film layer housing a specific light-emitting molecule (Figure 7.12).[135,136] In the multilayer/emitter device, the color output of the WOLED can be tuned by adjusting dopant concentrations,[137] varying layer thicknesses,[138] or introducing charge-blocking layers.[139] However, introducing these numerous variables can create difficulties in achieving proper charge carrier balance and exciton confinement, which can lead to decreases in efficiencies and poor color reproducibility. One of the major disadvantages of multilayer multi-emitter devices is differential aging (in general, the lifetime and stability of the blue-emitting materials are much less than those of the green and red). This can alter the color of the WOLED over time thereby degrading its initial white purity. In addition, these highly-complicated multilayer WOLED structures are usually fabricated by wasteful, relatively high-cost methods such as thermal vapor deposition. Contrastingly, solution-processing techniques that utilize ink-jet printing[140] or screen printing[141] can decrease the fabrication cost and complexity of these devices.

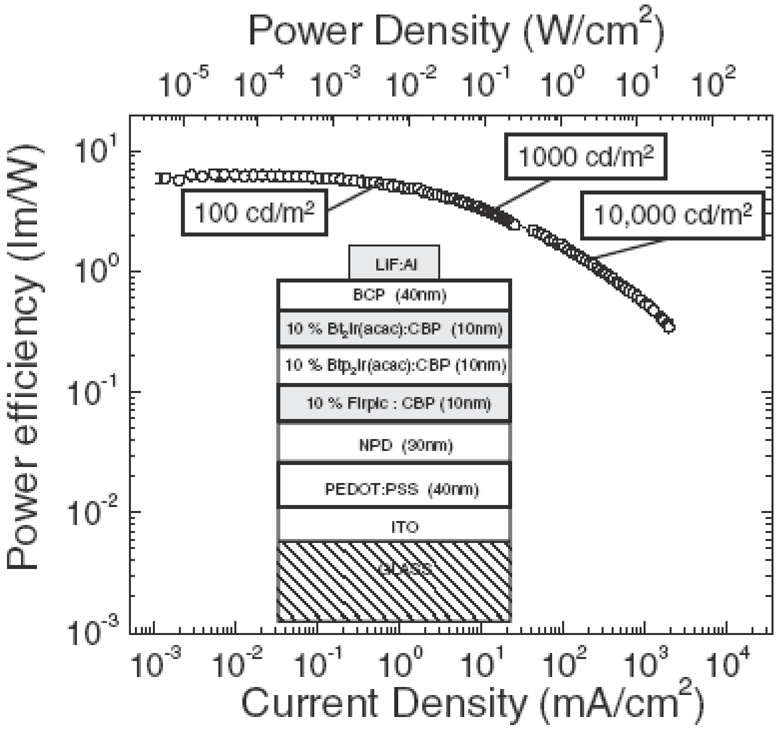

Figure 7.12 Multilayer OLED utilizing tri-color emission from three separate layers.[142]

Single-layer solution-processed WOLEDs can decrease the cost and complexity of fabrication but can also introduce many challenges and drawbacks (such as proper charge transport and cathode quenching). There have been several methods proposed to make such simple devices high-performing such as the following: blending of two or more emitting polymers,[143,144] doping a polymer layer with multiple small-molecule emitters,[145,146] or utilizing configurations that incorporate exciplex[147] or excimer[148] emission. Although these are possible ways of producing white light from a simple solution-processed OLED, there are significant drawbacks to each of these approaches. Classical polymer-based systems are typically difficult to purify and often exhibit poor batch-to-batch reproducibility. In general, blends of small molecule emitters and polymer dispersions of emitters have limited solubility and also tend to aggregate or phase separate, which often results in decreased device performance and poor color stability. Devices utilizing exciplex emission often show bias-dependent spectral output. In addition, their formation changes the transport properties and decreases the quantum efficiency of the device.[147] Finally, devices utilizing excimers generally show off-white color emission with poor CIE values which are far from the standard white (0.33, 0.33).

7.6 White-light electroluminescence from polymers and macromolecules

Up until the last several years, polymers and small molecules have been the two main classes or divisions of materials used for the fabrication of OLEDs. Each of these materials has their own positive and negative aspects. Polymers can be solution processed, allowing for high-volume production and simplified fabrication techniques such as stamping, blade coating, ink-jet printing, and roll-to-roll processing.[97,98,149] Still, there are many challenges that polymeric-based OLEDs are faced with such as relatively low quantum efficiencies compared to their small-molecule counterparts (difficulty in incorporating triplet emitters), lack of reproducible high purification, and the inability to create multilayer devices without the use of cross-linking or different polar solvents.[150] Small molecules, on the other hand, have the ability to produce multilayer OLEDs with relatively high quantum efficiencies. They can be easily purified which allows OLEDs to exhibit long device lifetimes. A drawback of small molecule-built OLEDs involves the complex and high-cost manufacturing of these devices due to their inability to be easily solution processed.

An additional drawback (at least for WOLEDs) that both polymer and small molecule organic materials share is that neither can efficiently emit broadly enough to cover the entire visible spectrum. Consequently, strides to incorporate several emitters on a single polymeric chain have been undertaken.[151,152] Still, these complex polymers suffer from the same challenges of traditional polymeric materials.

Macromolecules provide another choice of materials available for the construction of simple-structured WOLEDs. In order to make such materials emissive, fluorescent or phosphorescent emitters need to be incorporated into their structure. This type of hybrid molecule combines the advantages of both small molecular and polymeric materials. These molecules are monodispersible with easy purification, yet are solution-processible and able to form a self-standing film. There are several macromolecule architectures that have been investigated. Monodispersed dendrimers are possible candidates for WOLED materials because of their highly branching structure and multi-functionality.[153,154] Several moieties can be attached onto the exterior of the globular core including emitter, charge transport, or absorber. However, the tedious synthetic procedures needed to create these structures make for little practical usage. An efficient alternative to a typical organic dendritic core is the use of a new class of inorganic cores known as Polyhedral Oligomeric Silsesquioxanes (POSS).[155] Sellinger et al.[156] reported synthesis of an octavinyl-POSS substituted with a hole-transport moiety via Heck coupling, and Xiao et al.[157] reported the synthesis of oligophenylenefunctionalized POSS utilizing a Grignard mechanism. The POSS-substituted products in both of the above mentioned proved to have superior thermal properties and device performance than the substituent that was not incorporated onto the POSS core. However, both of these methods did not yield pure octa-functionalized POSS and instead yielded mixtures of incompletely substituted POSS compounds. Imae et al.[158] reported the synthesis of a perfectly controlled eight-carbazole substituted POSS via hydrosilylation reaction of 9-vinylcarbizole with octakis(dimethylsiloxy)POSS. The small size of the vinylcarbazole group may have facilitated the complete substitution on POSS. Advantages of using functionalized POSS macromolecules include the ease of synthesis, high glass-transition temperatures, high solubility, good film-forming properties, and high purity via column chromatography.

CHAPTER 8

WHITE-LIGHT ELECTROLUMINESCENCE FROM A SINGLE MACROMOLECULE

This chapter discusses the efforts in the design of electroluminescent devices employing several new organic-inorganic lumophore-functionalized macromolecules. This work will potentially lead to the production of single-molecule white-light emitters, which can be solution processed and applied to existing OLED technologies with simple fabrication techniques such as spin casting, inkjet printing, or screen printing. This kind of single-emissive molecule combines the advantages of both small molecular and polymeric materials. These molecules will be monodispersible with easy purification, yet are solution processible and form a self-standing film. It is envisioned that such a single-molecule emitter will drastically simplify WOLED device fabrication.

8.1 Chemistry, materials, and device structure

Choosing the proper electroluminescent lumophores and base core structure was an important first step in the development of an electroluminescent WOLED that consists of a single macromolecule and its white-light emission. To limit the complexity and number of variables in creating white-light emission, a blue/orange bi-color system was a logical experimental starting point. A fluorine-based blue emitter 9-hexenyl-2,7-bis-(2,2-diphenyl-vinyl)-9-methyl-fluorene (Blue) and a donor-accepter fluorescent orange lumophore 2-[2-tert-butyl-6-(2-{4-[(4-hexyl-phenyl)-phenyl-amino]-phenyl}-vinyl)-

pyran-4-ylidene]-malononitrile (Orange) were synthesized according to previous publications.[159,160] These lumophores were then attached to the vertices of a relatively stiff cubical structure based on core Polyhedral Oligomeric Silsesquioxanes or (1,3,5,7,9,11,13,15-octakis(dimethylsilyloxy)pentacyclo-[9.5.1.1^{3,9}.1^{5,15}.1^{7,13}]-octasiloxane) (POSS) in multiple configurations.[155,161] The cubic form of POSS has the chemical formula ($R_8Si_8O_{12}$) and consists of a rigid silica-like inorganic core that can be covalently linked to eight organic groups. These molecules are excellent platforms for nanotechnology applications because their spatial geometry can be perfectly defined, and they can be synthesized to have great versatility of properties. With these eight vertices available for the covalent bonding of either lumophore, octa-functional POSS$(O)_8$, octa-functional POSS$(B)_8$, and mixed POSS$(B)_7(O)_1$ were synthesis by optimizing reaction conditions for the correct ratio of mixed dyes.[162] All POSS-dye materials have shown better thermal stability and better film-forming properties than their free dye counterparts. The chemical structures of the orange and blue free lumophores, POSS, POSS$(O)_8$, POSS$(B)_8$, and POSS$(B)_7(O)_1$ are shown in Figure 8.1. In addition, the optical properties of the emitting structures are presented in Table 8.1.

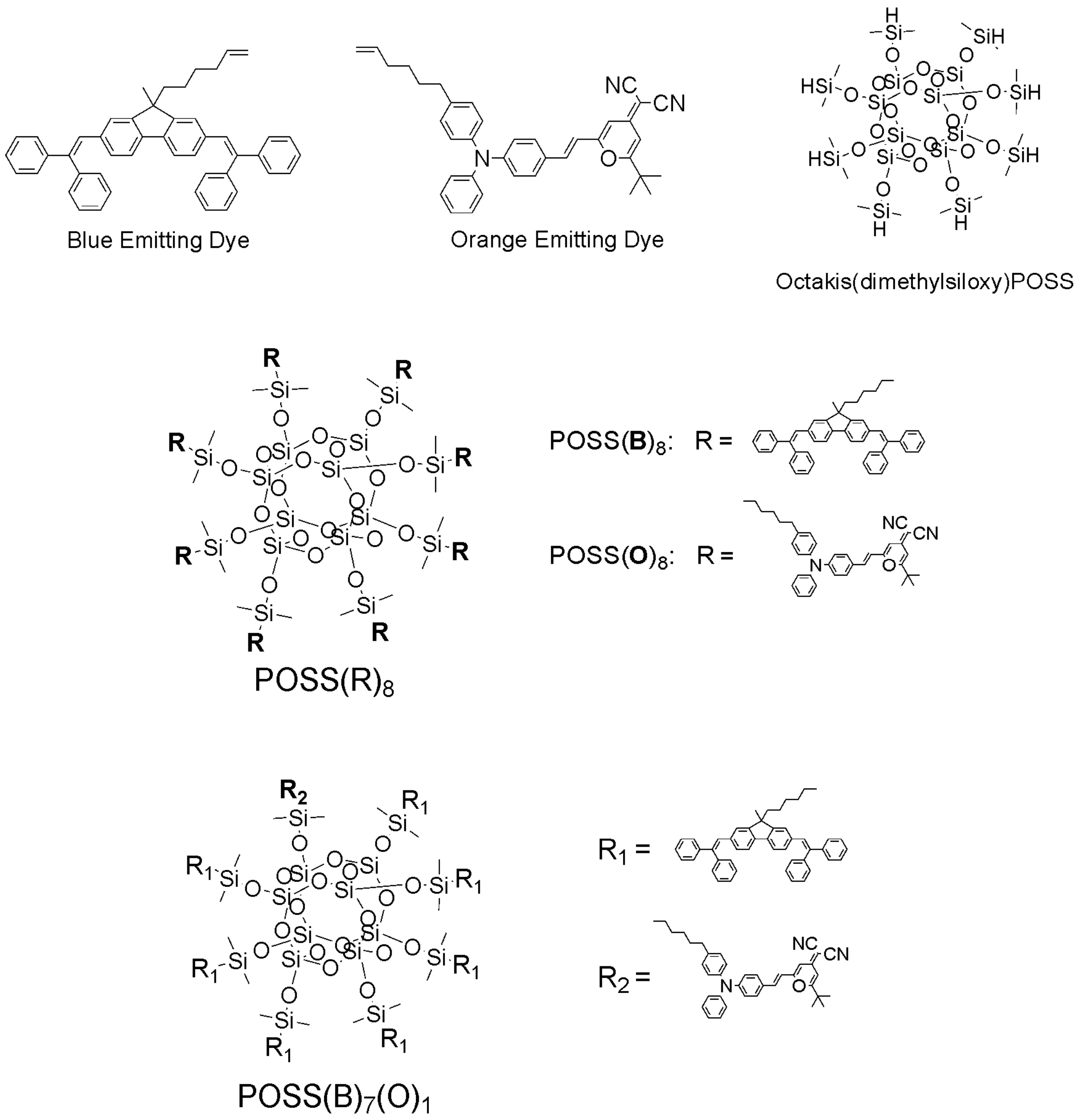

Figure 8.1 Schematic structures of synthesized materials. Oktakis(dimethylsiloxy)POSS was purchased from Sigma-Aldrich.

Table 8.1 Absorption and photoluminescence spectra of the five investigated molecules in solvent CH_2Cl_2 and in a neat film spun cast from cyclopentanone on glass substrates.

Materials	Solution		Solid Thin Film	
	Abs max (nm)	λ max (nm)	Abs max (nm)	λ max (nm)
Blue	372	450	376	456
Orange	470	612	478	619
$POSS(B)_8$	373	450	373	456
$POSS(O)_8$	466	612	476	621
$POSS(B)_7(O)_1$	372,472	450,610	375,480	590

In simple single-layer devices such as these, it is desired to incorporate a host that has both good electron and hole transporting properties. Focusing mainly on the emissive properties of the organic-inorganic light-emitting lumophore-functionalized macromolecules, a common non-enhanced two-part host of polymer PVK and electron-transporting additive PBD was used.[145] Nonconjugated polymer PVK, purchased from Sigma-Aldrich, is well-known for its high energy blue-emissive singlet excited state, favorable film-forming properties, and hole mobility of about 10^{-5} cm^2 V^{-1} s^{-1}.[163] Additive PBD, a small molecule dopant sublimed to decrease impurities, was used to increase electron transport. In all experiments, equal weights of PVK to PBD were used in the solvent chloroform at a concentration of 15 mg/ml. The concentrations of lumophore emitters were added at 1% of the total weight. Chloroform solutions containing the host and luminescent materials were prepared by stirring and then passed through 0.2 μm filters before spin casting onto ITO-covered glass substrates. Before the application of the single organic layer, the substrates were cut into 1 in.^{2} pieces and cleaned using consecutive ultrasonic baths of acetone, methanol, and isopropanol. Air plasma ashing for 2 min followed. Next, the active layer was prepared by spin casting at 1000 rpm for 60 s. Finally, films were dried at room temperature or 70-100°C for 15 min (same results) in a nitrogen-filled glove box and then immediately transferred to a vacuum of about 5×10^{-7} Torr where the thermal evaporation of a Mg:Ag cathode at a 10:1 ratio was completed.

8.2 Spectrum balancing and energy transfer

Three types of electroluminescent systems were investigated. These systems incorporated either free lumophores, octa-functional POSS$(R)_8$, or mixed POSS$(B)_7(O)_1$ as dopants in an ITO/PVK:PBD:dopant/Mg:Ag structured device. Several ratios of blue to orange emitters were prepared for both the free lumophores and octa-functional POSS$(R)_8$ while mixed POSS$(B)_7(O)_1$ is inherently seven blues to one orange. The spectrum, corresponding CIE coordinate values, brightness, and efficiencies were collected and compared to investigate energy transfer mechanisms, quenching means, and aggregation effects.

The first of these three systems utilize free lumophores in a ITO/PVK:PBD:blue:orange/Mg:Ag structured device. Several ratios of blue to orange free lumophores were used to correctly identify the spectral emission balance that provided CIE coordinates closest to (0.33, 0.33). As shown in Figure 8.2 (a), a ratio of sixteen blues to one orange provides white-light emission, rendering CIE coordinates of (0.33, 0.38). The blue and orange peaks, located at 440 nm and 560 nm respectively, are at lower wavelengths than the corresponding photoluminescence data given in Table 8.1.

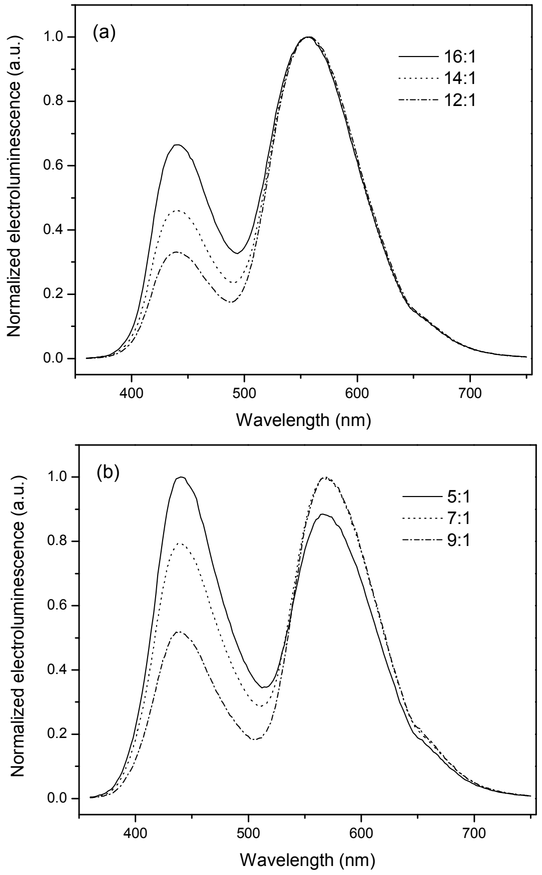

Figure 8.2 (a) Electroluminescence spectra of three devices using blue:orange free lumophore dyes at ratios of 12:1, 14:1, and 16:1. (b) Electroluminescence spectra of three devices using POSS(B)$_8$:POSS(O)$_8$ at ratios of 5:1, 7:1, and 9:1.

This is due to a decrease in aggregation effects when binding the lumophores into a host structure as compared to a neat film. As can be seen from the spectra depicted in Figure 8.2, the PBD and PVK emission peaks of 390 nm and 410 nm are absent. Therefore, excitons that form on either PBD or PVK must transfer to neighboring dopant molecules through Förster energy transfer or decay nonradiatively. Both the blue lumophore and PVK have emission spectra that overlap quite well with the orange lumophore's absorption spectrum causing efficient sequential Förster energy transfer.[164] The free dye lumophore system, that utilized a sixteen blue to one orange ratio, was then compared to a device with the structure of ITO/PVK:PBD:POSS(B)$_8$:POSS(O)$_8$/Mg:Ag. Figure 8.2 (b) shows that a ratio of seven POSS(B)$_8$ to one POSS(O)$_8$ gives the best balance of emission to result in CIE coordinates of (0.34, 0.34) which is extremely close to pure white-light emission (Figure 8.3). The difference in the ratios needed to create white light between the free lumophore device and the POSS(B)$_8$:POSS(O)$_8$ device is believed to be due to a decrease in the energy transfer from the blue to the orange emitter when these lumophores are incorporated in the POSS(R)$_8$ structure. Once an exciton is trapped on a POSS(B)$_8$ molecule, it is more likely to decay as a blue photon or by nonradiative processes, thereby increasing the amount of blue emission and decreasing the overall efficiency of the device (Figure 8.5).

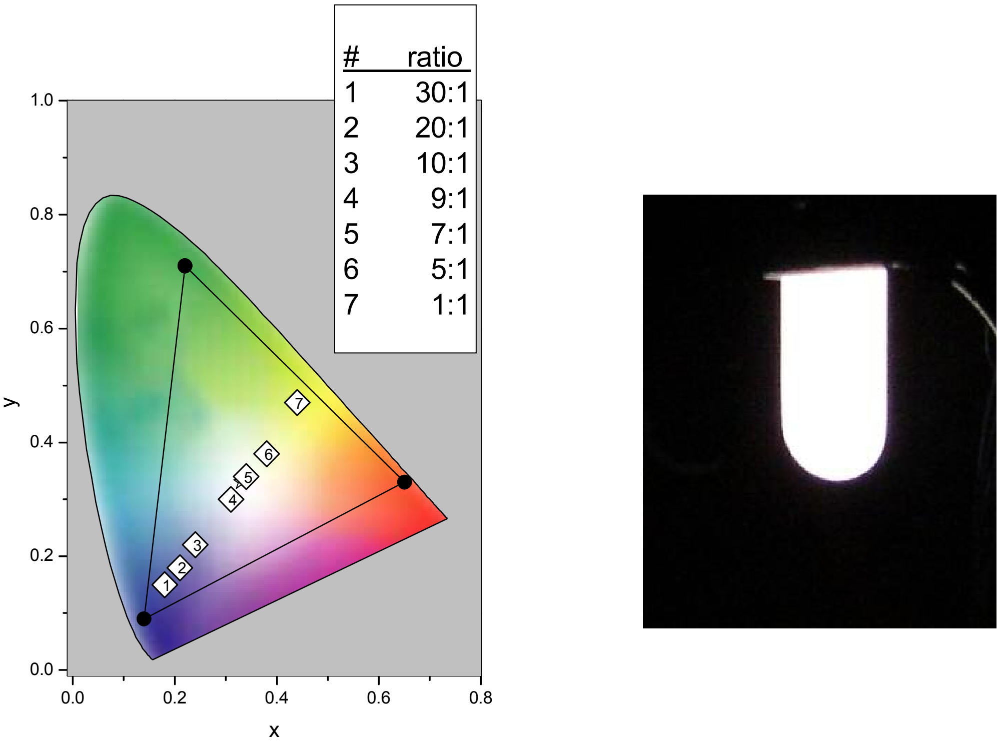

Figure 8.3 (a) CIE diagram depicting the coordinate values of a ITO/PVK:PBD:POSS(B)$_8$:POSS(O)$_8$/Mg:Ag WOLED with varying ratios of POSS(B)$_8$:POSS(O)$_8$. Digital picture of (#5 from (a)) 7:1 ratio POSS(B)$_8$:POSS(O)$_8$ device exhibiting CIE coordinates of (0.34, 0.34).

8.3 Characterization of free-lumophore and macromolecule dispersions

In the third system, both the blue and orange lumophores were incorporated on the same macromolecule. With such efficient energy transfer from the high energy blue to the lower energy orange singlet state, the maximum number of blue emitters was chosen. Devices employing macromolecule POSS(B)$_7$(O)$_1$ in a ITO/PVK:PBD:POSS(B)$_7$(O)$_1$/Mg:Ag device were characterized. It was found to be beneficial to compare this device to the two previous systems when incorporating the same ratio of emitters. The number of blue emitters to orange emitters for this final comparison was kept constant at a ratio of seven to one for all three systems. Their electroluminescence spectra are compared in Figure 8.4. Each device was designed to contain the same number of blue and orange emitters; however, the POSS$(B)_7(O)_1$ device showed the least amount of blue emission. We believe this is due to the rapid charge transfer from the seven blue lumophores to their neighboring lower energy orange lumophore when both colored emitters are located on the same core. When devices employing free lumophores or monochromatic octal-functional POSS$(R)_8$ are used, intermolecular spacing between blue and orange emitters increases which decreases energy transfer and allows for more nonradiative paths of exciton decay. This can be seen in the comparison of external quantum efficiencies and electroluminescent brightnesses shown in Figures 8.5 and 8.6. The POSS$(B)_7(O)_1$ device exhibits superior electroluminescent characteristics over the other two systems, but CIE coordinates of (0.41, 0.51) correspond to an unsaturated orange-colored emission. To overcome the imbalance of emission and to saturate the sequential energy transfer from the blue to orange dye, the incorporation of additional blue lumophores was hypothesized to be the next chemical engineering step.

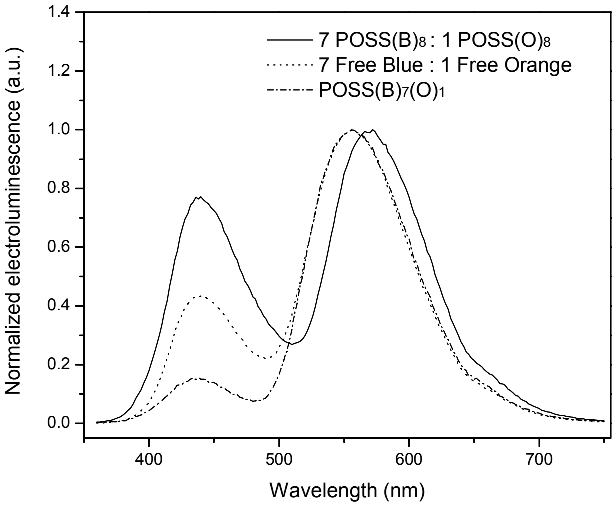

Figure 8.4 Electroluminescence spectrum comparison of three device systems: POSS$(B)_8$:POSS$(O)_8$, (free blue):(free orange), and POSS$(B)_7(O)_1$. All three systems incorporate a seven blue to one orange emitter doping ratio in a ITO/PVK:PBD:dopant/Mg:Ag device structure.

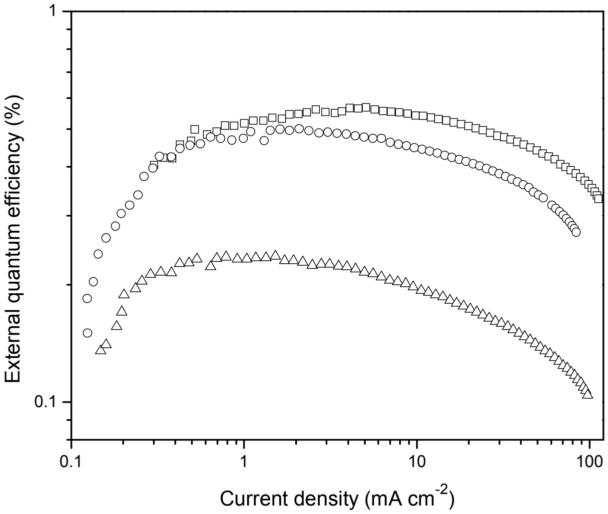

Figure 8.5 Forward external quantum efficiency versus current density of three device systems: POSS$(B)_7(O)_1$ (squares), (free blue):(free orange) at a 7:1 ratio (circles), and POSS$(B)_8$:POSS$(O)_8$ at a 7:1 ratio (triangles).

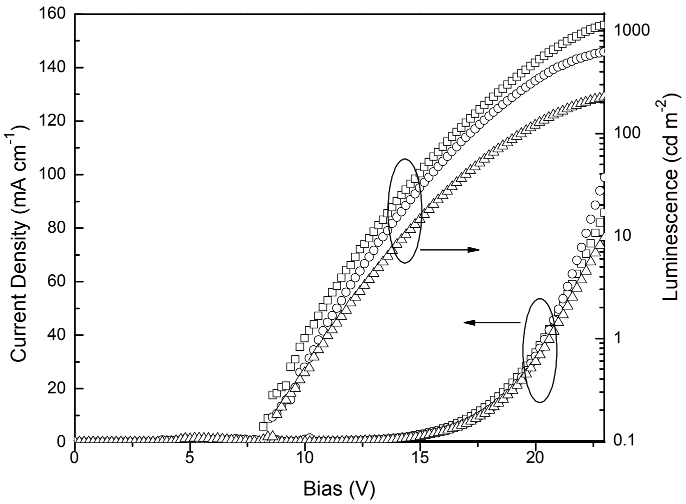

Figure 8.6 Voltage-current density and voltage-luminescence characteristics of POSS(B)$_7$(O)$_1$ (squares), (free blue):(free orange) at a 7:1 ratio (circles), and POSS(B)$_8$:POSS(O)$_8$ at a 7:1 ratio (triangles).

8.4 Second generation multi-lumophore functionalized macromolecule

The previous results revealed the need for an increase in the number of blue lumophores per macromolecule. To satisfy this need, a macromolecule incorporating twenty-one blue lumophores was synthesized. In addition, the high energy orange lumophore was replaced with a lower energy yellow lumophore[160] to decrease the probability of Förster energy transfer between the two emitters. The materials and chemical structures used in this second generation of experiments are shown in Figure 8.7. The photoluminescence and absorption spectra of these materials is given in Table 8.2.

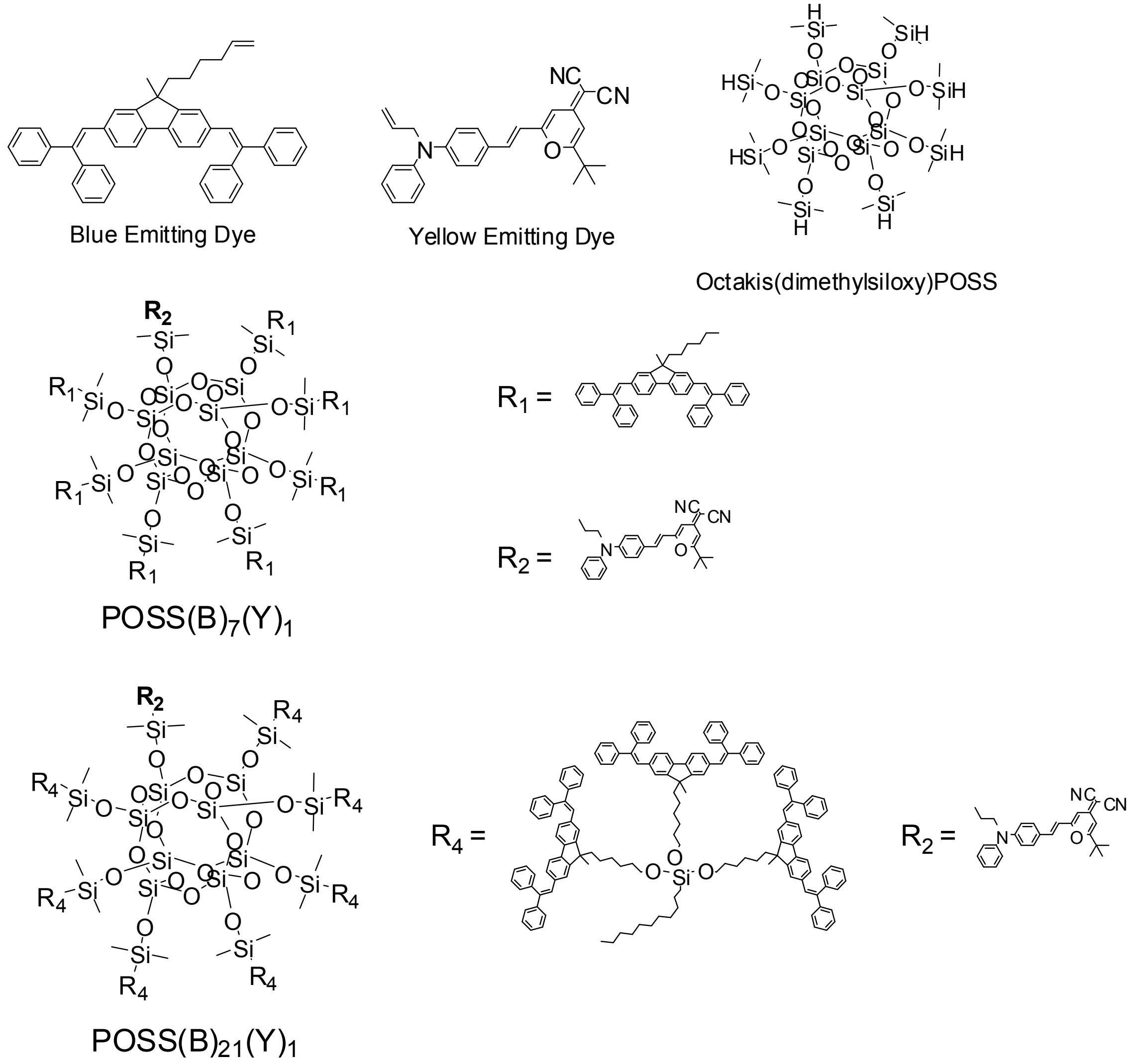

Figure 8.7 Schematic structures of synthesized materials.

Table 8.2 Absorption and photoluminescence spectra of the four investigated molecules in solvent CH_2Cl_2 and in a neat film spun cast from cyclopentanone on glass substrates.

Materials	Solution		Solid Thin-Film	
	Abs max (nm)	λ max (nm)	Abs max (nm)	λ max (nm)
Blue	372	450	376	456
Yellow	461	574	469	619
$POSS(B)_7(Y)_1$	372,474	450,580	376,475	577
$POSS(B)_{21}(Y)_1$	372,475	450,578	NA	560

The same device structure and host of PVK and PBD were used in the second generation of experiments. Several electroluminescent devices were fabricated with a similar (ITO/PVK:PBD:dopant/Mg:Ag) architecture utilizing the different luminescent dopants. The free lumophore-doped devices showed electroluminescent spectral peaks of about 440 nm for the blue and 554 nm for the yellow (Figure 8.8). Notice that again, the high energy emission peaks of PVK (410 nm) and PBD (390nm) are nearly absent in each curve. The absence of the host emission can be clearly seen in the curve representing the electroluminescence spectrum of the ITO/PVK:PBD:Yellow/Mg:Ag device. In blended devices such as these, excitation of the emitter occurs either via the formation of excitons on the host followed by Förster energy transfer to the emitter or direct charge carrier trapping on the emitter itself. If excitons form on the PVK or PBD host, nearly complete energy transfer occurs to the dopant emitter.

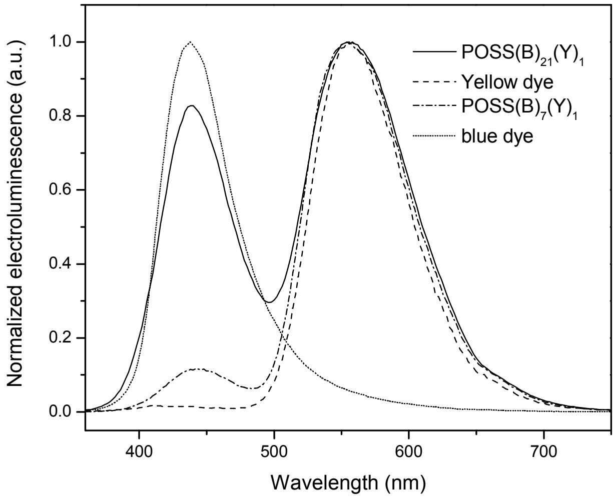

Figure 8.8 Electroluminescence spectra of four devices which incorporate either free blue dye, free yellow dye, POSS$(B)_7(Y)_1$, or POSS$(B)_{21}(Y)_1$.

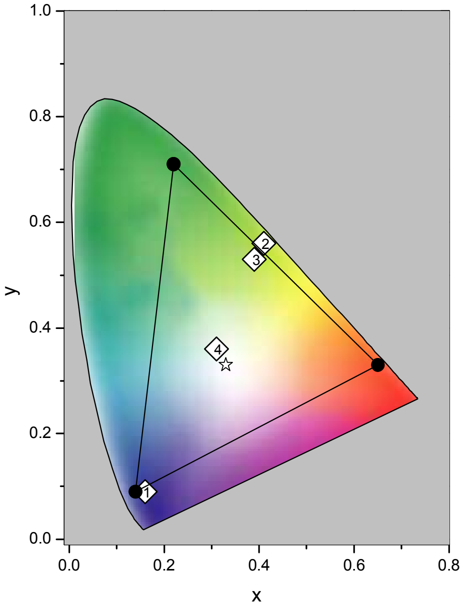

Figure 8.9 CIE chromaticity diagram of four devices which incorporate either free blue dye (1), free yellow dye (2), POSS$(B)_7(Y)_1$ (3), or POSS$(B)_{21}(Y)_1$ (4).

A macromolecule incorporating seven blues and one yellow lumophore was then implemented into the same device structure as the previous free lumophores. The electroluminescence spectrum was compared and showed similar emission peaks of 440 nm and 554 nm indicating that the attached lumophores retained their optical gap energy. The blue emission intensity was nearly 10 times less than the yellow indicating that an efficient energy transfer from the blue lumophores to the single yellow lumophore occurred. The POSS$(B)_7(Y)_1$ macromolecule device produced non-white emission with CIE coordinate values of (0.39,0.53) but exhibited far better quantum efficiencies than that of a free lumophore device with the same ratio of seven blue to one yellow (Figure 8.10). This increase in device performance is believed to be attributed to the elimination of aggregation effects when employing the POSS$(B)_7(Y)_1$ macromolecule.

To balance the blue and yellow emissions, an increase in the number of blue lumophores was employed. The POSS$(B)_{21}(Y)_1$ blended device revealed a nearly balanced spectrum that is shown in Figure 8.8 with corresponding CIE coordinate values of (0.31, 0.37). Tripling the number of blue emitters increased the blue emission by nearly 8 times. This nonlinear result is believed to have occurred due to a saturation of the yellow lumophore. Evidence towards this assertion can be found in the observation of a decrease in the quantum efficiency and brightness compared to the POSS$(B)_7(Y)_1$ macromolecule-incorporated device (Figure 8.10 and 8.11). The emission color of the POSS$(B)_{21}(Y)_1$ blended device is stable over several orders of current density as can be seen in Figure 8.12. This will allow these devices to emit high-purity white light for a wide range of operating powers.

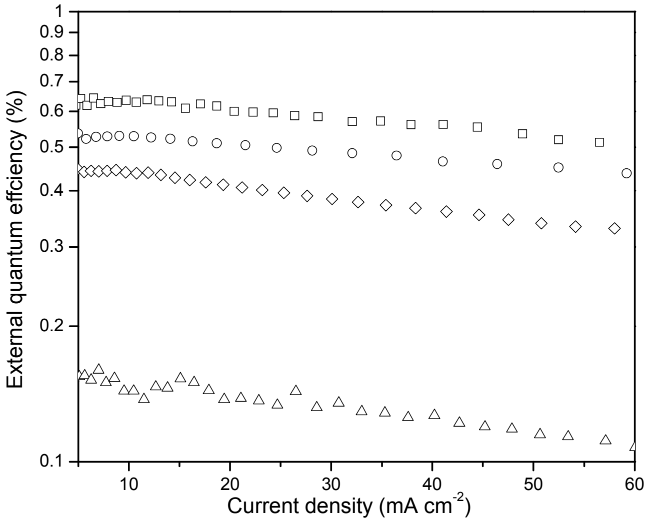

Figure 8.10 External quantum efficiency versus current density of four devices incorporating either POSS(B)$_7$(O)$_1$ (squares), POSS(B)$_{21}$(O)$_1$ (circles), free blue and yellow dye at a seven to one ratio (diamonds), or free blue dye (triangles) in a ITO/PVK:PBD:dopant/Mg:Ag structure.

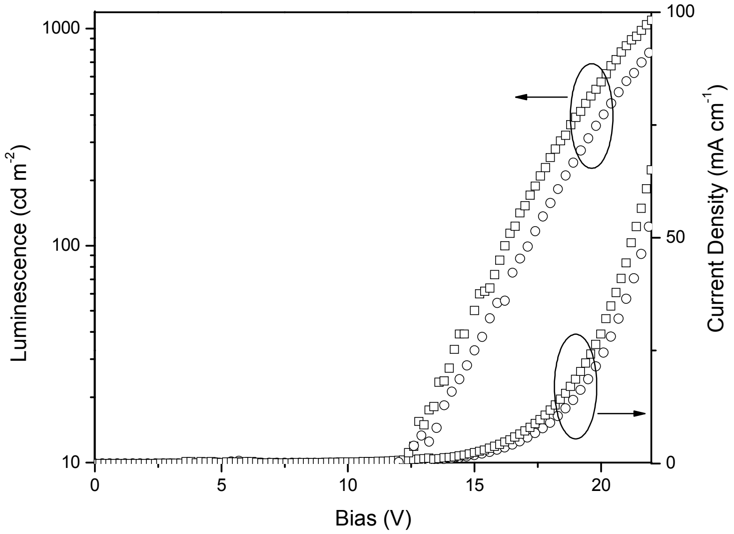

Figure 8.11 Voltage-current density and voltage-luminescence characteristics of devices incorporating POSS(B)$_7$(O)$_1$ (circles) and POSS(B)$_{21}$(O)$_1$ (squares) in a ITO/PVK:PBD:dopant/Mg:Ag structure.

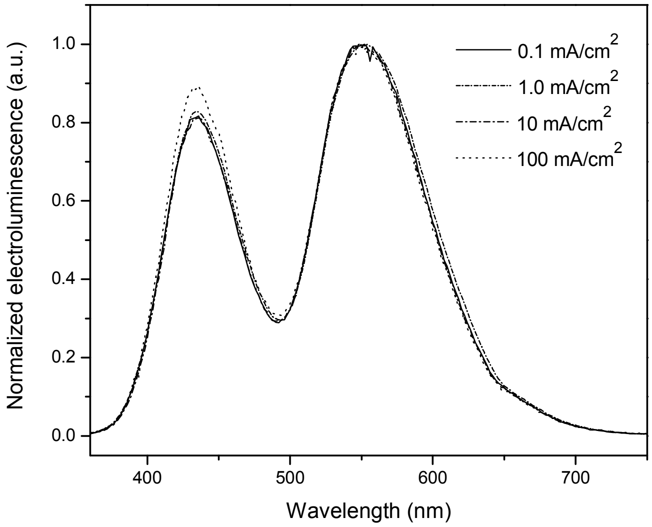

Figure 8.12 Electroluminescence spectrum of ITO/PVK:PBD:POSS(B)$_{21}$(O)$_1$/Mg:Ag device at several current densities.

8.5 Preliminary phosphorescent data and future WOLED work

Future goals for this project include a device that features a fluorescent blue singlet emitter in conjunction with phosphorescent red and green emitters all incorporated on a single POSS nanoparticle core. Theoretically, 100% of the excitions generated by electrical injection can be harvested by electrophosphorescent OLEDs.[165] Many electrophosphorescent WOLEDs have been reported to exhibit high quantum efficiencies (reaching 20 lm W^{-1}).[148,166-168] Phosphorescent molecules have the ability to harness the triplet excitons that constitute three-quarters of the bound electron–hole pairs that form during charge injection, and which (unlike singlet excitons) would otherwise recombine non-radiatively. This macromolecule would utilize the fluorescent blue lumophore to harness all of the electrically-generated high-energy singlet excitons (~25%) and the red and green phosphorescent dopants to harvest the remainder of the lower-energy triplet excitons (~75%). The reason for this future step is to drastically increase device efficiencies and possibly decrease the number of blue emitters needed to compared to the lower-energy green and red emitters. Although this next step is predicted to drastically increase device quantum efficiency, there will still be a few challenges to overcome. It is expected that energy losses will be suffered due to triplet quenching by the fluorescent blue emitter. In addition, energy transfers from the high energy blue fluorophore to the lower energy red and green phosphors could also decrease efficiencies. The initial steps in creating phosphorescent-functionalized POSS (Figure 8.13) cores have been taken and preliminary device characterization is shown in (Figure 8.14).

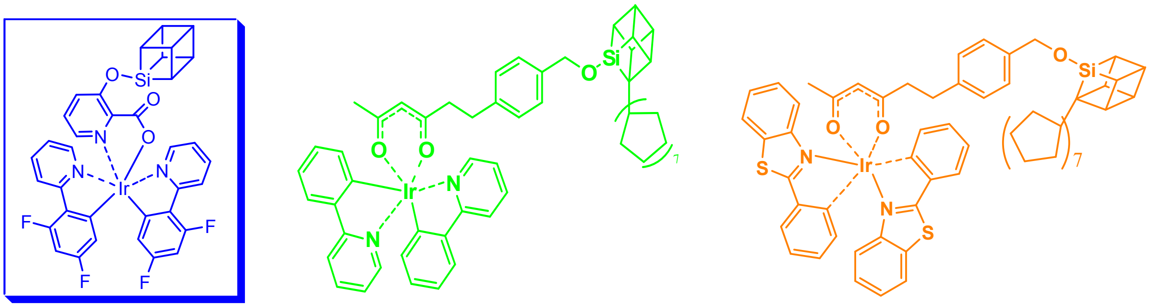

Figure 8.13 Schematic structures of synthesized phosphorescent-functional POSS.

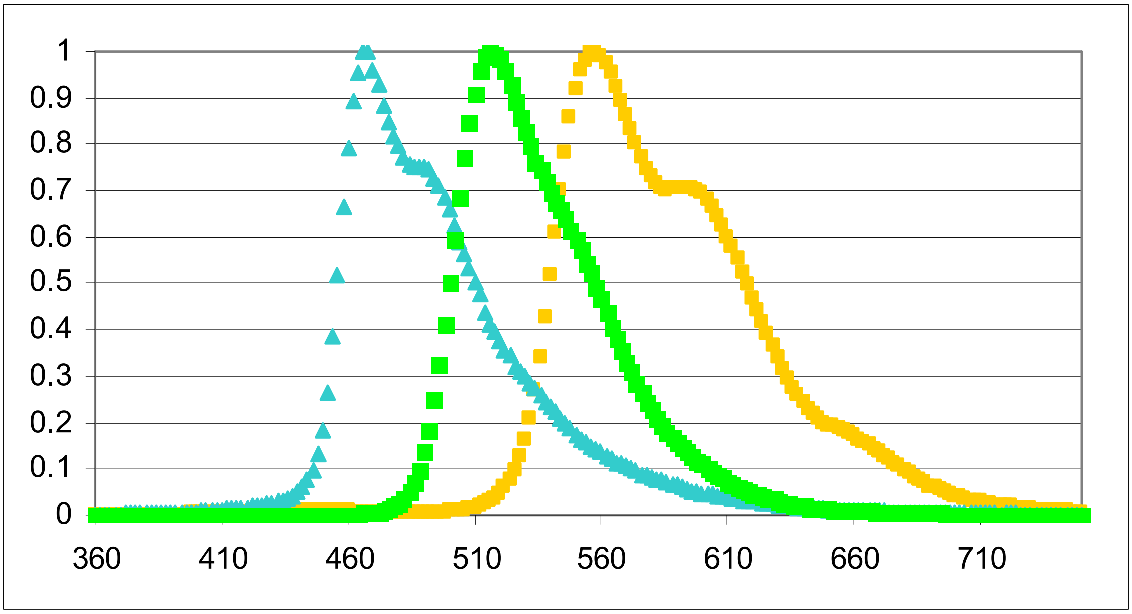

Figure 8.14 Electroluminescence spectrum comparison of the three phosphorescent-functional POSS device systems.

CHAPTER 9

SUMMARY AND CONCLUSIONS

In the first part of this dissertation, metal/organic/ITO structures, including regularly structured OLEDs, were demonstrated to contain multiple nonvolatile conductance states that can be programmed by the application of an external bias above a certain threshold voltage (V_{th}). These conductance states are stable and in turn can be probed by the use of a bias lower in value then V_{th}. The unbiased retention time of states is more than several weeks, and more than 48,000 write-read-rewrite-read cycles have been performed with minimal degradation. It is found that the programming of a continuum of conductance states is possible and techniques to do so were outlined. The electrical conductivity of the highest and lowest states can differ by six orders of magnitude. Switching speeds below 50 ns were shown, resulting in an energy requirement of about 100 pJ to switch from one conductance state to another. The memory phenomenon was shown to be influenced by the active layer thickness, gaseous environment, and anode/surface roughness while temperature dependence is limited. The electrical characteristics of these devices are consistent with metal diffusion or filament phenomena found in metal-insulator-metal structures, suggesting a possible mechanism by which the states are stored.

Several experiments have provided evidence into filament formation and the electrical processes that result. We believe that thermally activated electron tunneling between metal particles entrapped in the organic layer and energy dependent trapping and freeing of electrons in tunneling barriers are responsible for the current characteristics seen in these devices. We believe oxygen has a prominent effect on the amount and size of the traps available. An in-depth understanding of this mechanism is still needed. Once the mechanism behind the switching effect and existence of multiple conductance states is well understood, steps of optimization and advancement of fabrication can take place to push these devices towards a high-density, low-cost, and reliable data storage application.

In the second part of this dissertation, electroluminescent devices employing several new organic-inorganic lumophore-functionalized macromolecules were presented. In this study, macromolecules incorporating several lumophores covalently bonded to the vertices of a cubical core structure based on Polyhedral Oligomeric Silsesquioxane (POSS) in multiple configurations are implemented as light-emitting centers. A study of energy transfer in several systems was carried out to understand the requirements needed to create white-light emission from a single macromolecule. A single macromolecule incorporating twenty-one blue and one yellow lumophore was shown to exhibit field-independent stable white-light electroluminescence with Commission Internationale de l'Eclairage (CIE) coordinates of (0.31, 0.37). An external quantum efficiency of 0.55 percent and a maximum brightness of 1600 cd/m^2 were attained with simple solution-processed single-layer devices. Future goals for this project include a device that features a fluorescent blue singlet emitter in conjunction with phosphorescent red and green emitters all incorporated on a single POSS nanoparticle core. This macromolecule would utilize the fluorescent blue lumophore to harness all of the electrically-generated high-energy singlet excitons (~25%) and the red and green phosphorescent dopants to harvest the remainder of the lower-energy triplet excitons (~75%).

WOLEDs implementing multifunctional macromolecules represent a unique route to producing low-cost and highly-efficient white-light illumination. The development of new functionalized cores will enable WOLEDs to attain higher quantum efficiencies, simplified device architecture, superior white color purity, and longer device lifetimes. This kind of single-emissive molecule combines the advantages of both small molecular and polymeric materials. It is envisioned that such a single-molecule emitter will drastically simplify WOLED device fabrication. This work shows further strides in the improvement of macromolecule-incorporated WOLEDs aiding their advancement to future application.

LIST OF ACRONYMS

AFM	Atomic Force Microscopy
BLT	$Bi_{(4-x)}La_xTi_3O_{12}$
CAFM	Conductance Atomic Force Microscopy
CCT	Color-Correlated Temperature
CD	Compact Disc
CIE	Commission Internationale de l'Eclairage
CPU	Central Processing Unit
CRI	Color Rendering Index
CRT	Cathode Ray Tube
DARPA	Defense Advanced Research Projects Agency
DRAM	Dynamic Random Access Memory
DVD	Digital Versatile Disc
EEPROM	Electrically Erasable Programmable Read Only Memory
ETL	Electron-Transport Layer
FCC	Federal Communications Commission
FeRAM	Ferroelectric Random Access Memory
GPIB	General Purpose Interface Bus
HDD	Hard Disk Drive
HOMO	Highest-Occupied Molecular Orbital
HTL	Hole-Transport Layer
IC-AFM	Intermittent-Contact Mode Atomic Force Microscopy
I-V	Current-Voltage
ITO	Indium Tin Oxide
LCD	Liquid Crystal Display
LED	Light Emitting Diode
LUMO	Lowest-Unoccupied Molecular Orbital
MEH-PPV	Poly[2-methoxy-5-(2'-ethyl-hexyloxy)-1,4-phenylene vinylene
MIM	Metal Insulator Metal
MRAM	Magnetoresistive Random Access Memory
MTJ	Magnetic Tunnel Junction
NA	Numerical Aperture
NDR	Negative Differential Resistance
NPB	N, N'-diphenyl-N, N'-bis(1-naphthyl phenyl)-1, 1'-biphenyl-4, 4'-diamine
OLED	Organic Light-Emitting Device
PANI/CSA	Polyaniline doped with Camphorsulfonic Acid
PBD	2-(4-biphenylyl)-5-(4-tert-butylphenyl)1,3,4-oxadiazole
PDA	Personal Digital Assistant
PEDOT	Polyethylenedioxythiophene: Polystyrene Sulphonic Acid
PEDT	Polyethylenedioxythiophene
POSS	Polyhedral Oligomeric Silsesquioxane
PROM	Programmable Read-Only Memory
PSS	Polystyrene Sulphonic Acid

PVK	Poly(*N*-vinylcarbazole)
PZT	$PbZr_xTi_{(1-x)}O_3$
Ra	Mean Roughness
RAM	Random Access Memory
TUNA	Tunneling AFM

REFERENCES

[1] J. G. Simmons and Verderber, "New Conduction And Reversible Memory Phenomena In Thin Insulating Films," Proceedings Of The Royal Society Of London Series A-Mathematical And Physical Sciences **301** (1464), 77 (1967).

[2] S. Hudgens and B. Johnson, "Overview of phase-change chalcogenide nonvolatile memory technology," MRS Bull. **29** (11), 829 (2004).

[3] Ovshinsk S, "Reversible Electrical Switching Phenomena In Disordered Structures," Phys. Rev. Lett. **21** (20), 1450 (1968).

[4] Y. Arimoto and H. Ishiwara, "Current status of ferroelectric randomm-access memory," MRS Bull. **29** (11), 823 (2004).

[5] H. Kohlstedt, Y. Mustafa, A. Gerber, A. Petraru, M. Fitsilis, R. Meyer, U. Bottger, and R. Waser, "Current status and challenges of ferroelectric memory devices," Microelectron. Eng. **80**, 296 (2005).

[6] S. Masui, T. Ninomiya, M. Oura, W. Yokozeki, K. Mukaida, and S. Kawashima, "A ferroelectric memory-based secure dynamically programmable gate array," IEEE J. Solid-State Circuit **38** (5), 715 (2003).

[7] A. Sheikholeslami and P. G. Gulak, "A survey of circuit innovations in ferroelectric random-access memories," Proc. IEEE **88** (5), 667 (2000).

[8] G. Grynkewich, J. Akerman, R. Brown, B. Butcher, R. W. Dave, M. DeHerrera, M. Durlam, B. N. Engel, J. Janesky, S. Pietambaram, N. D. Rizzo, J. M. Slaughter, K. Smith, J. J. Sun, and S. Tehrani, "Nonvolatile magnetoresistive random-access memory based on magnetic tunnel junctions," MRS Bull. **29** (11), 818 (2004).

[9] Memory Strategies International July 2006 report, NAND and NOR Nanocrystal Flash Memory, 2006.

[10] S. Lombardo, B. De Salvo, C. Gerardi, and T. Baron, "Silicon nanocrystal memories," Microelectron. Eng. **72** (1-4), 388 (2004).

[11] S. Tiwari, F. Rana, K. Chan, H. Hanafi, W. Chan, and D. Buchanan, in *IEDM Technical Digest* (1995), pp. 521.

[12] J. De Blauwe, "Nanocrystal nonvolatile memory devices," IEEE Trans. Nanotechnol. **1** (1), 72 (2002).

[13] T. Shimizuiwayama, S. Nakao, and K. Saitoh, "Visible Photoluminescence In Si+-Implanted Thermal Oxide-Films On Crystalline Si," Appl. Phys. Lett. **65** (14), 1814 (1994).

[14] Z. T. Liu, C. Lee, V. Narayanan, G. Pei, and E. C. Kan, "Metal nanocrystal memories - Part I: Device design and fabrication," IEEE Trans. Electron Devices **49** (9), 1606 (2002).

[15] Z. T. Liu, C. Lee, V. Narayanan, G. Pei, and E. C. Kan, "Metal nanocrystal memories - Part II: Electrical characteristics," IEEE Trans. Electron Devices **49** (9), 1614 (2002).

[16] H. J. Hovel and J. J. Urgell, "Switching And Memory Characteristics Of Znse-Ge Heterojunctions," J. Appl. Phys. **42** (12), 5076 (1971).

[17] A. Beck, J. G. Bednorz, C. Gerber, C. Rossel, and D. Widmer, "Reproducible switching effect in thin oxide films for memory applications," Appl. Phys. Lett. **77** (1), 139 (2000).

[18] J. F. Gibbons and W. E. Beadle, "Switching Properties Of Thin Nio Films," Solid-State Electron. **7** (11), 785 (1964).

[19] F. Argall and A. K. Jonscher, "Dielectric Properties Of Thin Films Of Aluminium Oxide And Silicon Oxide," Thin Solid Films **2** (3), 185 (1968).

[20] Y. Watanabe, J. G. Bednorz, A. Bietsch, C. Gerber, D. Widmer, A. Beck, and S. J. Wind, "Current-driven insulator-conductor transition and nonvolatile memory in chromium-doped SrTiO3 single crystals," Appl. Phys. Lett. **78** (23), 3738 (2001).

[21] M. A. Afifi, M. M. Abdel-Aziz, H. H. Labib, M. Fadel, and E. G. El-Metwally, "Electrical and switching properties of amorphous films based on the Ge-Se-Tl system," Vacuum **61** (1), 45 (2001).

[22] M. A. Afifi, H. H. Labib, N. A. Hegab, M. Fadel, and A. E. Bekheet, "Memory Switching Characteristics Of In2se3 Amorphous Thin-Films," Indian J. Pure Appl. Phys. **33** (3), 129 (1995).

[23] M. F. Kotkata, M. A. Afifi, H. H. Labib, N. A. Hegab, and M. M. Abdelaziz, "Memory Switching In Amorphous Ge-Se-Tl Chalcogenide Semiconductor-Films," Thin Solid Films **240** (1-2), 143 (1994).

[24] M. A. Afifi, N. A. Hegab, H. H. Labib, and M. Fadel, "Switching Phenomenon In Se75ge25-Xsbx Chalcogenide Glass System," Indian J. Pure Appl. Phys. **30** (5), 211 (1992).

[25] D. Adler, M. S. Shur, M. Silver, and S. R. Ovshinsky, "Threshold Switching In Chalcogenide-Glass Thin-Films," J. Appl. Phys. **51** (6), 3289 (1980).

[26] A. M. Barnett, "Current Filaments In Semiconductors," IBM J. Res. Dev. **13** (5), 522 (1969).

[27] W. D. Buckley and S. H. Holmberg, "Electrical Characteristics And Threshold Switching In Amorphous-Semiconductors," Solid-State Electron. **18** (2), 127 (1975).

[28] C. Rossel, G. I. Meijer, D. Bremaud, and D. Widmer, "Electrical current distribution across a metal-insulator-metal structure during bistable switching," J. Appl. Phys. **90** (6), 2892 (2001).

[29] C. C. Lin, B. C. Tu, C. C. Lin, C. H. Lin, and T. Y. Tseng, "Resistive switching mechanisms of V-doped SrZrO3 memory films," IEEE Electron Device Lett. **27** (9), 725 (2006).

[30] K. Szot, W. Speier, G. Bihlmayer, and R. Waser, "Switching the electrical resistance of individual dislocations in single-crystalline SrTiO3," Nat. Mater. **5** (4), 312 (2006).

[31] R. Oligschlaeger, R. Waser, R. Meyer, S. Karthauser, and R. Dittmann, "Resistive switching and data reliability of epitaxial (Ba,Sr)TiO3 thin films," Appl. Phys. Lett. **88** (4) (2006).

[32] D. Lee, H. Choi, H. Sim, D. Choi, H. Hwang, M. J. Lee, S. A. Seo, and I. K. Yoo, "Resistance switching of the nonstoichiometric zirconium oxide for nonvolatile memory applications," IEEE Electron Device Lett. **26** (10), 719 (2005).

[33] R. Fors, S. I. Khartsev, and A. M. Grishin, "Giant resistance switching in metal-insulator-manganite junctions: Evidence for Mott transition," Phys. Rev. B **71** (4) (2005).

[34] A. D. Pearson and C. E. Miller, "Filamentary Conduction In Semiconducting Glass Diodes," Appl. Phys. Lett. **14** (9), 280 (1969).

[35] Dearnale.G, A. M. Stoneham, and D. V. Morgan, "Electrical Phenomena In Amorphous Oxide Films," Rep. Prog. Phys. **33** (11), 1129 (1970).

[36] Sutherla.Rr, "Theory For Negative Resistance And Memory Effects In Thin Insulating Films And Its Application To Au-Zns-Au Devices," J. Phys. D-Appl. Phys. **4** (3), 468 (1971).

[37] G. Dearnaley, D. V. Morgan, and A. M. Stoneham, in *Journal of Non-Crystalline Solids* (1970), pp. 593.

[38] M. J. Rozenberg, I. H. Inoue, and M. J. Sanchez, "Nonvolatile memory with multilevel switching: A basic model," Phys. Rev. Lett. **92** (17) (2004).

[39] A. Sawa, T. Fujii, M. Kawasaki, and Y. Tokura, "Hysteretic current-voltage characteristics and resistance switching at a rectifying Ti/Pr0.7Ca0.3MnO3 interface," Appl. Phys. Lett. **85** (18), 4073 (2004).

[40] A. Baikalov, Y. Q. Wang, B. Shen, B. Lorenz, S. Tsui, Y. Y. Sun, Y. Y. Xue, and C. W. Chu, "Field-driven hysteretic and reversible resistive switch at the Ag-Pr0.7Ca0.3MnO3 interface," Appl. Phys. Lett. **83** (5), 957 (2003).

[41] S. Tsui, A. Baikalov, J. Cmaidalka, Y. Y. Sun, Y. Q. Wang, Y. Y. Yue, C. W. Chu, L. Chen, and A. J. Jacobson, "Field-induced resistive switching in metal-oxide interfaces," Appl. Phys. Lett. **85** (2), 317 (2004).

[42] A. D. Pearson, "Characteristics Of Semiconducting Glass Switching/Memory Diodes," IBM J. Res. Dev. **13** (5), 510 (1969).

[43] H. J. Stocker, "Bulk And Thin Film Switching And Memory Effects In Semiconducting Chalcogenide Glasses," Appl. Phys. Lett. **15** (2), 55 (1969).

[44] Fritzsch.H, "Physics Of Instabilities In Amorphous Semiconductors," IBM J. Res. Dev. **13** (5), 515 (1969).

[45] M. Sugi, M. Kikuchi, S. Iizima, and K. Tanaka, "Switching Characteristics Of Chalcogenide Glass," Solid State Commun. **7** (24), 1805 (1969).

[46] Kevorkia.J, M. M. Labes, D. C. Larson, and D. C. Wu, "Bistable Switching In Organic Thin Films," Discussions Of The Faraday Society (51), 139 (1971).

[47] M. Lauters, B. McCarthy, D. Sarid, and G. E. Jabbour, "Multilevel conductance switching in polymer films," Appl. Phys. Lett. **89** (1) (2006).

[48] C. H. Tu, Y. S. Lai, and D. L. Kwong, "Memory effect in the current-voltage characteristic of 8-hydroquinoline aluminum salt films," IEEE Electron Device Lett. **27** (5), 354 (2006).

[49] M. Lauters, B. McCarthy, D. Sarid, and G. E. Jabbour, "Nonvolatile multilevel conductance and memory effects in organic thin films," Appl. Phys. Lett. **87** (23) (2005).

[50] J. S. Chen, L. L. Xu, J. Lin, Y. H. Geng, L. X. Wang, and D. G. Ma, "Negative differential resistance and multilevel memory effects in organic devices," Semicond. Sci. Technol. **21** (8), 1121 (2006).

[51] D. Tondelier, K. Lmimouni, D. Vuillaume, C. Fery, and G. Haas, "Metal/organic/metal bistable memory devices," Appl. Phys. Lett. **85** (23), 5763 (2004).

[52] L. P. Ma, J. Liu, and Y. Yang, "Organic electrical bistable devices and rewritable memory cells," Appl. Phys. Lett. **80** (16), 2997 (2002).

[53] Y. Yang, J. Ouyang, L. P. Ma, R. J. H. Tseng, and C. W. Chu, "Electrical switching and bistability in organic/polymeric thin films and memory devices," Adv. Funct. Mater. **16** (8), 1001 (2006).

[54] R. J. Tseng, J. Ouyang, C. W. Chu, J. S. Huang, and Y. Yang, "Nanoparticle-induced negative differential resistance and memory effect in polymer bistable light-emitting device," Appl. Phys. Lett. **88** (12) (2006).

[55] L. D. Bozano, B. W. Kean, M. Beinhoff, K. R. Carter, P. M. Rice, and J. C. Scott, "Organic materials and thin-film structures for cross-point memory cells based on trapping in metallic nanoparticles," Adv. Funct. Mater. **15** (12), 1933 (2005).

[56] W. Tang, H. Z. Shi, G. Xu, B. S. Ong, Z. D. Popovic, J. C. Deng, J. Zhao, and G. H. Rao, "Memory effect and negative differential resistance by electrode-induced two-dimensional single-electron tunneling in molecular and organic electronic devices," Adv. Mater. **17** (19), 2307 (2005).

[57] M. Kano, S. Orito, Y. Tsuruoka, and N. Ueno, "Nonvolatile memory effect of an Al/2-Amino-4,5-dicyanoimidazole/Al structure," Synth. Met. **153** (1-3), 265 (2005).

[58] J. Y. Ouyang, C. W. Chu, R. J. H. Tseng, A. Prakash, and Y. Yang, "Organic memory device fabricated through solution processing," Proc. IEEE **93** (7), 1287 (2005).

[59] J. S. Chen and D. G. Ma, "Single-layer organic memory devices based on N,N '-di(naphthalene-l-yl)-N,N '-diphenyl-benzidine," Appl. Phys. Lett. **87** (2) (2005).

[60] C. W. Chu, J. Ouyang, H. H. Tseng, and Y. Yang, "Organic donor-acceptor system exhibiting electrical bistability for use in memory devices," Adv. Mater. **17** (11), 1440 (2005).

[61] R. J. Tseng, J. X. Huang, J. Ouyang, R. B. Kaner, and Y. Yang, "Polyaniline nanofiber/gold nanoparticle nonvolatile memory," Nano Lett. **5** (6), 1077 (2005).

[62] J. He, L. P. Ma, J. H. Wu, and Y. Yang, "Three-terminal organic memory devices," J. Appl. Phys. **97** (6) (2005).

[63] J. Y. Ouyang, C. W. Chu, C. R. Szmanda, L. P. Ma, and Y. Yang, "Programmable polymer thin film and non-volatile memory device," Nat. Mater. **3** (12), 918 (2004).

[64] Y. Yang, L. P. Ma, and J. H. Wu, "Organic thin-film memory," MRS Bull. **29** (11), 833 (2004).

[65] L. P. Ma, Q. F. Xu, and Y. Yang, "Organic nonvolatile memory by controlling the dynamic copper-ion concentration within organic layer," Appl. Phys. Lett. **84** (24), 4908 (2004).

[66] J. H. Wu, L. P. Ma, and Y. Yang, "Single-band Hubbard model for the transport properties in bistable organic/metal nanoparticle/organic devices," Phys. Rev. B **69** (11) (2004).

[67] H. J. Gao, K. Sohlberg, Z. Q. Xue, H. Y. Chen, S. M. Hou, L. P. Ma, X. W. Fang, S. J. Pang, and S. J. Pennycook, "Reversible, nanometer-scale conductance transitions in an organic complex," Phys. Rev. Lett. **84** (8), 1780 (2000) and Y. Thao, A. Fein, C. A. Peterson, and D. Sarid, Phys. Rev. Lett. **87** 9706 (2001).

[68] H. K. Henisch and W. R. Smith, "Switching In Organic Polymer-Films," Appl. Phys. Lett. **24** (12), 589 (1974).

[69] H. Carchano, R. Lacoste, and Y. Segui, "Bistable Electrical Switching In Polymer Thin Films," Appl. Phys. Lett. **19** (10), 414 (1971).

[70] Y. Segui, B. Ai, and H. Carchano, "Switching In Polystyrene Films - Transition From On To Off State," J. Appl. Phys. **47** (1), 140 (1976).

[71] A. Saneto, M. Octavio, R. C. Callarotti, P. E. Schmidt, and P. Esqueda, "Conduction And Threshold Switching In Small Area Lateral Metal-Polymer-Metal Devices," J. Appl. Phys. **51** (7), 3827 (1980).

[72] R. S. Potember, T. O. Poehler, and D. O. Cowan, "Electrical Switching And Memory Phenomena In Cu-Tcnq Thin-Films," Appl. Phys. Lett. **34** (6), 405 (1979).

[73] Y. G. Kriger, N. F. Yudanov, I. K. Igumenov, and S. B. Vashchenko, "Study Of Test Structures Of A Molecular Memory-Element," J. Struct. Chem. **34** (6), 966 (1993).

[74] J. Chen, J. Su, W. Wang, and M. A. Reed, "Electronic memory effects in self-assembled monolayer systems," Physica E **16** (1), 17 (2003).

[75] J. Chen, W. Wang, J. Klemic, M. A. Reed, B. W. Axelrod, D. M. Kaschak, A. M. Rawlett, D. W. Price, S. M. Dirk, J. M. Tour, D. S. Grubisha, and D. W. Bennett, in *Molecular Electronics Ii* (New York Acad Sciences, New York, 2002), Vol. 960, pp. 69.

[76] J. Chen, W. Wang, M. A. Reed, A. M. Rawlett, D. W. Price, and J. M. Tour, "Room-temperature negative differential resistance in nanoscale molecular junctions," Appl. Phys. Lett. **77** (8), 1224 (2000).

[77] J. Chen, M. A. Reed, A. M. Rawlett, and J. M. Tour, "Large on-off ratios and negative differential resistance in a molecular electronic device," Science **286** (5444), 1550 (1999).

[78] E. P. Harris, "Superconductivity In Ain Bistable Resistance Devices," Appl. Phys. Lett. **24** (10), 514 (1974).

[79] A. C. Arias, I. A. Hummelgen, A. Meneguzzi, and C. Ferreira, "A conjugated polymer-based voltage-regulator device," Adv. Mater. **9** (12), 972 (1997).

[80] Szymansk.A, D. C. Larson, and M. M. Labes, "A Temperature-Independent Conducting State In Tetracene Thin Film," Appl. Phys. Lett. **14** (3), 88 (1969).

[81] A. R. Elsharkawi and K. C. Kao, "Switching And Memory Phenomena In Anthracene Thin-Films," J. Phys. Chem. Solids **38** (1), 95 (1977).

[82] S. G. Liu, Y. Q. Liu, and D. B. Zhu, "Electrical switching and memory phenomena in Al/[TBA](y)[Ni(DMID)(2)]/Cu system," Mol. Cryst. Liq. Cryst. Sci. Technol. Sect. A-Mol. Cryst. Liq. Cryst. **281**, 229 (1996).

[83] A. R. Duggal and L. M. Levinson, "High power switching behavior in electrically conductive polymer composite materials," Appl. Phys. Lett. **71** (14), 1939 (1997).

[84] H. K. Henisch, J. A. Meyers, R. C. Callarotti, and P. E. Schmidt, "Switching In Organic Polymer-Films," Thin Solid Films **51** (3), 265 (1978).

[85] K. Takimoto, H. Kawade, E. Kishi, K. Yano, K. Sakai, K. Hatanaka, K. Eguchi, and T. Nakagiri, "Switching And Memory Phenomena In Langmuir-Blodgett-Films With Scanning Tunneling Microscope," Appl. Phys. Lett. **61** (25), 3032 (1992).

[86] E. G. Gerstner and D. R. McKenzie, "Nonvolatile memory effects in nitrogen doped tetrahedral amorphous carbon thin films," J. Appl. Phys. **84** (10), 5647 (1998).

[87] L. P. Ma, J. Liu, S. M. Pyo, and Y. Yang, "Organic bistable light-emitting devices," Appl. Phys. Lett. **80** (3), 362 (2002).

[88] R. G. Sharpe and R. E. Palmer, ""Concerted" regeneration of electroformed metal-insulator-metal devices," J. Appl. Phys. **79** (11), 8565 (1996).

[89] R. G. Sharpe and R. E. Palmer, "Regeneration of electroformed metal-insulator-metal devices: A new model," J. Phys.-Condes. Matter **8** (3), 329 (1996).

[90] C. Y. Liu, C. C. Chuang, J. S. Chen, A. Wang, W. Y. Jang, J. C. Young, K. Y. Chiu, and T. Y. Tseng, "Memory effect of sol-gel derived V-doped SrZrO3 thin films," Thin Solid Films **494** (1-2), 287 (2006).

[91] S. Moller, C. Perlov, W. Jackson, C. Taussig, and S. R. Forrest, "A polymer/semiconductor write-once read-many-times memory," Nature **426** (6963), 166 (2003).

[92] Q. D. Ling, Y. Song, S. J. Ding, C. X. Zhu, D. S. H. Chan, D. L. Kwong, E. T. Kang, and K. G. Neoh, "Non-volatile polymer memory device based on a novel copolymer of N-vinylcarbazole and Eu-complexed vinylbenzoate," Adv. Mater. **17** (4), 455 (2005).

[93] D. Ma, M. Aguiar, J. A. Freire, and I. A. Hummelgen, "Organic reversible switching devices for memory applications," Adv. Mater. **12** (14), 1063 (2000).

[94] F. R. F. Fan, J. P. Yang, L. T. Cai, D. W. Price, S. M. Dirk, D. V. Kosynkin, Y. X. Yao, A. M. Rawlett, J. M. Tour, and A. J. Bard, "Charge transport through self-assembled monolayers of compounds of interest in molecular electronics," J. Am. Chem. Soc. **124** (19), 5550 (2002).

[95] B. Mukherjee and A. J. Pal, "On the origin of multilevel conductance and memory in ultrathin organic films," Synth. Met. **155** (2), 336 (2005).

[96] Z. J. Donhauser, B. A. Mantooth, K. F. Kelly, L. A. Bumm, J. D. Monnell, J. J. Stapleton, D. W. Price, A. M. Rawlett, D. L. Allara, J. M. Tour, and P. S. Weiss, "Conductance switching in single molecules through conformational changes," Science **292** (5525), 2303 (2001).

[97] C. D. Muller, A. Falcou, N. Reckefuss, M. Rojahn, V. Wiederhirn, P. Rudati, H. Frohne, O. Nuyken, H. Becker, and K. Meerholz, "Multi-colour organic light-emitting displays by solution processing," Nature **421** (6925), 829 (2003).

[98] P. Fairley, "Solar-cell rollout," Technol. Rev. **107** (6), 34 (2004).

[99] J. Y. Ouyang, C. W. Chu, D. Sieves, and Y. Yang, "Electric-field-induced charge transfer between gold nanoparticle and capping 2-naphthalenethiol and organic memory cells," Appl. Phys. Lett. **86** (12) (2005).

[100] C. Laurent, E. Kay, and N. Souag, "Dielectric-Breakdown Of Polymer-Films Containing Metal-Clusters," J. Appl. Phys. **64** (1), 336 (1988).

[101] L. D. Bozano, B. W. Kean, V. R. Deline, J. R. Salem, and J. C. Scott, "Mechanism for bistability in organic memory elements," Appl. Phys. Lett. **84** (4), 607 (2004).

[102] L. P. Ma, J. Liu, S. Pyo, Q. F. Xu, and Y. Yang, "Organic bistable devices," Mol. Cryst. Liquid Cryst. **378**, 185 (2002).

[103] L. P. Ma, S. Pyo, J. Ouyang, Q. F. Xu, and Y. Yang, "Nonvolatile electrical bistability of organic/metal-nanocluster/organic system," Appl. Phys. Lett. **82** (9), 1419 (2003).

[104] R. Pati and S. P. Karna, "Current switching by conformational change in a pi-sigma-pi molecular wire," Phys. Rev. B **69** (15) (2004).

[105] T. Tsujioka and H. Kondo, "Organic bistable molecular memory using photochromic diarylethene," Appl. Phys. Lett. **83** (5), 937 (2003).

[106] J. P. A. Williamson and R. A. Collins, "Electroforming And Switching In Mim Structures Under Pulsed Bias," Int. J. Electron. **38** (3), 413 (1975).

[107] K. B. Kim, Y. H. Tak, Y. S. Han, K. H. Baik, M. H. Yoon, and M. H. Lee, "Relationship between surface roughness of indium tin oxide and leakage current of organic light-emitting diode," Jpn. J. Appl. Phys. Part 2 - Lett. **42** (4B), L438 (2003).

[108] Y. H. Tak, K. B. Kim, H. G. Park, K. H. Lee, and J. R. Lee, "Criteria for ITO (indium-tin-oxide) an organic light thin film as the bottom electrode of emitting diode," Thin Solid Films **411** (1), 12 (2002).

[109] R. E. Thurstans and P. J. Harris, in *Electron Microscopy And Analysis 1997* (Iop Publishing Ltd, Bristol, 1997), pp. 621.

[110] H. Aziz and Z. D. Popovic, "Degradation phenomena in small-molecule organic light-emitting devices," Chem. Mat. **16** (23), 4522 (2004).

[111] Z. D. Popovic and H. Aziz, "Reliability and degradation of small molecule-based organic light-emitting devices (OLEDs)," IEEE J. Sel. Top. Quantum Electron. **8** (2), 362 (2002).

[112] S. J. Chua, L. Ke, R. S. Kumar, and K. Zhang, "Stabilization of electrode migration in polymer electroluminescent devices," Appl. Phys. Lett. **81** (6), 1119 (2002).

[113] L. Ke, S. J. Chua, K. Zhang, and N. Yakovlev, "Degradation and failure of organic light-emitting devices," Appl. Phys. Lett. **80** (12), 2195 (2002).

[114] H. R. Zeller and I. Giaever, "Tunneling, Zero-Bias Anomalies, And Small Superconductors," Physical Review **181** (2), 789 (1969).

[115] J. P. Hiernaut, R. P. Forier, and Vancaken.J, "Influence Of Oxygen On Electron-Trapping By Surfaces Of Metal-Oxides," Vacuum **22** (10), 471 (1972).

[116] Holzapfe.G, "Thermionic Emission From Electron Traps," Vacuum **22** (10), 467 (1972).

[117] R. E. Thurstans and D. P. Oxley, "The electroformed metal-insulator-metal structure: a comprehensive model," J. Phys. D-Appl. Phys. **35** (8), 802 (2002).

[118] C. W. Tang and S. A. Vanslyke, "Organic Electroluminescent Diodes," Appl. Phys. Lett. **51** (12), 913 (1987).

[119] Vol.1 U. S. Department of Energy National Lighting Inventory and Energy Consumption Estimate, U.S. Government Printing Office, Washington, DC, p.x., (2002).

[120] National Lighting Inventory and Energy Consumption Estimate U. S. Department of Energy, Vol.1, U.S. Government Printing Office, Washington, DC, p.xii.], 2002.

[121] M. Pope, P. Magnante, and H. P. Kallmann, "Electroluminescence In Organic Crystals," J. Chem. Phys. **38** (8), 2042 (1963).

[122] W. Helfrich and Schneide.Wg, "Recombination Radiation In Anthracene Crystals," Phys. Rev. Lett. **14** (7), 229 (1965).

[123] C.H. Chen C.W. Tang, and R. Goswami, US Patent 4,769,292, (1988).

[124] L. S. Hung and C. H. Chen, "Recent progress of molecular organic electroluminescent materials and devices," Mater. Sci. Eng. R-Rep. **39** (5-6), 143 (2002).

[125] M. A. Baldo, "The electronic and optical properties of amorphous organic semiconductors," (2001).

[126] B. W. D'Andrade and J. J. Brown, "Organic light-emitting device luminaire for illumination applications," Appl. Phys. Lett. **88** (19) (2006).

[127] G. Gu, D. Z. Garbuzov, P. E. Burrows, S. Venkatesh, S. R. Forrest, and M. E. Thompson, "High-external-quantum-efficiency organic light-emitting devices," Opt. Lett. **22** (6), 396 (1997).

[128] C. F. Madigan, M. H. Lu, and J. C. Sturm, "Improvement of output coupling efficiency of organic light-emitting diodes by backside substrate modification," Appl. Phys. Lett. **76** (13), 1650 (2000).

[129] J. S. Kim, P. K. H. Ho, N. C. Greenham, and R. H. Friend, "Electroluminescence emission pattern of organic light-emitting diodes: Implications for device efficiency calculations," J. Appl. Phys. **88** (2), 1073 (2000).

[130] A. D. Broadbent, "A critical review of the development of the CIE1931 RGB color-matching functions," Color Res. Appl. **29** (4), 267 (2004).

[131] H. S. Fairman, M. H. Brill, and H. Hemmendinger, "How the CIE 1931 color-matching functions were derived from Wright-Guild data," Color Res. Appl. **22** (1), 11 (1997).

[132] M. Shaw and M. Fairchild, "Evaluating the 1931 CIE colour-matching functions," Color Res. Appl. **27** (5), 316 (2002).

[133] J. Kido, K. Hongawa, K. Okuyama, and K. Nagai, "White Light-Emitting Organic Electroluminescent Devices Using The Poly(N-Vinylcarbazole) Emitter Layer Doped With 3 Fluorescent Dyes," Appl. Phys. Lett. **64** (7), 815 (1994).

[134] S. R. Forrest, P. E. Burrows, Z. Shen, G. Gu, V. Bulovic, and M. E. Thompson, "The stacked OLED (SOLED): a new type of organic device for achieving high-resolution full-color displays," Synth. Met. **91** (1-3), 9 (1997).

[135] J. Kido, M. Kimura, and K. Nagai, "Multilayer White Light-Emitting Organic Electroluminescent Device," Science **267** (5202), 1332 (1995).

[136] B. W. D'Andrade, M. E. Thompson, and S. R. Forrest, "Controlling exciton diffusion in multilayer white phosphorescent organic light emitting devices," Adv. Mater. **14** (2), 147 (2002).

[137] B. W. D'Andrade, J. Brooks, V. Adamovich, M. E. Thompson, and S. R. Forrest, "White light emission using triplet excimers in electrophosphorescent organic light-emitting devices," Adv. Mater. **14** (15), 1032 (2002).

[138] R. H. Jordan, A. Dodabalapur, M. Strukelj, and T. M. Miller, "White organic electroluminescence devices," Appl. Phys. Lett. **68** (9), 1192 (1996).

[139] Z. G. Liu and H. Nazare, "White organic light-emitting diodes emitting from both hole and electron transport layers," Synth. Met. **111**, 47 (2000).

[140] T. R. Hebner, C. C. Wu, D. Marcy, M. H. Lu, and J. C. Sturm, "Ink-jet printing of doped polymers for organic light emitting devices," Appl. Phys. Lett. **72** (5), 519 (1998).

[141] G. E. Jabbour, R. Radspinner, and N. Peyghambarian, "Screen printing for the fabrication of organic light-emitting devices," IEEE J. Sel. Top. Quantum Electron. **7** (5), 769 (2001).

[142] B. W. D'Andrade and S. R. Forrest, "White organic light-emitting devices for solid-state lighting," Adv. Mater. **16** (18), 1585 (2004).

[143] M. Granstrom and O. Inganas, "White light emission from a polymer blend light emitting diode," Appl. Phys. Lett. **68** (2), 147 (1996).

[144] D. H. Hwang, M. J. Park, and C. Lee, "White LEDs using conjugated polymer blends," Synth. Met. **152** (1-3), 205 (2005).

[145] J. Kido, H. Shionoya, and K. Nagai, "Single-Layer White Light-Emitting Organic Electroluminescent Devices Based On Dye-Dispersed Poly(N-Vinylcarbazole)," Appl. Phys. Lett. **67** (16), 2281 (1995).

[146] X. Gong, W. L. Ma, J. C. Ostrowski, G. C. Bazan, D. Moses, and A. J. Heeger, "White electrophosphorescence from semiconducting polymer blends," Adv. Mater. **16** (7), 615 (2004).

[147] J. S. Kim, B. W. Seo, and H. B. Gu, "Exciplex emission and energy transfer in white light-emitting organic electroluminescent device," Synth. Met. **132** (3), 285 (2003).

[148] V. Adamovich, J. Brooks, A. Tamayo, A. M. Alexander, P. I. Djurovich, B. W. D'Andrade, C. Adachi, S. R. Forrest, and M. E. Thompson, "High efficiency single dopant white electrophosphorescent light emitting diodes," New J. Chem. **26** (9), 1171 (2002).

[149] D. A. Pardo, G. E. Jabbour, and N. Peyghambarian, "Application of screen printing in the fabrication of organic light-emitting devices," Adv. Mater. **12** (17), 1249 (2000).

[150] B. J. de Gans, P. C. Duineveld, and U. S. Schubert, "Inkjet printing of polymers: State of the art and future developments," Adv. Mater. **16** (3), 203 (2004).

[151] L. Deng, P. T. Furuta, S. Garon, J. Li, D. Kavulak, M. E. Thompson, and J. M. J. Frechet, "Living radical polymerization of bipolar transport materials for highly efficient light emitting diodes," Chem. Mat. **18** (2), 386 (2006).

[152] P. T. Furuta, L. Deng, S. Garon, M. E. Thompson, and J. M. J. Frechet, "Platinum-functionalized random copolymers for use in solution-processible, efficient, near-white organic light-emitting diodes," J. Am. Chem. Soc. **126** (47), 15388 (2004).

[153] S. F. Li, G. Zhong, W. H. Zhu, F. Y. Li, J. F. Pan, W. Huang, and H. Tian, "Dendritic europium complex as a single dopant for white-light electroluminescent devices," J. Mater. Chem. **15** (31), 3221 (2005).

[154] S. F. Li, G. Y. Zhong, W. H. Zhu, F. Y. Li, J. F. Pan, W. Huang, and H. Tian, "White light electroluminescence from a dendritic europimn complex," Chem. Lett. **34** (5), 688 (2005).

[155] R. H. Baney, M. Itoh, A. Sakakibara, and T. Suzuki, "Silsesquioxanes," Chem. Rev. **95** (5), 1409 (1995).

[156] A. Sellinger, R. Tamaki, R. M. Laine, K. Ueno, H. Tanabe, E. Williams, and G. E. Jabbour, "Heck coupling of haloaromatics with octavinylsilsesquioxane: solution processable nanocomposites for application in electroluminescent devices," Chem. Commun. (29), 3700 (2005).

[157] Y. Xiao, L. Liu, C. B. He, W. S. Chin, T. T. Lin, K. Y. Mya, J. C. Huang, and X. H. Lu, "Nano-hybrid luminescent dot: synthesis, characterization and optical properties," J. Mater. Chem. **16** (9), 829 (2006).

[158] I. Imae and Y. Kawakami, "Unique photoluminescence property of a novel perfectly carbazole-substituted POSS," J. Mater. Chem. **15** (43), 4581 (2005).

[159] J. K. Cammack, G. E. Jabbour, S. Li, and J. Froehlich, Patent No. WO2005037955 A1.

[160] X. Q. Lin, B. J. Chen, X. H. Zhang, C. S. Lee, H. L. Kwong, and S. T. Lee, "A novel yellow fluorescent dopant for high-performance organic electroluminescent devices," Chem. Mat. **13** (2), 456 (2001).

[161] F. J. Feher and T. A. Budzichowski, Polyhedron **22** (14), 3239 (1995).

[162] J. D. Froehlich, R. Young, T. Nakamura, Y. Oomori, S. Li, A. Mochizuki, M. Lauters, and G. E. Jabbour, (2006).

[163] W. D. Gill, "Drift Mobilities In Amorphous Charge-Transfer Complexes Of Trinitrofluorenone And Poly-N-Vinylcarbazole," J. Appl. Phys. **43** (12), 5033 (1972).

[164] R. Gupta, M. Stevenson, M. D. McGehee, A. Dogariu, V. Srdanov, J. Y. Park, and A. J. Heeger, "Forster transfer based amplified spontaneous emission in conjugated polymer blends," Synth. Met. **102** (1-3), 875 (1999).

[165] M. A. Baldo, D. F. O'Brien, Y. You, A. Shoustikov, S. Sibley, M. E. Thompson, and S. R. Forrest, "Highly efficient phosphorescent emission from organic electroluminescent devices," Nature **395** (6698), 151 (1998).

[166] B. W. D'Andrade and S. R. Forrest, "Effects of exciton and charge confinement on the performance of white organic p-i-n electrophosphorescent emissive excimer devices," J. Appl. Phys. **94** (5), 3101 (2003).

[167] B. W. D'Andrade, R. J. Holmes, and S. R. Forrest, "Efficient organic electrophosphorescent white-light-emitting device with a triple doped emissive layer," Adv. Mater. **16** (7), 624 (2004).

[168] S. Tokito, T. Iijima, T. Tsuzuki, and F. Sato, "High-efficiency white phosphorescent organic light-emitting devices with greenish-blue and red-emitting layers," Appl. Phys. Lett. **83** (12), 2459 (2003).